

## Robotically assisted eye surgery : a haptic master console

**Citation for published version (APA):**

Hendrix, R. (2011). *Robotically assisted eye surgery : a haptic master console*. [Phd Thesis 1 (Research TU/e / Graduation TU/e), Mechanical Engineering]. Technische Universiteit Eindhoven.  
<https://doi.org/10.6100/IR696904>

**DOI:**

[10.6100/IR696904](https://doi.org/10.6100/IR696904)

**Document status and date:**

Published: 01/01/2011

**Document Version:**

Publisher's PDF, also known as Version of Record (includes final page, issue and volume numbers)

**Please check the document version of this publication:**

- A submitted manuscript is the version of the article upon submission and before peer-review. There can be important differences between the submitted version and the official published version of record. People interested in the research are advised to contact the author for the final version of the publication, or visit the DOI to the publisher's website.
- The final author version and the galley proof are versions of the publication after peer review.
- The final published version features the final layout of the paper including the volume, issue and page numbers.

[Link to publication](#)

**General rights**

Copyright and moral rights for the publications made accessible in the public portal are retained by the authors and/or other copyright owners and it is a condition of accessing publications that users recognise and abide by the legal requirements associated with these rights.

- Users may download and print one copy of any publication from the public portal for the purpose of private study or research.
- You may not further distribute the material or use it for any profit-making activity or commercial gain
- You may freely distribute the URL identifying the publication in the public portal.

If the publication is distributed under the terms of Article 25fa of the Dutch Copyright Act, indicated by the "Taverne" license above, please follow below link for the End User Agreement:

[www.tue.nl/taverne](http://www.tue.nl/taverne)

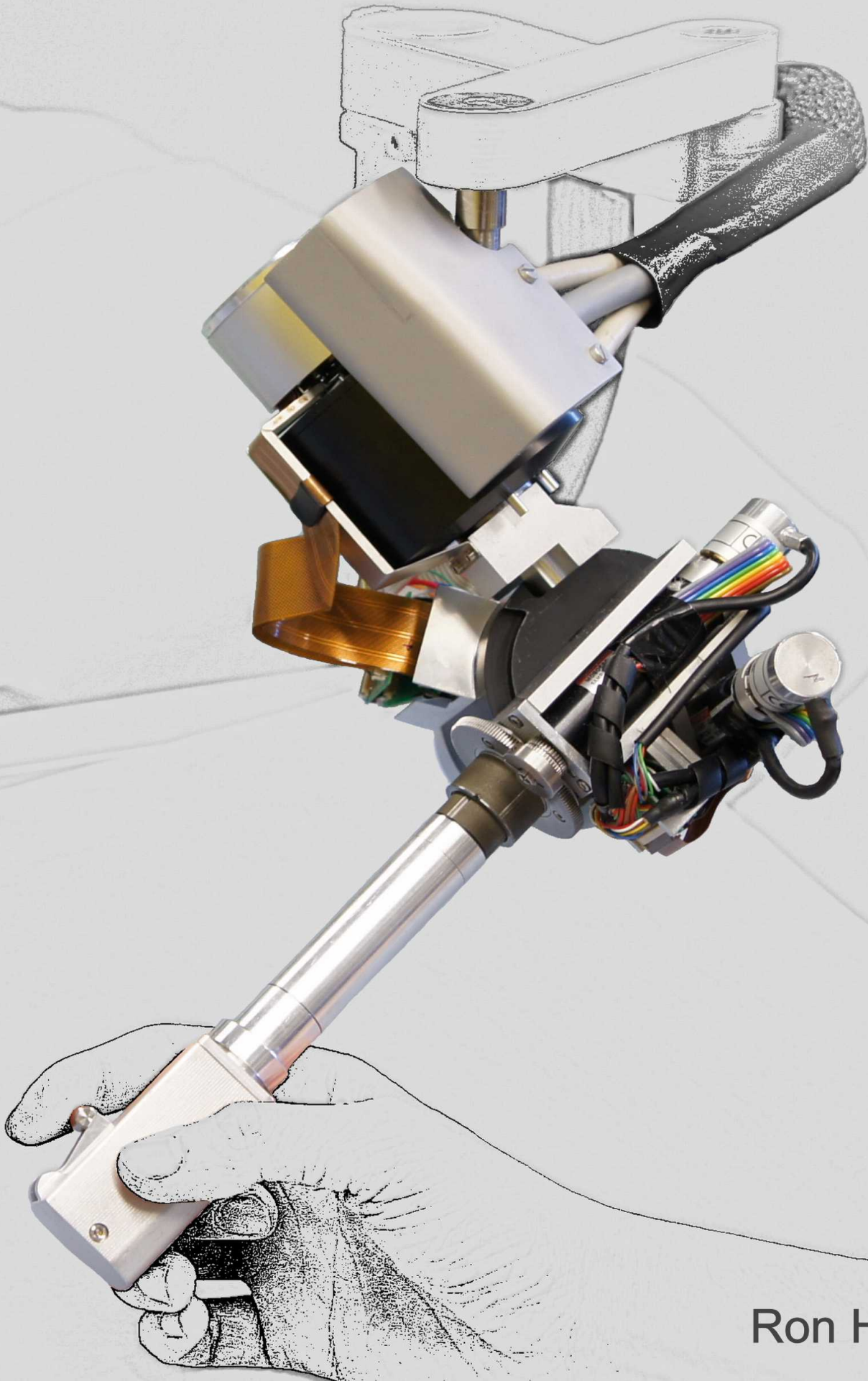
**Take down policy**

If you believe that this document breaches copyright please contact us at:

[openaccess@tue.nl](mailto:openaccess@tue.nl)

providing details and we will investigate your claim.

# Robotically assisted eye surgery: A haptic master console



Ron Hendrix



This research was financially supported by the IOP Precision Technology program of the Dutch Ministry of Economic Affairs.

Robotically assisted eye surgery: A haptic master console  
by Ron Hendrix  
Eindhoven: Technische Universiteit Eindhoven, 2011 - Proefschrift

A catalogue record is available from the Eindhoven University of Technology Library.  
ISBN: 978-90-386-2442-6  
NUR: 978

Cover design: Thijs Meenink and Ron Hendrix  
Reproduction: Ipskamp Drukkers B.V., Enschede, The Netherlands

Copyright ©2011 by R. Hendrix. All rights reserved.

# Robotically assisted eye surgery: A haptic master console

PROEFSCHRIFT

ter verkrijging van de graad van doctor  
aan de Technische Universiteit Eindhoven,  
op gezag van de rector magnificus, prof.dr.ir. C.J. van Duijn,  
voor een commissie aangewezen door het College voor Promoties  
in het openbaar te verdedigen  
op dinsdag 29 maart 2011 om 16.00 uur

door

Ronny Hendrix

geboren te Arcen en Velden

Dit proefschrift is goedgekeurd door de promotoren:

prof.dr. H. Nijmeijer

en

prof.dr.ir. M. Steinbuch

Copromotor:

dr.ir. P.C.J.N. Rosielle

# Contents

---

<b>1</b>	<b>Introduction</b>	<b>1</b>
1.1	Robotics . . . . .	1
1.2	Minimally invasive surgery . . . . .	2
1.3	Manually performed vitreo-retinal eye surgery . . . . .	5
1.4	Goal of this thesis . . . . .	8
1.5	Master console . . . . .	9
1.6	Outline of the thesis . . . . .	10
<b>2</b>	<b>Design requirements of the master console</b>	<b>11</b>
2.1	Vitreo-retinal eye surgery . . . . .	11
2.1.1	Vitreotomy . . . . .	13
2.1.2	Membrane peeling . . . . .	16
2.1.3	Repair of a retinal detachment . . . . .	18
2.1.4	Requirements with respect to the instrument movements . . . . .	19
2.1.5	Visualization with microscope and endoscope . . . . .	20
2.2	Robotically assisted eye surgery . . . . .	20
2.2.1	Hand held tools . . . . .	21
2.2.2	Master-slave systems already realized . . . . .	22
2.2.3	Eye surgery with the da Vinci . . . . .	24
2.2.4	Studies on master-slave systems . . . . .	25
2.2.5	Conclusions . . . . .	26
2.3	Haptic devices as part of the master console . . . . .	28
2.3.1	Generic haptic desktop devices . . . . .	28
2.3.2	Haptic devices for minimally invasive surgery . . . . .	34
2.3.3	Conclusions . . . . .	34
<b>3</b>	<b>Master console</b>	<b>37</b>
3.1	Surgical setup . . . . .	37
3.2	Main components of the master console . . . . .	40
3.2.1	3D Visualization . . . . .	40

3.2.2	Stylus based haptic interface . . . . .	44
3.2.3	Coarse adjustment . . . . .	45
3.2.4	Frame and ergonomics . . . . .	47
3.3	Concept layouts for the console . . . . .	48
3.4	Conclusions . . . . .	51
<b>4</b>	<b>Single DoF master-slave setups</b>	<b>53</b>
4.1	Existing single DoF master-slave setups . . . . .	54
4.2	Design specifications and requirements . . . . .	55
4.3	Single DoF rotational setup . . . . .	58
4.3.1	Mechanical design . . . . .	58
4.3.2	Electronics and safety . . . . .	68
4.3.3	Dynamic model and experimental results . . . . .	68
4.3.4	Position error controller . . . . .	71
4.4	Single DoF linear setup . . . . .	73
4.5	Conclusions . . . . .	77
<b>5</b>	<b>Haptic interface</b>	<b>81</b>
5.1	Design considerations . . . . .	81
5.2	Design and working principle . . . . .	82
5.2.1	$\varphi$ and $\psi$ housing . . . . .	84
5.2.2	$z$ - $\theta$ module . . . . .	87
5.2.3	Button part . . . . .	89
5.2.4	Wiring and electronics . . . . .	91
5.3	Results . . . . .	94
5.4	Conclusions . . . . .	96
<b>6</b>	<b>Improvements for the haptic interface</b>	<b>99</b>
6.1	Actuation concepts . . . . .	99
6.1.1	$\varphi$ and $\psi$ module . . . . .	99
6.1.2	$z$ and $\theta$ module . . . . .	108
6.2	Concept layout . . . . .	113
6.3	Conclusions . . . . .	114
<b>7</b>	<b>Conclusions and recommendations</b>	<b>117</b>
7.1	Conclusions . . . . .	117
7.2	Recommendations . . . . .	119
<b>A</b>	<b>Principal planes in human anatomy</b>	<b>121</b>
<b>B</b>	<b>Identification of the haptic interface</b>	<b>123</b>

---

C Kinematics of the bridge structure	125
Bibliography	127
Nomenclature	133
Summary	137
Samenvatting	139
Dankwoord	143
Curriculum Vitae	145





## CHAPTER ONE

# Introduction

---

**Abstract /** A robotic master-slave device can assist a surgeon during surgery on the vitreous humor and retina, as it combines the advantages of robotic systems with the surgeon's expertise. The slave is the robotic device that manipulates the instruments. The surgeon controls the slave robot via the master. This master device scales the surgeon's hand motions and provides force feedback to extend existing surgical skills during vitreo-retinal eye surgery.

Robotically assisted surgery enhances the surgeon's dexterity and is therefore beneficial for both the surgeon and the patient. This chapter is about the background of robotics and the application of robotic systems for minimally invasive surgery and vitreo-retinal eye surgery. The goal of this thesis is also discussed. Section 1.6 gives the outline of this thesis.

## 1.1 Robotics

Robots are in widespread use as they have different advantages over humans, like:

- potentially faster
- potentially cheaper
- more precise
- usable in a hazardous environment
- able to work with heavy and large components

A typical example is the use of industrial robots for car manufacturing. Here, the robots are used for tasks like the handling of the body panels, spot welding and painting.

Industrial robots are designed as multi DoF, multi purpose devices. A specific end effector tool and program make them suitable for a dedicated task. A second example is a pick and place robot for the assembly of printed circuit boards (PCBs). In this case, the robot transfers components from a reel to a specific location on the PCB.

An industrial robot and a pick and place robot have in common that they perform repetitive tasks in a static environment. Sensor information and a vision system can be used to deal with variations in the production process, for example the tolerance as found on the location of a PCB in the pick and place machine.

It is not possible for these systems to work in a dynamic environment, as it requires that the robot works autonomously. An example of research on autonomous robotic system is described in [76]. The paper is about the perception of doors and handles and what is needed to open or close them. This is one of the requirements for a personal robot to enter and function in a human living environment. The use of autonomous robotic systems does not automatically mean that humans have become superfluous. This is as an autonomous robot is not able (yet) to make complex decisions, like humans can do.

A third category of robotic systems are the master-slave or teleoperation systems where the advantages of robotic systems are used in combination with human's expertise. The slave is the robotic device that interacts with an object: the environment. A human operator controls the slave robot via the master device. Master and slave are mechanically connected or connected via electronic hardware and control software. When the master is provided with force feedback, then the operator can feel the interaction forces between slave and environment. Scaling of forces and movements can be implemented in the mechanical or electrical connection between master and slave.

The use of master-slave systems goes back to the 1940s and 1950s where R.C. Goertz worked on mechanical and electronically controlled manipulators for the remote handling of radioactive material for nuclear research [65].

Since the end of the 1990s, master-slave systems are also used for minimally invasive surgery (MIS), like surgery in the abdomen (laparoscopy) and in the chest (thoracoscopy).

## 1.2 Minimally invasive surgery

Laparoscopy and thoracoscopy are just two examples of minimally invasive surgery. In general, MIS is performed with  $\approx 300$  mm long instruments through three or four surgeon made entry points (figure 1.1). These points have a diameter of 10 mm and are often fitted with a trocar. The advantages for the patient are a reduced hospital stay and less complications. Compared to open surgery, the surgeon has to deal with

inverted instrument movements (due to the pivoting point) and a limited number of degrees of freedom (DoFs), which makes suturing for example more difficult. A surgeon has to work often in a non ergonomic body posture.

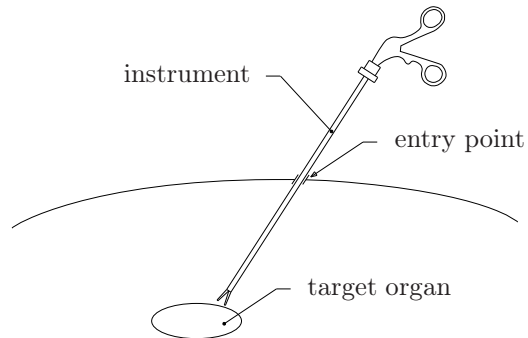


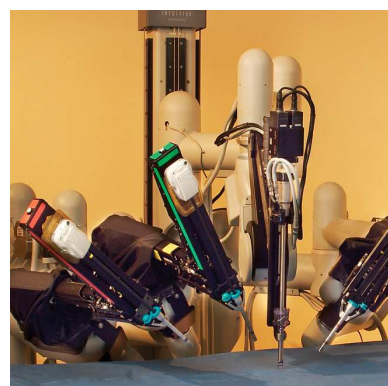
**Figure 1.1** / Minimally invasive surgery. An instrument is  $\approx 300$  mm long and has a diameter of 10 mm.

### Robotically assisted minimally invasive surgery

The commercially available da Vinci<sup>®</sup> surgical system (figure 1.2) from Intuitive Surgical, Inc. [40] deals with the inverted instrument movements and limited number of DoFs. It enhances the surgeon's dexterity by introducing additional DoFs and instrument scaling. The system consists of a surgeon console (master) and a patient-side cart (slave).



(a) surgeon console (master)



(b) patient-side cart (slave) [40]

**Figure 1.2** / Da Vinci<sup>®</sup> surgical system, Intuitive Surgical, Inc.

The slave is placed near the operating table. The slave has three arms with an option for a fourth. The arms are mounted to a central pillar. Draping of the slave guarantees

sterility during surgery. One of the arms manipulates the endoscope in four DoFs, the other arms are used to manipulate the different instruments in 6 or 7 DoFs. The DoFs of the endoscope and the first four of the instrument are the movements about the entry or trocar point. Two of the remaining DoFs are used to manipulate the tip of the instrument like a wrist joint to enhance dexterity. The optional seventh DoF is the operation of the clamp or forceps.

The surgeon console is provided with a visualization system and two master controls. The visualization system gives a 3D image of the surgical field. The controls are used to translate the surgeon's hand movements into real-time movements of two surgical instruments. Switching between the instrument arms enables the control of all instruments and endoscope with only two master controls.

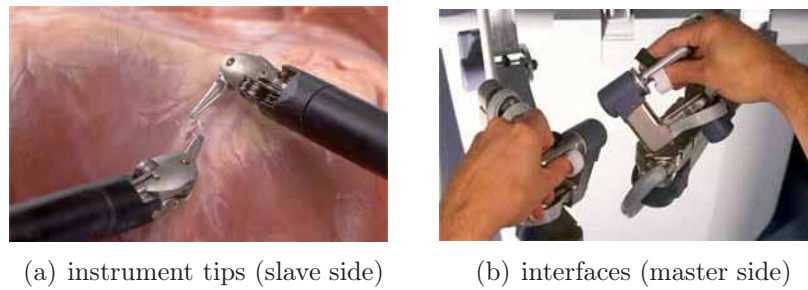


**Figure 1.3** / An intuitive way of working is achieved by the similarity between hand and instrument tip movements [40].

The similarity between the hand and instrument tip movements (figure 1.3) in combination with the natural hand-eye instrument alignment gives an intuitive way of working.

In spite of the advantages of the da Vinci<sup>®</sup> system, surgeons indicate that it is also desirable to have: a table mounted slave to ease table adjustment during surgery, instruments with additional DoFs to extend organ approach capabilities, force feedback to reduce operating time and to improve safety for the patient and, in the last place, a more compact slave design to facilitate access to the patient and the field of surgery. These features are integrated in the slave as designed and realized at the TU/e [7], see figure 1.4.

Issues such as a non ergonomic body posture, inverted instrument movements and absence of force feedback are also seen during eye surgery. Furthermore, downscaling of the hand movements enables the surgeon to work with a higher accuracy [16] and makes it possible to perform tasks like microcannulation which are difficult or impossible to do manually [88]. Therefore, a master-slave system would also be useful for vitreo-retinal eye surgery.



**Figure 1.4** / Slave as designed and realized at the TU/e. The slave is table mounted and can be equipped with up to three instrument manipulators. (Photo: Bart van Overbeeke)

### 1.3 Manually performed vitreo-retinal eye surgery

Eye surgery can be divided in two parts: operations performed on the posterior (vitreo-retinal eye surgery) and anterior (like cataract surgery) part of the eye (figure 1.5). Although the anterior surgery is more commonly practiced, the more difficult posterior eye surgical interventions are considered a true test of eye surgery skill and expertise. Therefore, the focus will be on vitreo-retinal surgery. As the name implies, surgery is performed on the vitreous humor, retina and underlying structures.

Figure 1.5 gives an overview of the anatomy of the human eye. The light enters the eye through the cornea and pupil, is focussed by the lens and projected on the retina.

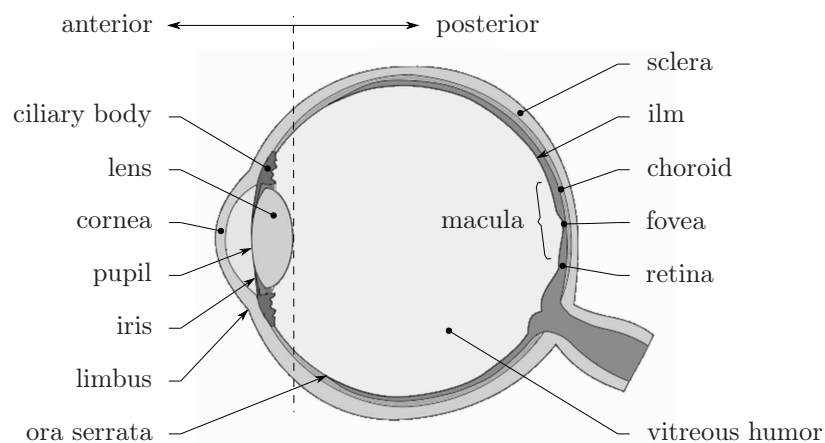


**Figure 1.5** / Anatomy of the human eye. Surgery can be performed on the posterior part as well as the anterior part. An explanation of the medical terms can be found in the nomenclature.

Surgery is performed not unlike MIS (figure 1.6). The instruments enter the eye through

surgeon made scleral openings, often fitted with a cannula. The 25 and 23 Gauge instruments are respectively 0.52 and 0.64 mm in diameter. The length is 30 mm.

Instruments are manipulated in four DoFs, three rotational DoFs ( $\varphi$ ,  $\psi$  and  $\theta$ ) and a translation in axial direction ( $z$ ). Actuation of for example a forceps can be considered as the fifth DoF. The entry point acts as pivoting point and therefore the lateral movements ( $\varphi$  and  $\psi$  rotation) are inverted. During surgery, the surgeon is limited to use two five DoF instruments at any given time.

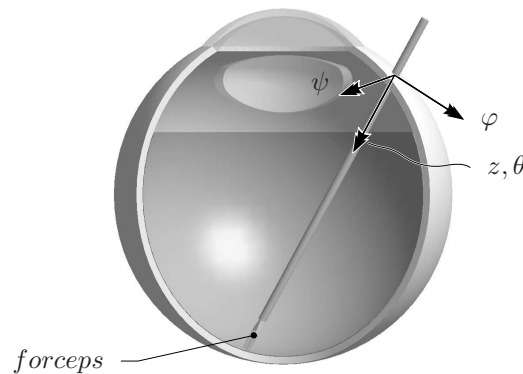


**Figure 1.6** / An instrument can be manipulated in four DoFs (three rotations and a translation in axial direction) through the surgeon made scleral opening. The operation of for example a forceps is the fifth DoF.

Before surgery can start the patient is covered by a sterile drape (figure 1.7). The drape has a transparent window with a fluid collecting bag that fits over the eye. An adhesive layer fixates the window and prevents fluid (for example to moisten the eye) to seep over the patient's face. A small cut gives access to the eye. Subsequently, a speculum is placed. The speculum retracts the eyelids to give access to the eye throughout surgery. If possible only a local anesthetic is used to immobilize the eye and to suppress pain.

The surgeon is sitting in line with the patient (figure 1.7). The microscope gives a  $\approx 5$ -25 times magnified, stereoscopic view of the operation area. The microscope is provided with an assistant microscope tube and camera. The camera image is displayed on a monitor as visible in the upper left part of figure 1.7. Sterilization of the microscope is not possible and therefore it is covered with sterile plastic bags and caps. During surgery the surgeon has to focus alternately on the sclera (outside of the eye) and on the fundus (inside of the eye). Therefore, the microscope can be equipped with a wide angle fundus observation system to simplify this switch. When the device is placed below the lens the fundus is visible, when swung away the sclera is visible.

Characteristically, the manipulation of delicate intraocular tissues is required. The shortest force loop and highest accuracy is achieved by supporting the hands on the patient's forehead. Forces are below the detection limit of 0.06 N. This means that

surgeons must rely on visual feedback only. The use of a microscope is of great importance, resulting in a static and non ergonomic body posture.



**Figure 1.7 /** Overview of an eye surgery procedure. The surgeon is sitting in line with the patient (covered by sterile drapes). The microscope gives a magnified, stereoscopic view of the operation area.

In summary, vitreo-retinal eye surgery is characterized by:

- small and inverted instrument movements
- manipulation of delicate, micrometer range thick intraocular tissue
- instrument forces below the human detection limit (visual feedback only)



- maximum use of two instruments simultaneously
- static and non ergonomic body posture

## 1.4 Goal of this thesis

There are different robotic systems to assist a vitreo-retinal eye surgeon, but none of these systems is suitable for a complete intervention or able to cover all issues as stated above. Therefore, the EyeRhas project<sup>1</sup> has been started in 2006. The project was initiated by M.D. de Smet, AMC UvA. The project's goal of EyeRhas is to make a technology demonstrator of a master-slave system with force feedback for vitreo-retinal eye surgery. Figure 1.8 gives an overview of the required subsystems.

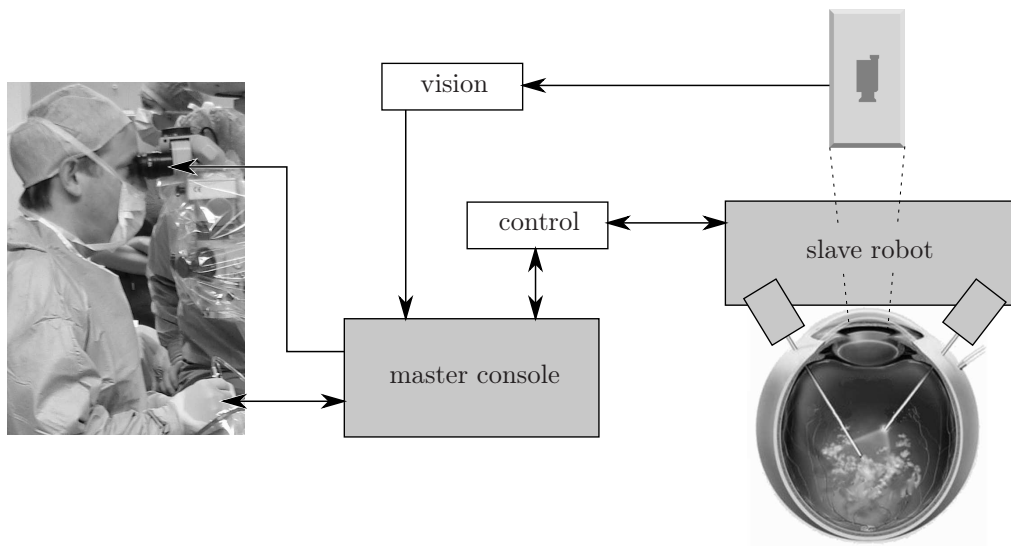


**Figure 1.8** / Overview of the subsystems within the EyeRhas project. The goal is to realize a master-slave system with force feedback. The system will be suitable for a complete intervention and will enhance the surgeon's dexterity.

The goal of this thesis is to design and realize a master console with haptic interfaces to control the instrument manipulators of a microsurgical slave designed for vitreo-retinal surgery. This master with force feedback and scaling of hand motions extends existing surgical skills to perform surgery on the vitreous humor and retina.

The surgeon uses the master to control the slave. The slave is placed near the patient and manipulates the instruments via two or more instrument manipulators (IMs). The

---

<sup>1</sup>Project partners: TU/e, TNO and AMC UvA. EyeRhas is an acronym for: Eye Robot for Haptically Assisted Surgery.

slave is an easy to place, table mounted device. The IMs can be positioned over either the left or right eye. Each IM has an automatic onboard instrument changing system as different instruments are used during surgery. The design and realization of the slave is the work of H.C.M. Meenink and is performed in a parallel Ph.D. research project at the TU/e [57–59].

Vision and control are two additional subsystems of EyeRhas.

Control comprises the electronics and software between the master and slave hardware. This subsystem consists of the power supplies, motor amplifiers, data acquisition system and control hardware with appropriate control algorithms and safety features. At least a bilateral control scheme is required for the position tracking and force feedback between master and slave.

With a master-slave system there can be an increase in the distance between surgeon and patient. This means that the surgeon can not use the binoculars of the microscope. Implementation of an alternative system for the visual feedback is covered in the fourth subsystem: vision.

## 1.5 Master console

The master console must be suitable for the diversity of instruments and entry point locations which may be required by the various surgical tasks to be accomplished in the posterior part of the eye. A compact and easy to place design makes it possible to place it near the patient and results in a short setup time and a quick removal in case of a complication.

The console includes a 3D visualization system to represent the microscope or endoscope images and two five DoF haptic interfaces for an intuitive, bimanual operation of the instruments. Downscaling of the hand motion at the master system results in a more accurate instrument movement compared to manually performed surgery. Dexterity is further enhanced by the feedback of the augmented interaction force between instrument and intraocular tissue.

A high quality force feedback requires a haptic interface with a high stiffness, a low moving mass/inertia, no backlash and low disturbance forces. A high device stiffness and a low inertia result in a high eigenfrequency and a high control bandwidth, which is necessary for a correct representation of the contact stiffness between instrument and environment. A low inertia makes it also easier to perform a specific task and reduces fatigue. A backlash free design results in a higher control stability and enables, together with low disturbance forces, a more precise manipulation of the instrument. Low disturbance forces are also desired as they directly interfere with the upscaled instrument forces.

None of the commercially available five and six DoFs haptic devices is found to be suitable for the master console. The two main reasons are a limited structural stiffness and a workspace which is too small. The same is valid for the more dedicated devices as applied within surgical simulators for the training of minimally invasive surgery tasks. Therefore, a new haptic interface with 5 DoFs is designed for the console.

The force feedback also depends on the actuator, transmission and control algorithm. Single DoF master-slave systems are realized to study the impact of these aspects and to derive an additional set of requirements for the multi DoF haptic interface.

## 1.6 Outline of the thesis

The requirements for the master console will be formulated in chapter 2. These requirements are derived from the different vitreo-retinal eye surgery procedures as observed in the operating room. Chapter 2 will also give an overview of existing robotic systems for vitreo-retinal eye surgery and haptic devices.

Several concept designs for the master console are presented in chapter 3. Differences are found in the placement in the operating room, the visualization system and the arrangement of the degrees of freedom of the haptic interface. A table mounted console with a 3D display and a dedicated haptic interface is finally selected.

Two one degree of freedom master-slave setups are realized to gain insight in the requirements as well as the control of the haptic interface. Chapter 4 is about the design, realization and control of these single DoF setups.

The design and realization of a preliminary version of the haptic interface is discussed in chapter 5. The purpose of this interface is to verify the different design considerations. Based on the results, a concept design is made for an improved version of the interface. The design of this interface is discussed in chapter 6.

The conclusions and recommendations are given in chapter 7.

# Design requirements of the master console

---

**Abstract /** Vitreo-retinal eye surgery encompasses vitrectomy, membrane peeling and the repair of a retinal detachment. Different instruments are used, each with a specific workspace and accuracy. Manipulation of an instrument requires a haptic interface with five degrees of freedom. A dedicated, stylus based interface provides a sufficient large bandwidth for an adequate force feedback and allows the surgeon to manipulate the different eye surgery instruments in the entire workspace with the desired accuracy.

The first part of this chapter is about the background of vitreo-retinal eye surgery and about robotically assisted eye surgery. Haptic interfaces as part of the master console are discussed in the second part.

## 2.1 Vitreo-retinal eye surgery

Vitreo-retinal surgery can be divided into three distinct phases which occur quite consistently in most cases: vitrectomy, membrane peeling and the repair of a retinal detachment. Figure 2.1 gives a typical hand operated instrument layout during surgery on the left eye. The layout is mirrored for surgery on the right eye.

A surgeon uses two instruments simultaneously, which requires two scleral openings. The openings are often fitted with a cannula. One is placed left and one is placed right, at a distance of 3-4 mm from the limbus (the border of the cornea and the sclera) to prevent penetration of the retina or the ciliary body. This layout provides a large working area and a natural simultaneous operation with the left and right hand. The exact angle with respect to the transverse plane varies between approximately  $0^\circ$  and  $30^\circ$ . It is chosen in such way that the instrument movements are obstructed as little as possible by the contours of the eye socket or the nose of the patient.

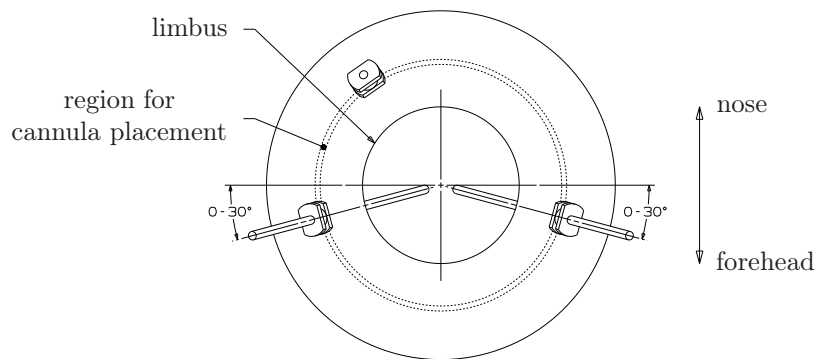


**Figure 2.1** / The typical instrument layout during manually performed eye surgery on the left eye (top view). Cannula placement is only possible at a distance of 3-4 mm from the limbus. The instruments are placed under an angle of 0-30° with respect to the transverse plane (see figure A.1). The exact position depends on the geometry of the patient's face and in particular the patient's nose. The third cannula is for the infusion.

Besides the two entry points for the instruments, an infusion is required to maintain a correct eyeball pressure and to replace the fluid which is removed during surgery (for example the vitreous humor during a vitrectomy). An infusion is often used in combination with a (third) cannula, but as it is stationary, it is also possible to place it directly in a scleral opening. There are self retaining infusions and infusions which have to be sutured on top of the sclera. The advantage of a third cannula is that the infusion and an instrument can be interchanged, giving a larger working area. The scleral openings are made with a relatively short stiletto (figure 2.2).

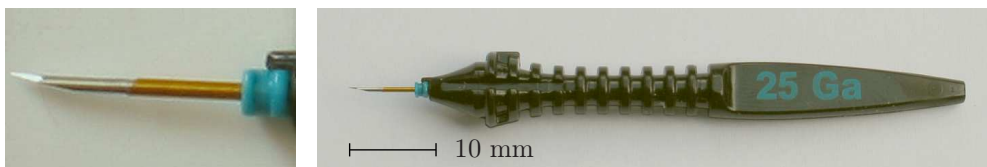


**Figure 2.2** / Stiletto with cannula. The tip has a trapezoidal cutting section. The protrusion between handle and cannula acts as a rotation lock to ease the cannula placement in the incision.

The stiletto combines two functions in one device. First, the incision is made with the trapezoidal cutting section at the tip. Thereafter, the stiletto is pushed through another 5 mm to place the cannula, which is on the stiletto shaft. The protrusion between handle and cannula enables rotation of the cannula to simplify the actual placement. The cannula stays in the incision after retraction of the stiletto. The incision angle of 30-40° [24] results in a self sealing incision, so no suturing is required after the removal

of the cannula when the procedure is completed. The cannula, while installed, gives a well defined, easy to retrieve entry point. It also protects the sclera against the instrument movements and it reduces friction, which ensures a more precise control of the instrument.

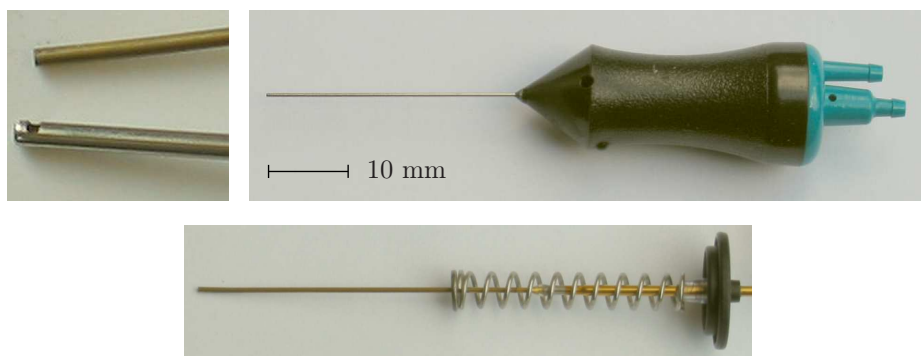
### 2.1.1 Vitrectomy

Removal of the vitreous humor is the initial and most frequent procedural step. In most cases it is done to improve visualization and instrument manipulation during subsequent vitreo-retinal surgical tasks, but it can also be done for intraocular foreign body removal or to reduce retinal traction.

Vitrectomy requires the use of a vitrectome and sometimes an endo-illuminator. The vitrectome is a combined suction and cutter device. The endo-illuminator is a light fibre.

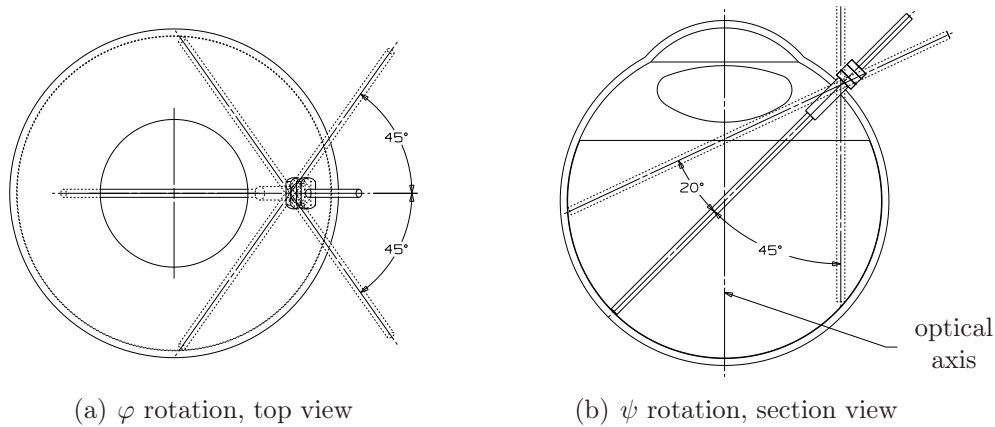
#### Vitrectome

The vitrectome (figure 2.3) consists of two coaxial tubes. The outer tube is mounted to the handpiece and has a lateral port opening just behind the tip. The inner tube moves in an axial direction and acts as a guillotine. The tip of the inner tube is slightly bent to guarantee a correct cutting of the vitreous humor. Actuation is done pneumatically with a cutting rate of up to 2500 cuts per minute. Aspiration is also done via this tube. Cutting of the gel like liquid streamlines the aspiration, but also reduces the possibility of retinal traction. Such traction could result in a retinal tear.



**Figure 2.3 / Vitrectome.** The intraocular part consists of two coaxial tubes: an outer tube and a plunger. The lateral port opening and the tip of the plunger are visible in the left picture. Actuation and aspiration is done via the two hose fittings on the right. The pneumatically actuated plunger is visible in the picture at the bottom.

A vitrectome needs a large working area as the whole posterior cavity is filled with the vitreous humor. In practice, there are two limitations. Firstly, it is desirable that the  $\varphi$  and  $\psi$  rotations are limited to  $\pm 45^\circ$  with respect to a radially inserted instrument. This is to protect the sclera against excessive deformation. Secondly, a direct contact between the instrument shaft and lens is unwanted, as damage can result in a cataract.



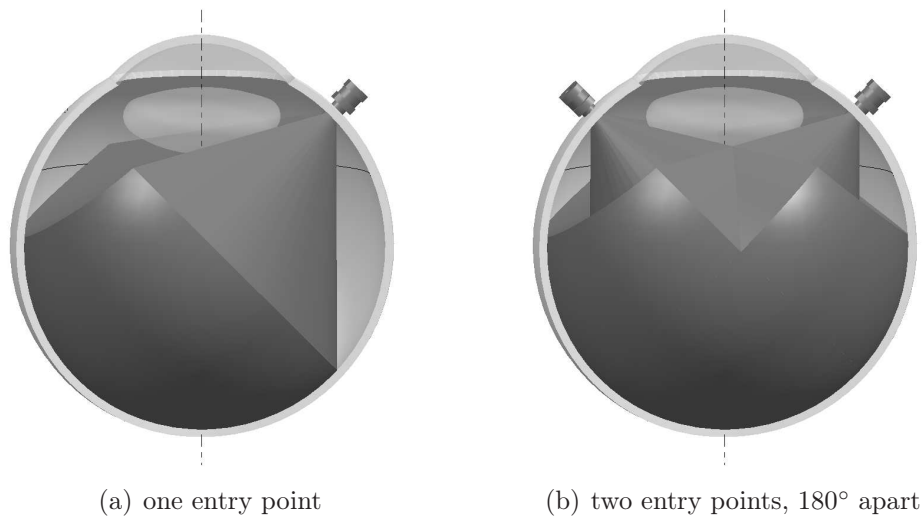
**Figure 2.4** / Range of motion for a rotation about the principal  $\varphi$  and  $\psi$  axes.

Figure 2.4 gives an overview of the working area for the two principal axes of rotation. The eyeball diameter is set to 24.2 mm [4, 15]. The nominal instrument angle varies between  $43\text{--}48^\circ$  with respect to the optical axis as it depends on the distance between cannula and limbus (3-4 mm). Here, an angle of  $45^\circ$  is used. With this, the distance between instrument tip and the anterior boundary of the retina (ora serrata) becomes 5 mm. It complies to the range of 3.5-5.5 mm as specified in [84].

Based on these figures, the working range becomes  $\pm 45^\circ$  for  $\varphi$  and  $-20^\circ/+45^\circ$  for  $\psi$ . However, as the  $\psi$  range does not allow surgery sideways of the lens, it is preferable to increase this to  $-35^\circ/+45^\circ$ . The  $z$  movement is identical to the eyeball diameter of  $\approx 24$  mm. In  $\theta$ , the range is  $360^\circ+$ . In practice, it is only limited by the two silicon tubes between instrument and the vitrectomy console.

A 3D view of the working area achieved is visible in figure 2.5(a). Not all areas are covered. There is a gap at the left side of the lens and a second gap in the area around the cannula and from there downwards to the retina. A large part is caught up by using the second entry point (figure 2.5(b)) and by using the infusion cannula. Visualization of the peripheral areas is only possible by rotation of the eyeball to get a more sideways view.

The regions which are not covered are near the ora serrata. For the most vitrectomy procedures this is not important as it does not interfere with the central vision. Microscopic imaging of this region is also limited. If required, these regions are reached



**Figure 2.5** / The workspace of the vitrectome for one and two entry points. The area is defined by the lens and a maximum instrument angle of  $45^\circ$  with respect to a radially inserted instrument.

by indentation of the eyeball. This technique is discussed in section 2.1.3).

### Endo-illuminator

During a vitrectomy, a direct contact between vitrectome and retina is to be avoided. Therefore, the surgeon uses an endo-illuminator to improve visualization of intraocular tissues and to create a visual depth cue in addition to the stereoscopic image of the microscope. An endo-illuminator (figure 2.6) consists of an optical fibre, which is connected to an external light source. The intraocular part of the fiber is protected by a thin-walled circular tube. The illuminator can have a straight or bent tip.



**Figure 2.6** / Endo-illuminator with straight tip and optical light fiber. The fiber is connected to an external light source.

The additional depth cue is based on a casted shadow. This shadow differs from the shadow generated by the external light source of the microscope, as it is visible sideways instead of behind the instrument (figure 2.7). This means that the shadow moves along with the vitrectome. Out of the distance between the shadow and instrument tip, the



surgeon can estimate the distance between instrument and retina.

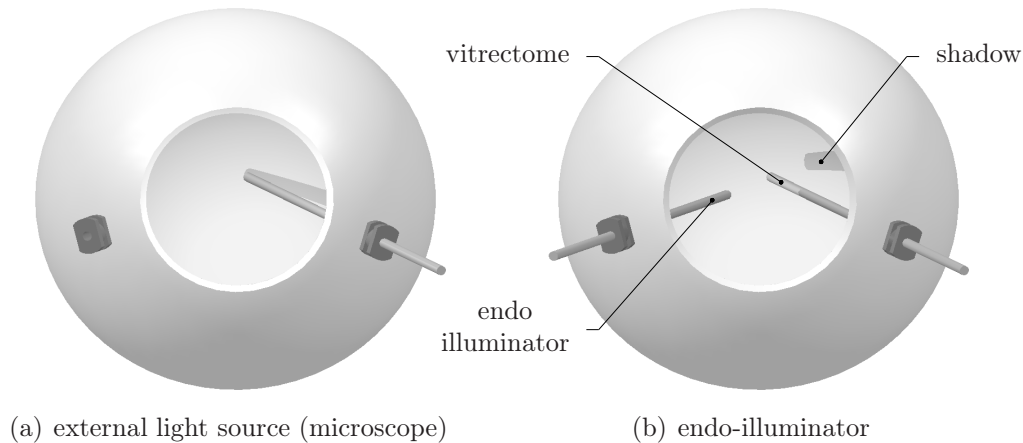


**Figure 2.7 /** Shadow of the vitrectome as created by the external light source of the microscope and as created by the endo-illuminator. The advantage of a sideways placed shadow (endo-illuminator) is that it acts as an additional depth cue to estimate the distance between the tip of the vitrectome and retina (here: 3 mm).

The illumination probe must be in front of the vitrectome to create a shadow on the retina. This means that the working range of the illuminator is within that of the vitrectome.

### 2.1.2 Membrane peeling

Membrane peeling is the removal of a membrane on top of the retina. There are two kinds of membranes: an epiretinal and an internal limiting membrane (ILM). The first is a sort of scar tissue that can grow on top of the retina, as result of a microscopic damage of the retina. Shrinkage of the vitreous humor with accompanying retinal traction can be the cause for this damage.

The ILM is a normal tissue layer that separates the retina from the vitreous humor. Like the epiretinal membrane, it can start to contract and distort the retina and the vision as well. When the traction becomes too large, a retinal detachment can be the result.

The removal of an ILM requires the same operating techniques and instrumentation as an epiretinal membrane removal. A vitrectomy is often performed first, before a start is made on the actual peeling procedure.

As the intraocular membranes are nearly transparent, they are first stained with a special dye (indocyanine green) to make them more easily distinguishable from the

underlying retina. This fluid is injected in the vitreous cavity, whereafter the excess dye is removed by aspiration. A pick and forceps are the specific instruments for the removal of a membrane. An endo-illuminator is used for an improved depth perception.

### Pick

There must be a start before the membrane can be grasped with a forceps. If necessary, this start is made with a pick. The pick in figure 2.8 consists of a tube and a knife. The bent shape of the knife eases scraping, as the tip of the blade is not perpendicular, but parallel to the retina. The knife can be retracted in the tube to ease the insertion through the cannula. The surgeon controls the extension and retraction of the blade via the button on the handle.

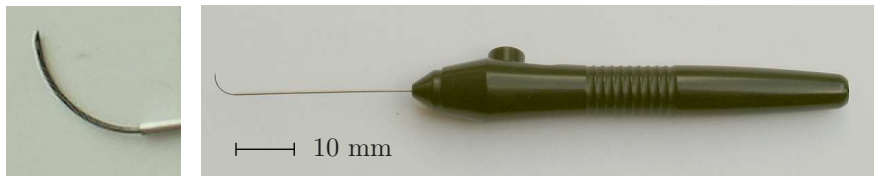


**Figure 2.8** / Extendable pick, shown extended. The surgeon controls the extension and retraction of the blade via the button on the handle. A detail photo of the blade is visible in the left picture.

### Forceps

Once a start is made with the pick, the membrane is grasped with the forceps and gently peeled away from the retina by making small circular movements. Peeled membrane tissue is removed directly via the cannula or by the use of the vitrectome.

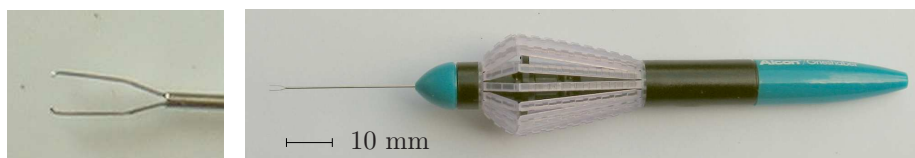


**Figure 2.9** / Forceps with straight jaws. Operation of the forceps is done by squeezing the umbrella style, synchronously moving levers on the handpiece.

Actuation of the forceps (figure 2.9) is done by a squeezing finger motion. A mechanism inside the handpiece translates this motion in an axial movement of the tube. The tube is pushed over the jaws of which the distal ends are fixed. The wedge shaped geometry

of the jaws makes that the forceps closes.

The actual peeling is often concentrated on the macula. This area is responsible for central vision and has a diameter of approximately 2.5 mm. It is situated on the visual axis, 5° apart of the optical axis. The macula is within the workspace of the vitrectomy procedure. Manipulation of a forceps or pick requires steady hand movements, even during actuation, as the surgeon has to remove membranes with a thickness down to 2 μm without damaging the underlying retina.

### 2.1.3 Repair of a retinal detachment

The retina, which lies at the inside of the posterior eye wall, may occasionally become detached from the choroid (a layer of blood vessels). A detachment can be initiated by a traction force from the vitreous humor or a membrane and therefore the repair is often done in combination with a peeling procedure following a vitrectomy. The surgical aim in this case is the reestablishment and fixation of the retina to its underlying layers. This must be done as quickly as possible, because otherwise the detached part of the retina will lose its ability to perceive light. There are different techniques depending on the size and precise location of the detachment.

Reestablishment is achieved from the inside by injection of gas ( $\text{SF}_6$  or  $\text{C}_3\text{F}_8$ ) or silicon oil. The gas or oil presses the retina back into place and prevents fluid from collecting under the retina. An alternative to bring the layers back together is by scleral buckling. This is done from the outside by placing a silicone band around the eye.

After bringing the retina back into position it has to be sealed against the eye wall. This is done cryogenically or by laser. Both techniques initiate a scar reaction to seal the break. In the first case, a freezing probe is pushed from the outside of the eye directly over the retinal defect. In the second case, an endolaser probe is inserted via a cannula. As the focus is on minimally invasive vitreo-retinal eye surgery, only the endolaser will be discussed.

#### Endolaser

The construction of an endolaser is similar to an endo-illuminator. The difference is that the optical fibre is connected to a laser source. The working area is the direct neighborhood of the retina and goes up to the ora serrata. With two or three entry points it is not possible to cover this complete area (see figure 2.5(b)), without indentation of the eyeball.

Indentation is done with a cotton bud or an equivalent object (figure 2.10). As the retina is brought more inwards it is possible to perform a task without interfering with the eye lens. Another advantage of indentation is that the visual feedback improves, as

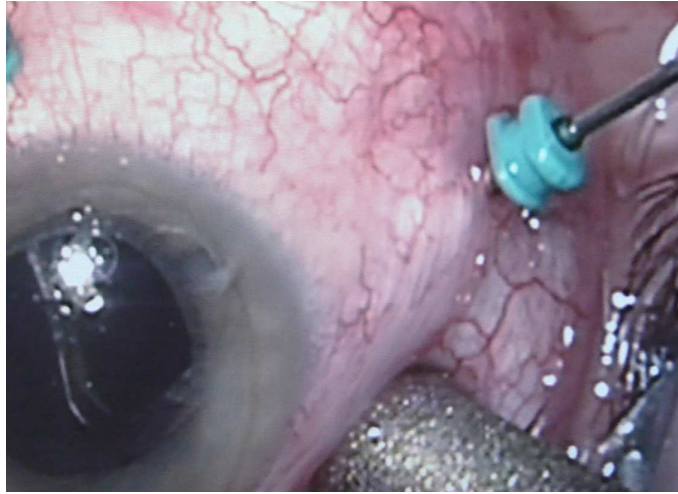


**Figure 2.10** / Indentation of the eyeball to reach the region near the ora serrata.

the workspace moves towards the optical axis. Drawback is the stretching of the ocular structures.

#### 2.1.4 Requirements with respect to the instrument movements

It is sufficient to look to the vitrectome and forceps to derive the specifications for the instrument movements. The vitrectome is of importance as this instrument has the largest range of motion, thereby defining the robot range. The forceps needs the highest accuracy for the peeling of the sometimes only  $2\ \mu\text{m}$  thick membrane. According to [74], a surgeon is able to keep an instrument within  $49\pm 30\ \mu\text{m}$  (RMS error) from a desired location. This value can be seen as the highest achievable accuracy. In  $\varphi$  and  $\psi$  direction this equals an angle of 2 mrad or  $0.1^\circ$  ( $49\ \mu\text{m}$  over a 24 mm inserted instrument). For  $\theta$  the accuracy depends on the hand piece diameter (10 mm) of the vitrectome and pick. A movement of  $49\ \mu\text{m}$  over 5 mm (half the diameter) gives a rotation of  $0.6^\circ$ . The specifications for the instrument movements are summarized in table 2.1.

**Table 2.1** / Minimum requirements with respect to instrument movements. The DoFs are according to figure 1.6.

	$\varphi$	$\psi$	$z$	$\theta$	<i>forceps</i>
range	$-45^\circ/+45^\circ$	$-35^\circ/+45^\circ$	24 mm	$360^\circ+$	2.5 mm
accuracy	$0.1^\circ$	$0.1^\circ$	$50\ \mu\text{m}$	$0.6^\circ$	$50\ \mu\text{m}$

### 2.1.5 Visualization with microscope and endoscope

The microscope is used during most operations as it provides a stereoscopic view and as it has no limitations with respect to the resolution of the images. A 2D endoscope, on the other hand, has the ability to visualize the region between ciliary body and ora serrata and has the advantage that the cornea and eye lens opacity does not influence the image quality [83].

#### Microscope

The microscope is placed 15 cm above the patient's eye and gives a  $\approx 5$ -25 times magnified, stereoscopic view. The surgeon has to focus alternately on the sclera and on the fundus. This switch can be made by zooming and refocussing or via a wide angle fundus observation system, which is placed in one hand movement between the microscope and eye. The system can be combined with a contact lens and enlarges the field of view towards a maximum of  $125^\circ$ .

The microscope is equipped with a foot switch to adjust the focus, zoom and the position in the coronal plane (see figure A.1), parallel to the operating table.

#### Endoscope

Like a standard instrument, the entrance point of an endoscope is placed on 3-4 mm from the limbus. Manipulation of an endoscope is comparable to an endo-illuminator. The diameter of the endoscope is limited to approximately 1 mm to guarantee a good sealing and healing of the wound after surgery. As a result of the diameter, the resolution of the endoscope is limited to 20-30K pixels. Nevertheless, the viewing angle of  $110^\circ$  allows to visualize and to assess regions not covered by microscopic surgery [18, 25]. The surgeon has one free hand left, so he is able to perform surgery in these regions.

## 2.2 Robotically assisted eye surgery

Different approaches and devices can be found in literature to assist a surgeon during vitreo-retinal eye surgery. Classification is possible in four categories:

- hand held tools
- realized master-slave systems for eye surgery
- eye surgery with the da Vinci<sup>®</sup> surgical system
- recently performed studies on master-slave systems for eye surgery

### 2.2.1 Hand held tools

#### Steady hand

The Steady hand robot [89] (figure 2.11) is designed to extend a human's ability to perform sub-millimeter manipulation tasks.

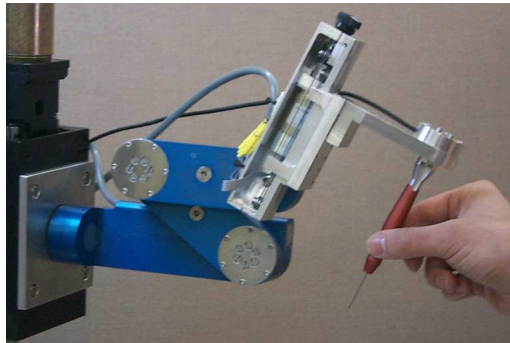


**Figure 2.11** / Steady hand. The instrument is held simultaneously by the surgeon and the robot. The system provides tremor filtering and force scaling.

The system consists of three parts: a 3 DoF base, a remote center of motion assembly and an instrument guiding assembly. Instruments are held simultaneously by the operator's hand and robot arm. The instrument and hand forces are measured and used to provide tremor-free positional control and force scaling. Instrument forces are scaled upwards with a factor 10 to 100.

The system is compact, is easy to place and enables a potentially cheaper implementation when compared to a master-slave system. Scaling of the positional motions is not possible with this device.

#### Micron

Another hand held tool is the Micron [3], figure 2.12. The Micron is designed to compensate physiological tremor and other unwanted movements. The main purpose is to be able to perform extremely difficult or impossible tasks like intraocular cannulation, which requires a tip positioning accuracy in the order of 10  $\mu\text{m}$ .

The tool has an average diameter of 22 mm and is 210 mm long and is held like a normal instrument. A tri-axial accelerometer and three ceramic rate gyros are mounted at the back end of the instrument handle to measure the translation and rotation. The unwanted  $\varphi$ ,  $\psi$  and  $z$  movements of the intraocular part of the instrument are canceled by moving the tool tip in opposite direction. Actuation of the tip is done by three piezoelectric actuators.



**Figure 2.12 / Micron.** The tooltip is actuated to compensate for tremor.

Recently, some improvements have been made with respect to sensor placement, dimensions and weight [46].

### 2.2.2 Master-slave systems already realized

Two master-slave systems are realized at the end '90s: one at the Jet Propulsion Laboratory (JPL) and one at the department of mechanical engineering at the Korea Advanced Institute of Science and Technology (KAIST).

#### JPL RAMS

The JPL Robot Assisted MicroSurgery (RAMS) system is intended to enhance the fine motion skills of surgeons. In contrast with the hand held tools, this system has the ability to scale hand motions to precise instrument movements. RAMS comprehends a master interface, a slave manipulator, software, servo control and an electronics subsystem [16]. The master and slave are visible in figure 2.13.

The slave arm measures approximately  $\varnothing 25$  mm x 250 mm and has an almost hemispherical workspace. It is mounted to a cylindrical base housing of  $\varnothing 120$  mm x 180 mm that contains the drives for the 6 DoFs of the arm. All DoFs are cable driven. According to [21] it can position a surgical instrument with an accuracy of 12  $\mu$ m.

The master is kinematically similar to the slave and has the same dimensions. The master arm is mounted to a box shaped housing. The gear ratios for the master arm are lower than for the slave arm to guarantee backdrivability. The workspace is 50x50x50 mm<sup>3</sup> and the resolution is 25  $\mu$ m.

Reported is a successfully conducted removal of a particle ( $\varnothing 0.4$  mm) from a simulated eyeball. This procedure is performed without force reflection from the slave.

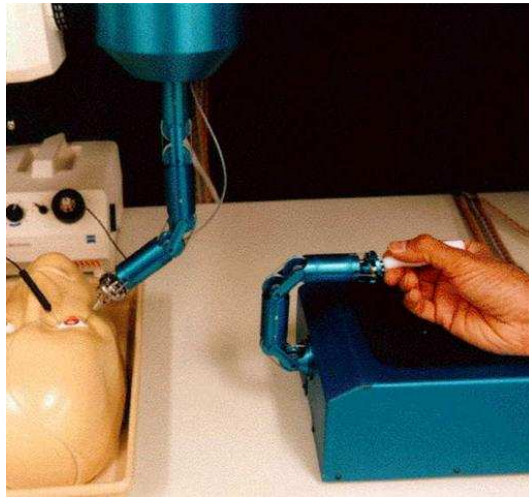
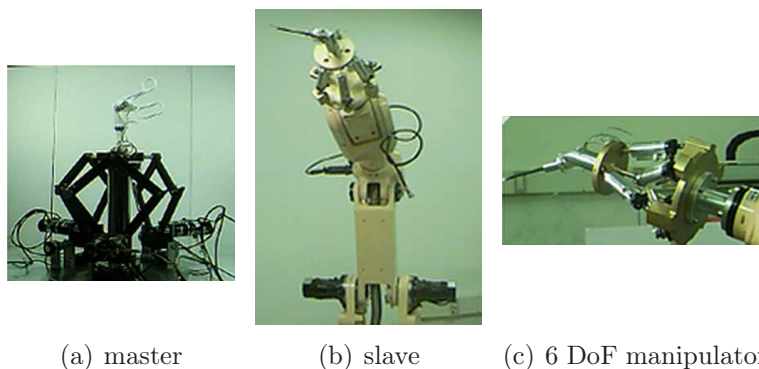


**Figure 2.13** / The RAMS setup. The slave manipulator at the left manipulates an instrument in 6 DoF, according to the hand motions of the surgeon as measured by the master interface.

### KAIST Microsurgical Telerobot System

As the name implies, the telerobot system is designed for microsurgery tasks. Requirements are based on the analysis of task and tool motions for four different microsurgery fields, including ophthalmic surgery [45]. The master and slave are visible in figure 2.14.



(a) master

(b) slave

(c) 6 DoF manipulator

**Figure 2.14** / The Microsurgical Telerobot System. Large slave motions are made with an industrial robot. Small and precise instrument motions are made with the 6 DoF manipulator.

The slave is a combination of a 6 DoF parallel type manipulator with interchangeable instruments and an industrial robot. The 6 DoF manipulator is for the small and precise instrument motions. The workspace is set on  $20 \times 20 \times 20 \text{ mm}^3$  with an accuracy of  $20 \mu\text{m}$



and a maximum force of 1 N. Large motions are made with the industrial robot.

The workspace of the 6 DoF master is set on 200x200x150 mm<sup>3</sup>, which allows for downscaling of the hand motions [44]. The parallel kinematic layout is constructed out of three five-bar mechanisms. The end effector is built like a surgical instrument handle. In contrast with the RAMS master, this device has a 6 DoF force/torque sensor to measure the interaction force between the user and end effector. This to cancel out disturbance forces and to improve the force feedback.

### 2.2.3 Eye surgery with the da Vinci

A feasibility study of eye surgery with a da Vinci<sup>®</sup> surgical system is described in [11]. An overview and a detail view of the setup is visible in figure 2.15.

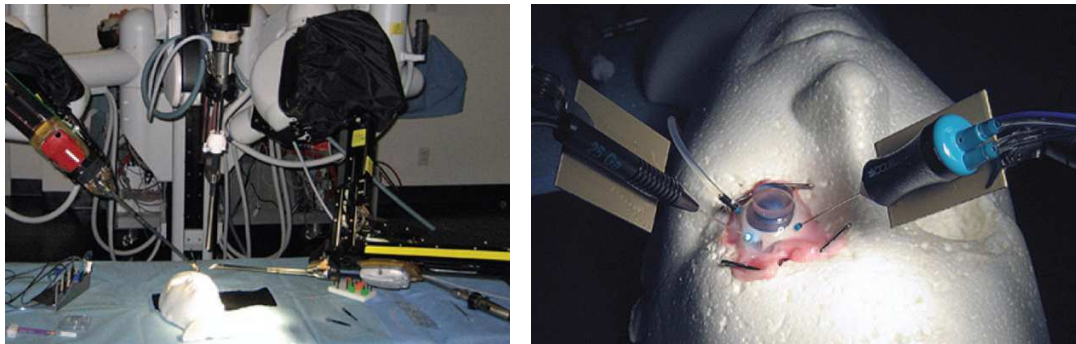


**Figure 2.15** / Eye surgery with the da Vinci<sup>®</sup>. Standard instruments for manually performed eye surgery are adapted for the da Vinci<sup>®</sup> by gluing them on a metal plate.

The study comprises an intraocular foreign body removal in the anterior part of the eye and a vitrectomy. The robotically performed tasks in the posterior part are, besides the vitrectomy itself, the placement as well as the removal of the cannulas and infusion. Besides a vitrectome, an endo-illuminator is used. Both instruments are adapted for the da Vinci<sup>®</sup> by gluing them on a metal plate (figure 2.15, right). The plates are grasped by standard robotic forceps. A magnetic rack is used as storage and gives the possibility to change instruments during surgery. Visual feedback is provided by the 3D endoscope of the da Vinci<sup>®</sup>.

It is concluded that the da Vinci<sup>®</sup> robotic system has the dexterity to perform delicate ocular manipulations, but also has its limitations: inferior visual feedback compared with an ophthalmic microscope, lack of force feedback and a reduced maneuverability due to the discrepancy between the virtual trocar point (the pivoting point of the robotic forceps) and the scleral opening.

As the virtual trocar point is not placed in the scleral opening, there is no restriction on the lateral movement of this point. This means that the surgeon must take care not to make these movements, otherwise large scleral forces can be induced.

A micro manipulator system is designed [63] to deal with the reduced maneuverability and to eliminate lateral forces on the sclera. The manipulator is mounted to the shaft of a da Vinci<sup>®</sup> tool. The system is based on two  $x$ - $y$  translation stages, which allows a  $\varphi$  and  $\psi$  rotation of  $31^\circ$  about the entry point.

### 2.2.4 Studies on master-slave systems

Two recent studies on dedicated systems for eye surgery are found at the Columbia University, New York, USA and the University of Tokyo, Japan.

#### Columbia University

The focus of this research is on the design and evaluation of a slave that combines instrument manipulation with an orbital manipulation of the eyeball [94, 95]. The slave consists of a head mounted ring with two hybrid instrument manipulators. Each manipulator is based on a 6 DoF hexapod with on top an adjustable 2 DoF intraocular dexterity robot. The hexapod is designed for a  $\varphi$  and  $\psi$  working range of  $\pm 20^\circ$ . With the 2 DoF dexterity robot it becomes possible to work with extendable instruments, like the extendable pick as depicted in figure 2.8.

The relevance of an instrument manipulator based orbital manipulation is to improve vision in the peripheral area of the eye, to roll the silicon oil to the correct place on the retina during the treatment of a retinal detachment and to decrease operation time.

#### University of Tokyo

In [92] the design and feasibility of a realized master-slave system is discussed. The slave has a 5 DoF serial layout. The two main rotations (equivalent to the  $\varphi$  and  $\psi$  DoF) are made with a circular ball guidance, each with a range of motion of  $\pm 50^\circ$ . An alternative slave with a parallel hexapod layout is presented in [64]. This design differs from a Stewart platform as manipulation is not done via linear actuators inside the rods, but by displacing the base joints. The  $\theta$  rotation of the instrument is made with an additional motor on top of the hexapod. The parallel layout limits the  $\varphi$  and  $\psi$  rotation to  $\pm 10^\circ$ .

A 7 DoF haptic interface is used to control the slave. The interface [86] consists of a 3 DoF hybrid mechanism for the  $x$ ,  $y$  and  $z$  motions with on top the three rotations in

a serial layout. The 7th DoF is the operation of the gripper. Force feedback is provided on the three translational DoFs and the gripper.

Visual feedback is provided via a high definition LCD display and a prism lens viewer, in a setting comparable to a normal ophthalmic microscope during manually performed surgery. The microscope images are captured by a high definition 3D camera.

The main conclusion with respect to the system (slave with serial layout, [92]) is that tasks can be performed 5-10 times more accurately than during manually performed surgery.

### 2.2.5 Conclusions

Based on the requirements for manually performed eye surgery and on the systems as discussed above, a robotically assisted vitreo-retinal eye surgery system has to fulfil the following criteria:

- have a sufficiently large range of motion with a high precision
- bimanual operation with two (extendable) instruments simultaneously
- usable with a microscope and endoscope
- possibility to change instruments
- safe and intuitive operation
- scaling of hand motion and tremor filtering
- force feedback with force scaling
- compact and easy to place

The range of motion must comply to the specifications in table 2.1. For enhanced dexterity, the accuracy must be in the order of 10  $\mu\text{m}$  [73] or better, as it eases working with the thin membranes and enables such tasks as cannulation of retinal blood vessels. Therefore, the system must be equipped with a scaling functionality in combination with tremor filtering. There must be at least two instrument manipulators to enable bimanual surgery. Preferable is a third manipulator to hold an illuminator or endoscope as it enhances dexterity even further. The manipulators must not obstruct the light path of the microscope and must not interfere with a wide angle fundus observation system. An instrument changing system is required to perform the different vitreo-retinal tasks and to make the setup suitable for a complete intervention.

The most secure way to manipulate an instrument is when the manipulator has a kinematically fixed rotation point (virtual entry point), placed in the scleral opening of the eye. In this way, an instrument can never exert a lateral force on the sclera.

For the six DoF devices, like the hexapod based manipulators, the unwanted lateral movements must be suppressed by the control loop. The less secure situation is seen by the feasibility study with the da Vinci<sup>®</sup>, as the surgeon has to take care by himself not to exert any forces on the sclera. Assessment of this is only possible via visual feedback, through which the surgeon has to focus on the inside and outside of the eye simultaneously.

An intuitive control of the instruments and an upscaled force feedback increases safety. An intuitive, natural control is achieved when the hand motions comply with the motions of the instrument as seen via the microscope or endoscope. This reduces the chance of making an erroneous movement. With force feedback, the surgeon can work more precisely in the direct neighborhood of the retina, even when the image quality is limited.

Finally, the master console and slave manipulator must be compact and easy to place. This guarantees a short setup time and a quick removal in case of a complication.

**Table 2.2** / Qualitative appreciation of the different robotically assisted eye surgery systems.

	Steady hand	Micron	JPL Rams	Kaist telerobot	da Vinci <sup>®</sup>	Columbia slave	Tokyo serial robot	Tokyo parallel robot
range of motion (slave)	+	n/a <sup>1</sup>	0	0	-	-	0	-
bimanual	+	+	+	?	+	+	+	+
microscope	+	+	+	+	-	+	+	+
endoscope	+	+	+	+	+	+	+	+
automatic instrument changing	-	-	-	+	+	-	-	-
safety (entry point)	+	n/a <sup>1</sup>	0	0	-	0	+	0
intuitive	-	-	+	-	+	n/a <sup>2</sup>	+	+
scaling of hand motions	-	-	+	+	+	n/a <sup>2</sup>	+	+
force feedback	+	-	?	?	-	n/a <sup>2</sup>	-	-
compact/easy to place	+	+	+	-	-	+	0	0

+: complies/ 0: does not comply, but within margin/ -: does not comply

?: no information available

n/a<sup>1</sup>: not applicable as it is a handheld device

n/a<sup>2</sup>: not applicable as the system does not include a master

Table 2.2 gives a qualitative appreciation of the different robotically assisted eye surgery systems. None of the systems can be used for a complete intervention as the range of motion is not sufficiently large nor does it have an automatic instrument changing mechanism. Force feedback is also an issue.

A dedicated system of reasonable size, suitable for a complete intervention and with force feedback will be designed within the EyeRhas project. This thesis covers the design of the master console. The design of the slave manipulator is described in [57–59]. The haptic interfaces are the most important parts of the master console.

## 2.3 Haptic devices as part of the master console

A haptic interface with at least 5 DoFs is required to take full control of the instrument motions in vitreo-retinal eye surgery. Force feedback is needed in the four main directions. Force feedback for the forceps is also desirable as membranes are to be grasped and tissues are to be manipulated during surgery. In this regard, the perception of holding a membrane is useful.

Different generic haptic devices are commercially available. Therefore, it is worthwhile to investigate if these systems can be used in the master console.

### 2.3.1 Generic haptic desktop devices

The commercially available devices with at least 4 DoF position sensing and force feedback are:

- Delta 6, Force Dimension [27]
- Virtuose™ 6D35-45 and 6D desktop, Haption S.A.[34, 35]
- Freedom 6S and Freedom 7S, MPB Technologies, Inc. [62]
- 5 DoF Haptic Wand, Quanser, Inc. [72]
- Phantom® Premium 1.5/6DOF, Premium 1.5 High Force/6DOF and Premium 3.0/6DOF, Sensable Technologies, Inc. [80, 81]

These devices have in common that they are used in combination with impedance control (see chapter 4).

#### Force Dimension

The haptic device (figure 2.16(a)) of Force Dimension is based on a 3 DoF delta parallel robot mechanism that allows for manipulability in  $x$ ,  $y$  and  $z$  direction. This kinematic



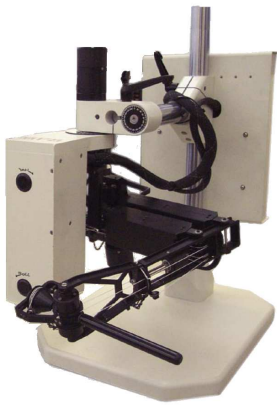
(a) Force Dimension Delta.6 [27]



(b) Haption Virtuose™ 6D Desktop [35]



(c) Haption Virtuose™ 6D35-45 [34]



(d) MPB Technologies Freedom 6S [62]



(e) Quanser 5 DoF Haptic Wand [72]



(f) Phantom® Premium 1.5/6DoF, Sensable Technologies [80]



(g) Phantom® Premium 3.0/6DoF, Sensable Technologies [81]

**Figure 2.16** / Commercially available haptic devices.

structure consists of three parallelograms, each placed under  $120^\circ$ . These parallelograms allow the platform to freely translate, while remaining parallel to the frame. Each parallelogram can be moved via a segment and capstan drive. Six rods suppress all the degrees of freedom between the segments and end effector.

Sensing of the rotations and force feedback in these DoFs is implemented via three motor/encoder combinations in the end effector. A recent update of the Delta 6 has resulted in a three times higher  $x$ ,  $y$  and  $z$  resolution.

### **Haption S.A.**

The Virtuose™ 6D desktop device (figure 2.16(b)) consists of a base with three articulated links to the end effector. The kinematic layout of the 6D desktop device differs from the Delta as each of the three arms is provided with two degrees of freedom: an articulated motion and a rotation around the longitudinal axis.

The Virtuose™ 6D35-45 (figure 2.16(c)) has a workspace corresponding to the movements of a human arm. The device has a hybrid kinematic layout, based on a four bar mechanism. Three motors and encoders are integrated in the base for position measurement and force feedback in  $x$ ,  $y$  and  $z$ . The three rotational DoFs are placed on top of the parallelogram.

### **MPB Technologies, Inc.**

A hybrid layout is also applied in the Freedom 6S (figure 2.16(d)). The system consists of a position stage and a orienting mechanism. The orienting mechanism comprises two five bar linkages and is mounted to a table-top holding stand. The position stage is mounted on top of the orienting mechanism and is based on a four bar mechanism. As the name implies, the rotations are covered by the orientating mechanism, the translations are covered by the position stage.

The Freedom 7S is identical to the Freedom 6S, but has an extra feature: an interchangeable force feedback scissors grip.

### **Quanser, Inc.**

The Haptic Wand (figure 2.16(e)) has five DoFs, three translations and two rotations. Not covered is the rotation around the longitudinal axis of the end effector. The system is based on a dual pantograph arrangement. Each pantograph is driven by two DC motors located at the base joints. The end effector is connected to the end points of the pantographs.

The  $z$  movement of the end effector is made by an up and downwards rotation of the pantographs. Force feedback is created by two additional motors in a redundant setup.

### **Sensible Technologies, Inc.**

The kinematic structure for the  $x$ ,  $y$  and  $z$  DoF is identical to that of the Virtuose™ 6D35-45 device (four bar mechanism). Actuation and position measurement is done via an capstan drive. The  $\varphi$ ,  $\psi$  and  $\theta$  dof are stacked on top of the four bar mechanism.

The range of motion of the Premium 1.5 (figure 2.16(f)) complies to lower arm movements (pivoting at elbow), the workspace of the Premium 3.0 (figure 2.16(g)) complies to full arm movements (pivoting at shoulder). It is possible to equip the devices with a 7th DoF end effector. The Premium 1.5 is also available as a high force variant, which can generate a 4.4 times higher translational force than the standard version.

### **Device properties**

Table 2.3 gives an overview of the properties of the mentioned devices. Not included in this table are the Virtuose™ 6D35-45 and Premium 3.0, as a full arm movement based workspace is not practical for eye surgery.

### **Device selection**

The haptic interfaces as compared in table 2.3 are provided with a knob shaped end effector (Delta 6 and Virtuose™ 6D desktop) or a stylus (other devices). A strategy to manipulate the instruments at the slave side is by mapping the  $x$ ,  $y$  and  $z$  translation and one rotation of the end effector knob (Virtuose™ 6D desktop and Delta 6) or stylus (other devices, see figure 2.17(a)) to the position and  $\theta$  orientation of the instrument tip. It is to be expected that a stylus will give the most natural feeling, as it can be grasped like a hand held instrument. There must be a downscaling of at least five times to achieve the accuracy of 10  $\mu\text{m}$ .

It is also possible to map the three rotations and the longitudinal movement of the stylus to the four DoFs of the instrument (figure 2.17(b)). An intuitive working environment is the result, as the hand movements are identical to the instrument movements as seen via the microscope or endoscope. Implementation of this approach on the six DoFs devices requires that two DoFs are constrained in such way that the stylus rotates about a virtual entry point. This means that the  $\varphi$  and  $\psi$  rotation is coupled with a translational movement of the pivot point of the stylus. Scaling of the hand motions in lateral direction is achieved by the ratio between the length of the intraocular part



**Table 2.3** / Properties of the different haptic desktop devices [27, 35, 62, 72, 80].

	Delta 6	Virtuose™ 6D Desktop	Freedom 6S	Haptic Wand	Premium 1.5/6DOF	
DoFs	6	6	6	5	6	
footprint [mm]	700x400	∅300	250x250	≈300x400	330x250	
workspace [mm]	$x$	∅360	(sphere)	170	381	
	$y$	300		220	250	267
	$z$			330	450	191
workspace [°]	$\varphi$	40	35	170	297	
	$\psi$	(3x)	(3x)	130	260	
	$\theta$			340	335	
force [N] (cont./max.)	$x$	20/-	3/15	0.6/2.5	1.4/8.5	
	$y$			2.3/7.7		
	$z$			2.1/7.0		
torque [Nm] (cont./max.)	$\varphi$	0.2/-	0.14/0.5	0.11/0.37	0.23/0.75	0.19/0.52
	$\psi$	(3x)	(3x)	0.09/0.31	0.25/0.81	0.19/0.52
	$\theta$			0.04/0.15	-	0.05/0.17
stiffness [N/mm]	14.5	2.5	2	6	3.5	
stiffness [Nm/rad]		2	4/2.5/0.2			
resolution [μm]	30	15	2		30	
resolution [°]	0.04	0.004	0.001		0.002	
friction [N]			0.04		0.04	
friction [mN/m]			5/2/1			
moving mass [kg]			0.13		0.14	
inertia [g/m <sup>2</sup> ]	$\varphi$		0.04			
	$\psi$		0.03			
	$\theta$		0.003			

compared to the distance between the place where the surgeon holds the stylus and the virtual entry point.

Each approach has its own requirements with respect to the workspace. For manipulating in a orthogonal way, the workspace must be spherical and must have a diameter of at least 125 mm (5 times the eyeball diameter). The  $\theta$  range of the stylus must be in the order of  $\approx 180^\circ$  as the human hand does not allow for larger rotations.

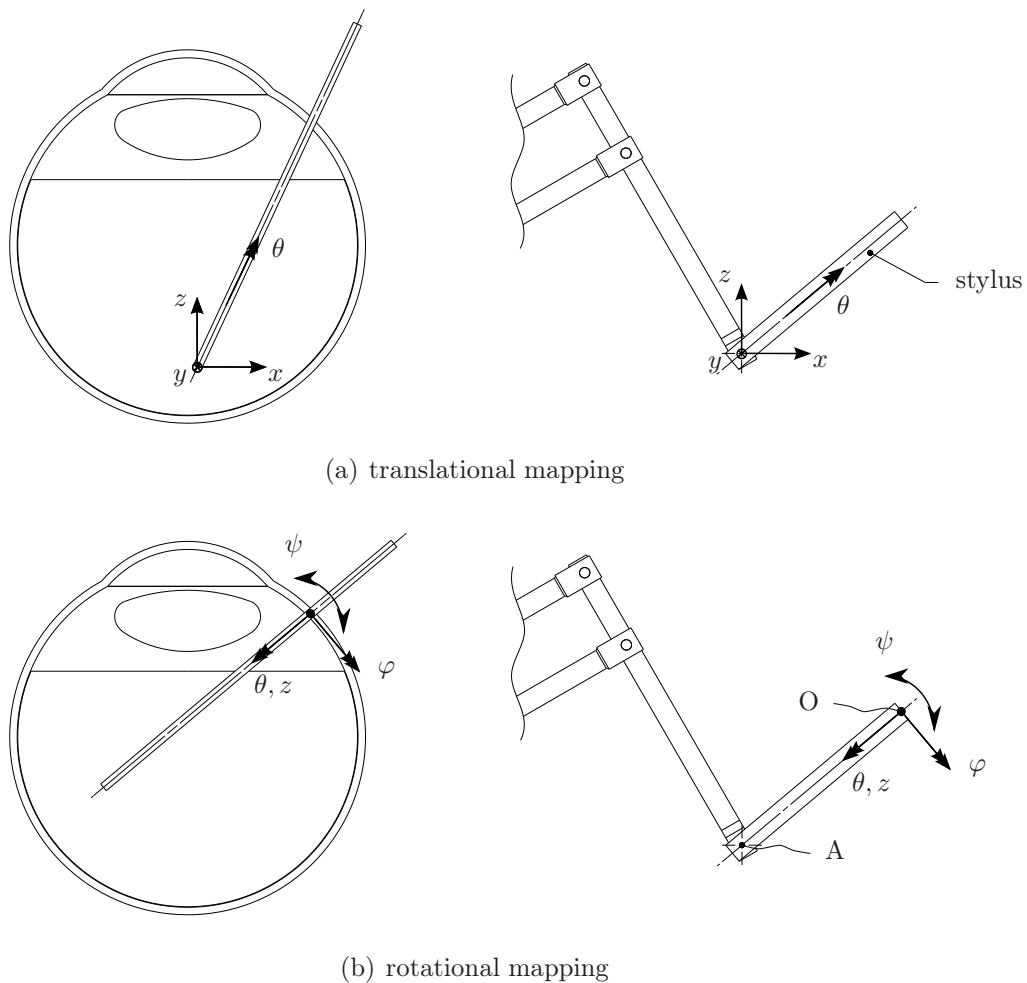


**Figure 2.17** / Two strategies for the mapping between the DoFs of the haptic device and the instrument. The user grasps the stylus near the pivot point A. Point O is the virtual entry point.

A jogging mode (combination of a position and velocity control) can be implemented to take full control of the  $360^\circ + \theta$  rotation of the instrument. The alternative approach requires a minimum working range of  $\pm 45^\circ$  for  $\varphi$  and  $\psi$ ,  $180^\circ$  for  $\theta$  and 125 mm for  $z$ .

Only the Freedom 6S and the Phantom<sup>®</sup> 1.5/6DoF have a workspace that is large enough for vitreo-retinal eye surgery procedures. The stiffness of these devices is 2 N/mm and respectively 3.5 N/mm (table 2.3). These values are low compared to the minimum stiffness to represent a hard contact. For eye surgery it is not directly necessary to represent a hard contact, but a low structural stiffness has also a negative impact on the eigenfrequencies of the devices. With a moving mass of 0.13 kg for the Freedom 6S and 0.14 kg for the Phantom<sup>®</sup> 1.5, the (lowest) eigenfrequency is in the order of 20-25 Hz. This value will decrease to 15-20 Hz by implementation of the 7th DoF (operation of forceps) in the end effector.

There are two relevant bandwidths for a haptic interface. The first for the detection of the hand motions and the second for the force feedback. Hand motions are in the order of maximal 10 Hz [12] including reflexive actions. During surgery, motions are up to 2 Hz [33]. The requirements for force feedback are higher. Kinesthetic and proprioceptive force sensing requires a bandwidth of 20 to 30 Hz [13], but the perceptual bandwidth for vibrotactile stimuli goes up to 800-1000 Hz [10, 87]. According to [42], the best performance for size identification is reached at a force bandwidth of 40 Hz or higher.

The maximum bandwidth of the Freedom 6S and Phantom® 1.5 will be below 20 Hz. This is enough to sense hand motions, but too low for an adequate force feedback. It is to be expected that a higher device stiffness and a higher quality force feedback is achievable with a more dedicated 4+1 DoF device.

### 2.3.2 Haptic devices for minimally invasive surgery

More dedicated haptic devices are used within surgical simulators for the training of minimally invasive surgical tasks. Two examples are a laparoscopic simulator by Baumann et al. [5, 6] and a simulator for urological operations by Papadopoulos et al. [67].

The training simulator for urological operations has 5 DoFs. It is based on a four bar parallel linkage with on top a spherical joint. Force feedback is created via frame mounted motors and capstan drives. The different DoFs are decoupled. The kinematic layout prohibits a combined  $z$ - $\theta$  movement along the instrument axis and therefore this design can not be directly used for vitreo-retinal eye surgery.

The 4 DoF haptic interface of the laparoscopic simulator consists of a parallel mechanism for  $\varphi$  and  $\psi$ , with on top the  $z$  and  $\theta$  DoF. The parallel mechanism has a virtual trocar point for an invisible implementation of the hardware inside the torso of the artificial patient. The device requires two adaptations to make it suitable for vitreo-retinal eye surgery. In the first place, a fifth DoF must be added for the control of the forceps. Secondly, the device must be mounted in such way that the pivoting point is placed above the surgeon's hand instead of below. It is also possible to improve the device stiffness further, as a virtual entry point representation is not needed.

### 2.3.3 Conclusions

An intuitive working environment is obtained when the hand movements of the surgeon comply with the instrument movements as seen via the microscope or endoscope. This requires a stylus based haptic interface with at least four DoFs. The control of the instrument function, e.g. gripper, can be seen as an additional DoF. There exist two commercially available, stylus based devices which have a workspace sufficient large for

vitreo-retinal eye surgery. These devices are the Freedom 6S from MPB Technologies and the Phantom<sup>®</sup> 1.5/6DoF from Sensable Technologies. Both devices have six DoFs and each can be seen as a generic haptic device. The stiffness of these two devices is respectively 2 N/mm and 3.5 N/mm. The bandwidth will be below 20 Hz, were 20-40 Hz is recommended for force feedback.

A more dedicated four DoF haptic device can be more compact and will have less mechanical links and pivot points. A mechanism with a lower inertia and a higher structural stiffness yields a higher bandwidth. More dedicated devices are applied in trainers for minimally invasive surgery, but the design of these systems requires adaptation prior to use in vitreo-retinal eye surgery. Therefore, it is more obvious to make a new and integral design of a dedicated 5 DoF, stylus based haptic interface with the master console and a system for visual feedback. Common techniques like a parallel actuation via frame mounted motors and a transmission via a capstan drive are also worthwhile to investigate for this new dedicated haptic device. These techniques can be, for example, found in the haptic simulator for urological operations and the haptic devices from Sensable Technologies and Force Dimension.



## CHAPTER THREE

# Master console

---

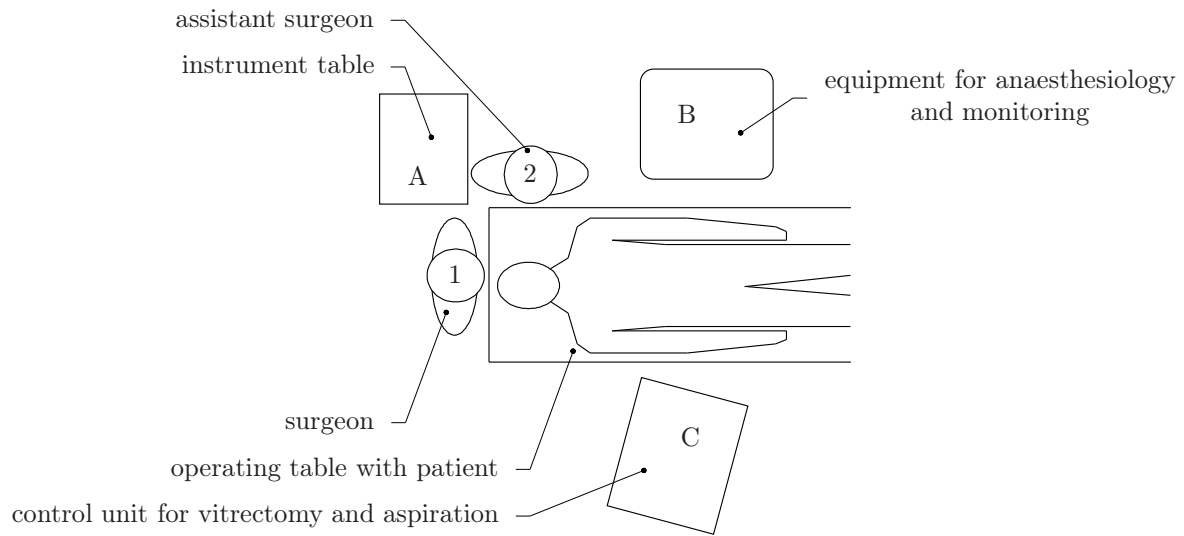
**Abstract /** This chapter discusses the layout of the master console. The new master console has two stylus based haptic interfaces to control the instruments and a stereoscopic screen for the visual feedback of the microscope and endoscope images. The console is compact and easy to place. It is mounted at the head of the operating table and fits in today's operating room arrangement.

The master console is used by the surgeon to operate the slave side instrument manipulators. When a master-slave system is introduced, it must fit in the current operating room (OR) setting, this to be able to perform other operations without master-slave system and to be able to switch back to manually performed surgery in case of a complication or malfunction.

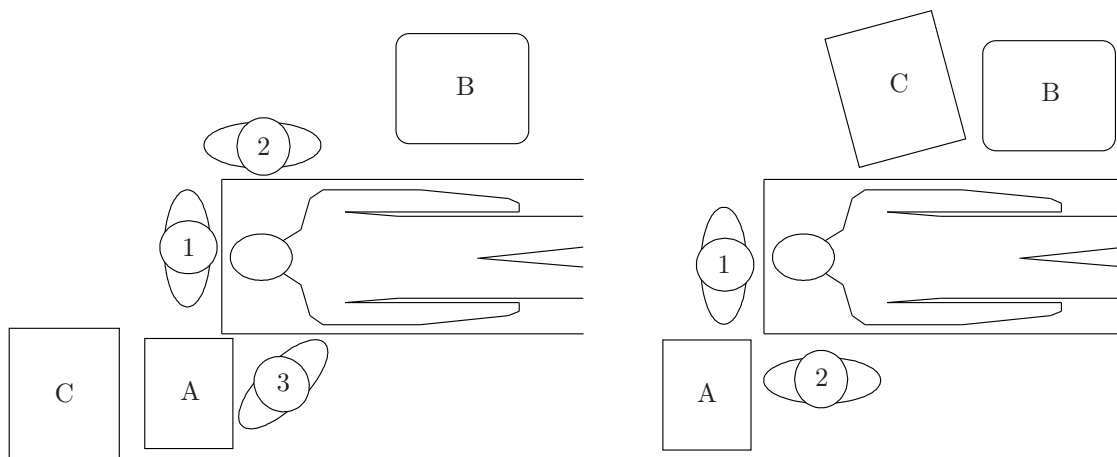
### 3.1 Surgical setup

Figure 3.1 gives three schematic overviews of the surgical setup as seen during manually performed surgery. The situations as drawn in figure 3.1(a) and (b) are for surgery on the left eye. Situation (c) is for surgery on the right eye. Surgery on the left eye is discussed first. Not drawn are the two foot switches: one to adjust the focus, zoom and the  $x$ - $y$  position (in the plane parallel to the operating table) of the microscope and one to adjust the cut rate and vacuum of the vitrectomy and aspiration device. The foot switches are placed under the operating table.

The surgeon is sitting in line with the patient. Equipment for anaesthesiology is placed at the left side of the table near the patient's forearm. The assistant surgeon is also sitting at the left. From this position the assistant is able to use the auxiliary microscope and is able to pass the required instruments to the surgeon (figure 3.1(a)). Handling of instruments can also be done by a third person, sitting at the right side of the table



(a) left eye, ZNA Middelheim



(b) left eye, AZM Maastricht

(c) right eye, CZE Eindhoven

**Figure 3.1** / Overview of the surgical setup for manually performed vitreo-retinal eye surgery. When the three layouts are compared, then the biggest difference is found in the location of the vitrectomy/aspiration device.

(figure 3.1(b)). Performing surgery with an additional assistant depends on the tasks and not on the hospital.

Surgery on the right eye requires a slightly different layout. Here, the assistant and instrument table are on the opposite side of the table. The vitrectomy and anaesthesiology consoles remain in the same place.

Comparing the three situations gives only one big difference: the location of the vitrectomy/aspiration device. It is found at the left side of the table, at the right side and right behind the surgeon. The first two locations are more practical, as it allows the surgeon to read off the settings more easily.

Based on the arrangements, a layout with the master placed sideways to the patient's head or in line with the operating table is obvious. In this way, it allows the surgeon to have eye contact and physical contact with the patient. This is seen as an important feature, as the surgeon can no longer feel the head movements of the patient.

A layout with the master console placed in line with the operating table (figure 3.2(a)) does not require any modifications to the operating room arrangement compared to manually performed surgery. The only requirement is some additional space at the head of the operating table. For a sideways placed master (figure 3.2(b)), it is desirable that the console is at the same side as the eye where surgery is performed on. This means that the assistant and surgeon have to change place and that the instrument table (if required) must be placed on the other side of the table.

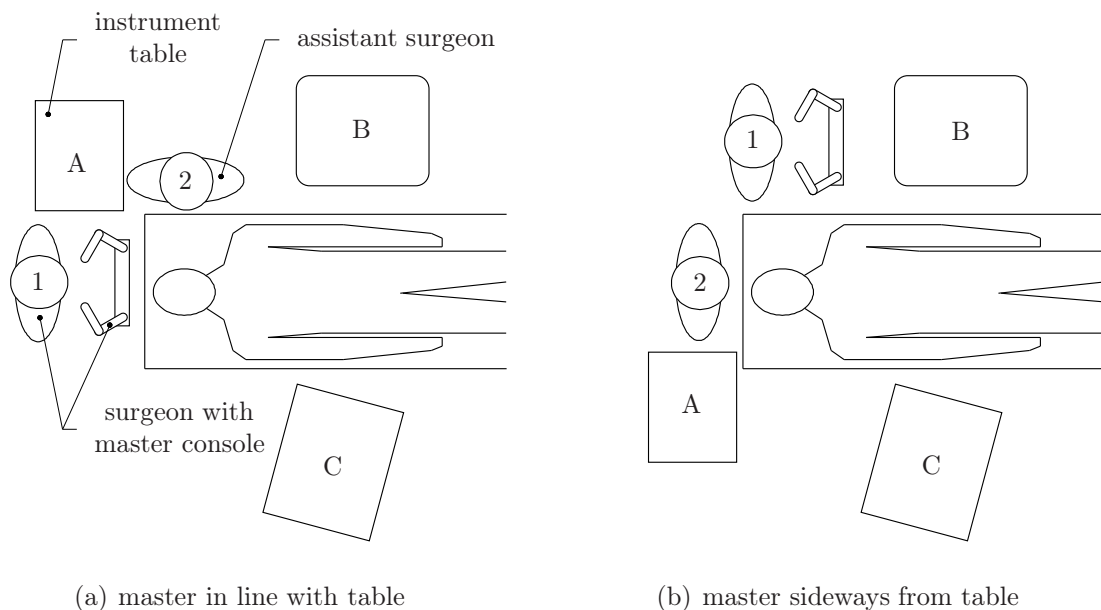


**Figure 3.2** / Surgical setups for robotically assisted vitreo-retinal eye surgery. The arrangements are based on the layout for manually performed surgery as applied in the operating room of ZNA Middelheim.



## 3.2 Main components of the master console

Figure 3.3 gives a schematic representation of a master console and its components. The surgeon controls the slave manipulators via the haptic interfaces. A 3D screen or an equivalent system provides the visual feedback of the microscope and endoscope images. The frame supports the individual components and must leave enough room for the foot switches to control the vitrectomy/aspiration device and microscope. The master console must provide a comfortable, ergonomic and intuitive working environment, as the surgeon performs several operations a day.

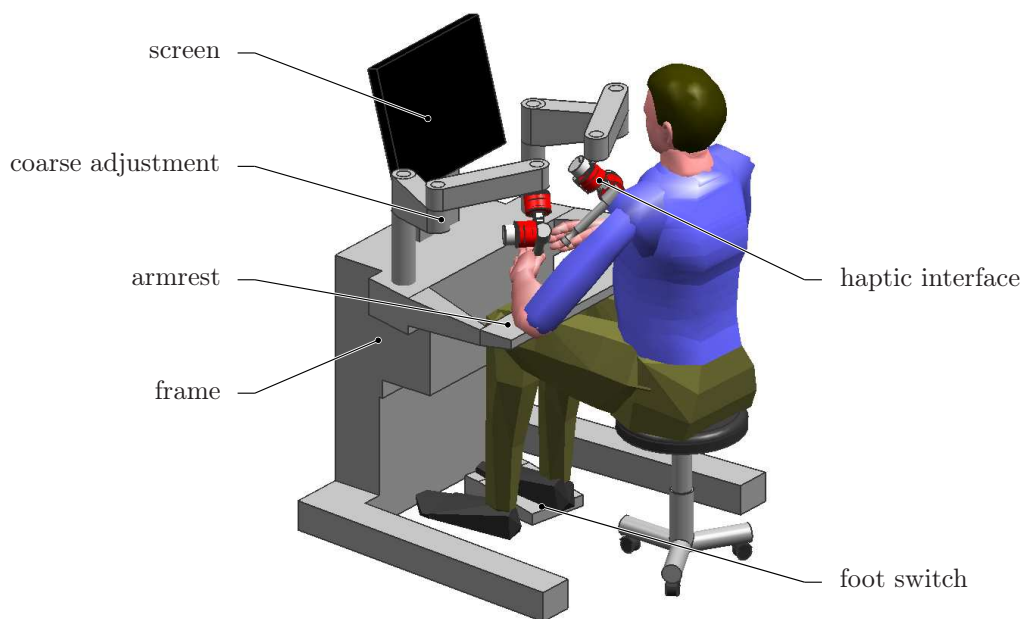


**Figure 3.3** / A concept layout of a freestanding master console. The main components are indicated.

The individual components of the master console are discussed in the following sections.

### 3.2.1 3D Visualization

The surgeon must have a correct depth perception of the operating area, especially during membrane peeling. Human depth perception is based on physiological and psychological depth cues [56]. Physiological cues are for example motion parallax and binocular disparity. Motion parallax is the movement of objects with respect to each other as result of the head movements of the observer. Binocular disparity is the difference in the images as seen with the left and right eye. Depth information is extracted from these differences. The second category, the psychological or empirical

cues are based on the observer's experience. Examples are shadows, relative size of objects and the interposition of objects in a scene.

The two most important depth cues for eye surgery are binocular disparity and shadows as created by the endo-illuminator (figure 2.7). Other cues like interposition and relative size are not relevant, as there are no other objects in the eye that can act as reference for the small and precise instrument motions in the direct neighborhood of the retina.

A surgical stereoscopic microscope has one primary objective lens whereafter two individual light paths are directed towards the left and right eye piece of the binocular tube. The two light paths image the posterior part of the eye at slightly different angles. This difference in angle results in the binocular disparity and a stereoscopic view.

With a master console, there can be an increase in the distance between surgeon and patient. This requires that the stereoscopic microscope images are directed in an alternative way to the surgeon. This is also necessary when the console is placed sideways of the operating table. An alternative visualization system can also be used for the representation of the endoscope images.

There are different ways to display the 3D images [39, 56, 68]. Applicable for the master console are the (auto)stereoscopic displays and frame mounted binocular viewing devices. A cave or dome and head mounted displays are left out of consideration as they isolate the surgeon from the patient. A direct contact is of importance as it allows the surgeon to check the patient's condition and to intervene when the patient makes undesired head movements.

### **Stereoscopic displays and binocular viewing devices**

Stereoscopic displays (figure 3.4(a)) present the visual information for the left and right eye in an alternate (time sequential) or simultaneous (time parallel) way. In case of a sequential representation, the user has to wear active shutter glasses. The glasses are synchronized with the screen and block the right eye when the left image is displayed and the left eye when the right image is displayed. The time parallel systems work with polarization or with a color coding (anaglyph) technique. In the first case, the two images are polarized in a different direction. The images for the left and right eye are filtered out via passive polarized glasses. The second option requires that the user wears glasses with two complimentary colored lenses to filter out the images for the left and right eye.

Special active or passive glasses are not required for auto-stereoscopic screens (figure 3.4(b)). The separation of the left and right image is done by a mask or a lens array which is placed directly in front of the display. Each view is directed to its individual viewing window. The angle between the viewing windows and the interpupillary distance defines the location where the user can see the image in 3D. Some

auto-stereoscopic displays generate more than two viewing windows. These displays provide multiple viewing locations and allow multiple persons to experience the 3D effect simultaneously. The same technique can also be used for the implementation of motion parallax. A position between two viewing locations gives crosstalk between different views and reduces the perception of depth.

The third category, the binocular viewing devices (figure 3.4(c)), can be compared with the binoculars of a stereoscopic microscope. The working principle is identical to the Wheatstone stereoscope [96]. Two images are generated independently of each other on two separate screens or side by side on one single screen. The two images are directed to the left and right eye of the user. Binocular viewing devices require that the user keeps his head on a fixed position. In this way there is no cross talk between the images. A binocular viewing device is also implemented in the robot-assisted vitreo-retinal eye surgery system as designed at the University of Tokyo [92] and in the da Vinci<sup>®</sup> surgical system [40].

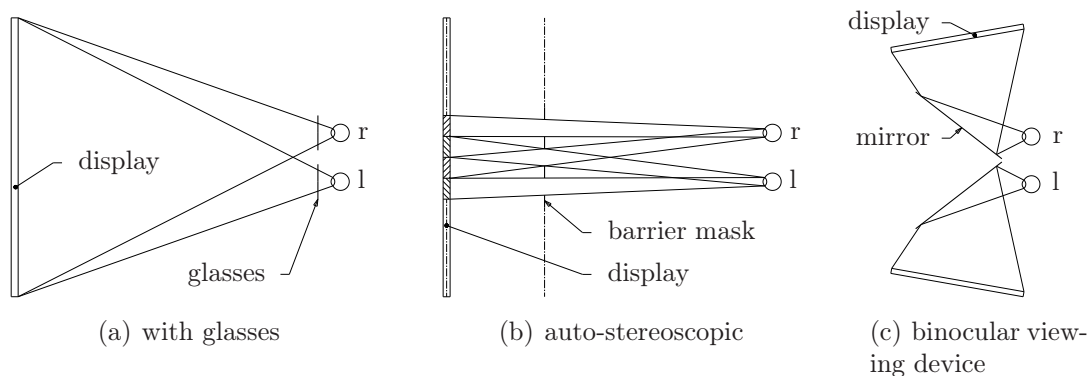


**Figure 3.4 / 3D display techniques.** The left and right eye of the user are indicated by l and r. Option (a) and (b) are based on a single display. Separation of the two images is done by glasses or via a barrier mask. Separation of the images is unnecessary in case of a binocular viewing device (c), as it has two individual light paths.

### Stereoscopic displays for the master console

The surgeon needs high resolution, full color images with a good contrast and brightness to distinguish the small intraocular structures, such as the retinal blood vessels. A high refresh rate is necessary for a flicker free image. Table 3.1 gives an overview of the different visualization systems for the representation of the endoscopic and 3D microscopic images. The resolution and refresh rate are compared to the specifications of the screen in 2D mode.

The non auto-stereoscopic displays give a reduction in contrast and brightness levels as

**Table 3.1** / Properties of the different 3D visualization systems. The resolution and refresh rate are compared to a screen in 2D mode.

	screen with shutter glasses	polarized screen	screen with anaglyphic encoding	auto-stereoscopic	binocular viewing device
glasses required	yes	yes	yes	no	no
crosstalk	a bit	no	yes	no <sup>1</sup>	no <sup>1</sup>
resolution	full	half <sup>2</sup>	half	half <sup>2</sup>	half <sup>2</sup>
refresh rate	half	full	full	full	full
full-color spectrum	yes	yes	no	yes	yes
contrast/brightness	reduced	reduced	reduced	normal	normal
fixed head position	no	no	no	yes	yes
direct contact with patient	yes	yes	yes	yes	reduced

<sup>1</sup>: within viewing window

<sup>2</sup>: full resolution with a dual screen setup

the glasses and filters in front of the display are not fully translucent. Polarization is preferable over anaglyphic encoding and time sequential imaging, as there is no crosstalk between the left and right picture which reduces the stereoscopic effect [68, 97]. Furthermore, with anaglyphic encoding it is not possible to accurately depict full-color images. The reduction in resolution can be overcome by a dual screen setup. According to [71], a polarized 3D screen improves the ergonomics compared to traditional microscopic viewing.

The image quality of an auto-stereoscopic display and a binocular viewing device is better, but these systems do not allow a sideways head movement of more than half the interpupillary distance (approximately 30-35 mm). A larger head movement results in loss of the stereoscopic effect. Head tracking could be a solution, but is still not good enough to compensate for the movements without noticeable delay [22]. The advantage of a binocular device over an auto-stereoscopic display is that it can be equipped with a head support. This makes it easier for the surgeon to keep his head in the correct viewing position. Therefore, a binocular device is preferable over an auto-stereoscopic display.

Compared to a binocular device, a screen gives a more ergonomic working environment,

as it does not force the surgeon to work in a static body posture. Furthermore, there can be a direct contact between surgeon and patient. On the other hand, a binocular viewing device has the highest image quality. Therefore, screen based and viewing device based concept layouts will be made for the master console.

### 3.2.2 Stylus based haptic interface

A stylus based haptic interface must have 5 DoFs to take full control of the instrument motions (figure 1.6). Two such interfaces are required for bimanual surgery. An intuitive working environment is created by placing the hand of the surgeon virtually on the tool shaft inside the eye of the patient (figure 3.5). This requires that each haptic interface stylus is oriented parallel to the slave tool. The stylus support point  $O$  corresponds with the entry point  $O'$  on the eye. The relative position of point  $O$  on both styli is placed in the same pattern as the entry points on the eye.

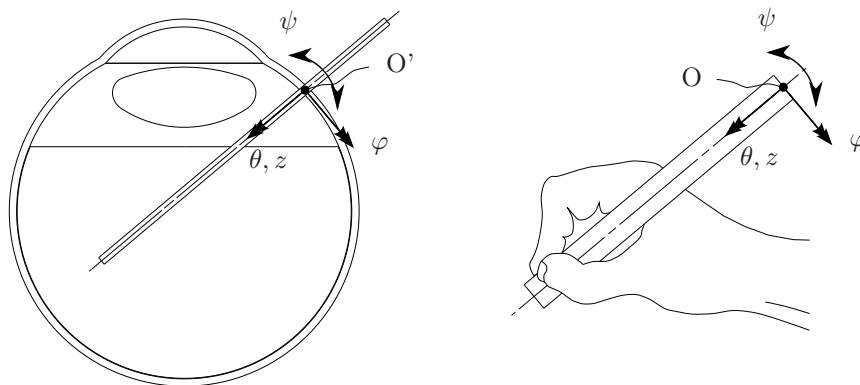


**Figure 3.5** / An intuitive working environment is created by placing the hand of the surgeon virtually inside the eye. The rotation point  $O$  is placed above the surgeon's wrist and represents the entry point  $O'$  of the instrument.

The rotation point  $O$  of the stylus in figure 3.5, is placed above the surgeon's hand. Compared to the layout in figure 2.17(b), this layout results in a more simple mechanical interface design and abandons the need for constraining some of the six DoFs to obtain the desired rotations and  $z$  translation of the stylus about the virtual entry point. This simplifies the control algorithms between interface and manipulator.

A stylus length in the order of 150-175 mm is desired to place the rotation point above the wrist of the surgeon (see also section 5.1). This gives a scaling ratio of approximately 1:7 in lateral direction, when working in the direct neighborhood of the retina. The scaling is calculated from the ratio between the length of the intraocular part of the instrument and the stylus length. Operation of the interface is done from wrist and

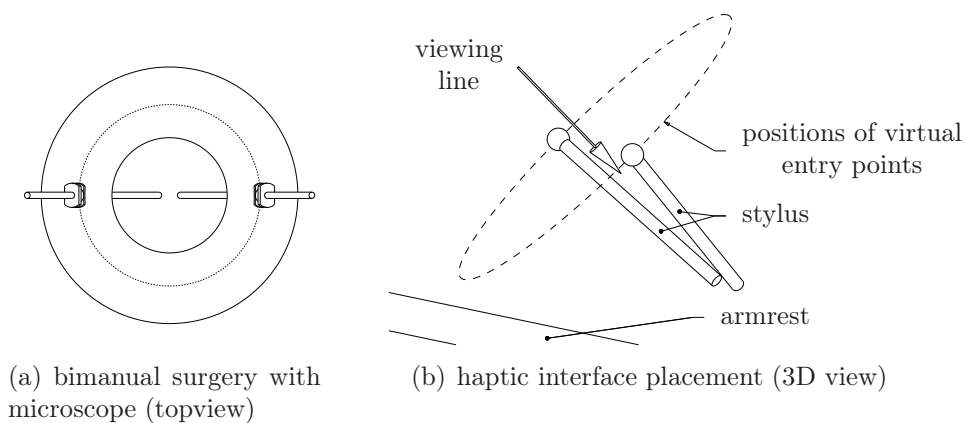
forearm movements.

The dedicated five DoF stylus based interfaces are each placed on a separate, additional coarse adjustment arm to create the intuitive pattern of the different entry point locations. The coarse adjustment can be designed with a high stiffness, so it will not influence the dynamical behavior and the force feedback of the interface stylus itself.

### 3.2.3 Coarse adjustment

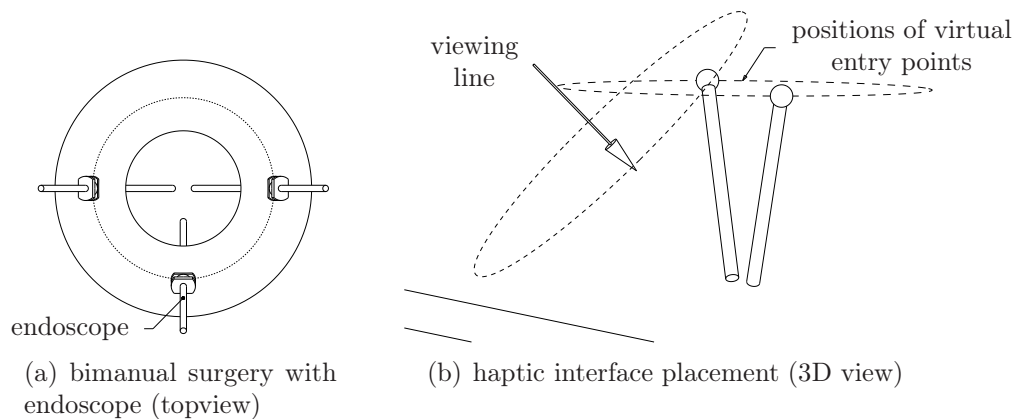
The location of the virtual entry point depends on the location of the scleral opening, the choice for a microscope or an endoscope and the angle of the optical axis of the microscope or endoscope with respect to the eye.

Figure 3.6 shows how a bimanual instrument layout (with one entry point at the left and one at the right, see also figure 2.1) in combination with a microscope is copied at the master side to achieve an intuitive working environment. The dashed circle indicates all possible virtual entry point locations and the arrow indicates the viewing line of the surgeon towards the stereoscopic display. Figure 3.7 shows the same situation, but now in combination with an endoscope. The difference with figure 3.6 is that the circle with the possible entry point locations is rotated upwards. The handheld part of the stylus remains on the same place for a radially inserted instrument.



**Figure 3.6 /** Setup of the haptic interfaces for surgery in combination with a microscope. The arrow indicates the viewing line of the surgeon towards the stereoscopic display. The haptic interfaces are collocated with this view to provide an intuitive way of working. The circle indicates the alternative positions of the virtual entry points.

Tilting of the eye ball to see the peripheral area of the eye or a  $\varphi$  or  $\psi$  rotation of the endoscope gives an analog effect. The virtual entry points rotate sideways or upwards/downwards with a maximum of  $45^\circ$ . A coarse adjustment with a hemispherical



**Figure 3.7** / Setup of the haptic interfaces for surgery in combination with an endoscope. The circle with the possible virtual entry point positions is rotated upwards, as the optical axis of the endoscope differs from the optical axis of the microscope.

workspace of  $\varnothing 350\text{-}400$  mm covers all possible positions of the haptic interface.

With a coarse adjustment it is sufficient to have two interfaces, even when an intervention is done with three or more instrument manipulators. In practice, switching between manipulators is done by locking one of the two operational manipulators, whereafter the accompanying interface is re-adjusted and used to control a further instrument or endoscope manipulator. The first instrument manipulator remains in its locked position until the surgeon decides to switch back to that manipulator. Mode switching can be initiated via foot pedals or via buttons on the interface itself. The need for only two manipulators simplifies the mechanical design and the electronic subsystem of the master console. It also gives more freedom around the surgeon's hands during manipulation.

The re-adjustment can be done manually (passive) or electrically (active). An active adjustment makes it easier for the surgeon to switch between different instrument manipulators. This feature is not strictly necessary as most interventions are done with only two manipulators via two scleral openings. This requires only one single adjustment during the setup phase of the system. For initial testing, a passive coarse adjustment is sufficient. An absolute position measurement system (for example via potentiometers) on the different coarse adjustment DoFs is desirable to detect a misalignment between interface and instrument.

### 3.2.4 Frame and ergonomics

The frame supports the individual components and must leave enough room for the two foot switches of the microscope and vitrectomy device. The free space inside the frame can be used for the master and slave drive electronics. Typical components are power supplies, motor amplifiers and a data acquisition system. Integration of these components inside the frame minimizes the number of cables and connections, compared to a freestanding electronic cabinet. This shortens setup time, increases reliability and makes it more practical to move the setup to another operating room. The frame can be freestanding like the concept in figure 3.3 or be more compact and attached to the headrest of the operating table.

The intended body posture during surgery is comparable with the posture during PC work. An armrest supports the surgeon's forearms to reduce fatigue. The chair, the armrest, the haptic interfaces and the display or binocular viewer must be adjustable in height to deal with the diversity in body dimensions and to guarantee an ergonomic way of working. For a table mounted master, it is possible to use the height adjustment of the operating table for this adjustment. This simplifies the mechanical layout of the console.

The optimal viewing range for a display is 0-30° below the horizontal sight line [90]. It is acceptable to extend this range to 0-45°. These values are of importance for the collocation of the visualization system with the haptic interfaces to achieve an intuitive layout. In comparison, during manually performed surgery there is a misalignment of 90° as the binoculars are placed horizontally and the objective lens of the microscope is placed vertically.

The body dimensions to derive the optimal height of the components are the sitting height, the eye position and the elbow height. These dimensions are based on the Dutch population [61] and summarized in table 3.2.

**Table 3.2** / Body dimensions of the Dutch population.

	male		female	
	mean [mm]	$\sigma$ [mm]	mean [mm]	$\sigma$ [mm]
sitting height	491	32	436	26
eye height <sup>1</sup>	833	37	772	34
elbow height <sup>1</sup>	261	28	243	30

1: measured from sitting height



### 3.3 Concept layouts for the console

Different concept layouts can be made for the master console. Summarized, the console must have a screen or a binocular viewing device, an armrest and two haptic interfaces, each with a coarse adjustment. The frame must be adjustable for an ergonomic body posture and must leave enough room for the foot switches of the microscope and vitrectomy device. The console can be freestanding or table mounted and can be placed in line with the patient or sideways of the patient's head. Figure 3.8 gives an overview of concept layouts for a freestanding master console. The consoles in figure 3.9 are table mounted.

The concept in figure 3.8(a) shows a configuration where the surgeon is sitting in line with the patient. The coarse adjustment covers the entire hemispherical workspace of approximately  $\varnothing 400$  mm. The screen is placed on such height that the arms of the coarse adjustment are never in front of the screen image. As a consequence of this screen position, the surgeon does not have a direct view on the patient. A direct visual contact is of importance as the surgeon can no longer feel the head movements of the patient via his hands.

Figures 3.8(b), 3.8(c) and 3.8(d) give three possible solutions. In (b) the screen is replaced by a binocular viewing device (viewer). The surgeon can look over the viewer to see the patient's head. This is possible, as a viewer is more compact and is placed directly in front of the surgeon's head. An alternative layout is visible in figure 3.8(c). Here, the console is placed sideways of the patient. The surgeon has to turn his head to the left to see the patient. The third option in (d) has a different approach. Here, the hemispherical workspace is divided in a left and right part. The screen is placed in the middle between both halves. Each coarse adjustment arm with haptic interface covers one half. This layout is suitable for the interventions with an instrument layout as visible in figure 2.1. In practice, this is the greater part of the interventions. It does not matter if a microscope or an endoscope is used during surgery.

Collocation of the microscope/endoscope image with the haptic interface gives the most intuitive way of working. This situation can only be achieved in the proposed concepts if the center of the image is placed at an angle of  $50-60^\circ$  below the horizontal sight line or if the haptic interfaces are placed on a larger distance from the surgeon. Both solutions are not desirable as it means that the surgeon has to work with extended arms or that the image is outside the optimal viewing range of  $0-45^\circ$ .

A freestanding master console will have a floor space of  $\approx 1 \times 1$  m<sup>2</sup> [70]. The distance between the surgeon and patient varies between 860 mm for the first concept and 600 mm for the third and fourth concept. The last concept has as consequence that it reduces the accessibility of the assistant(s) to the patient.

More compact are the table mounted consoles. A screen based console is visible in

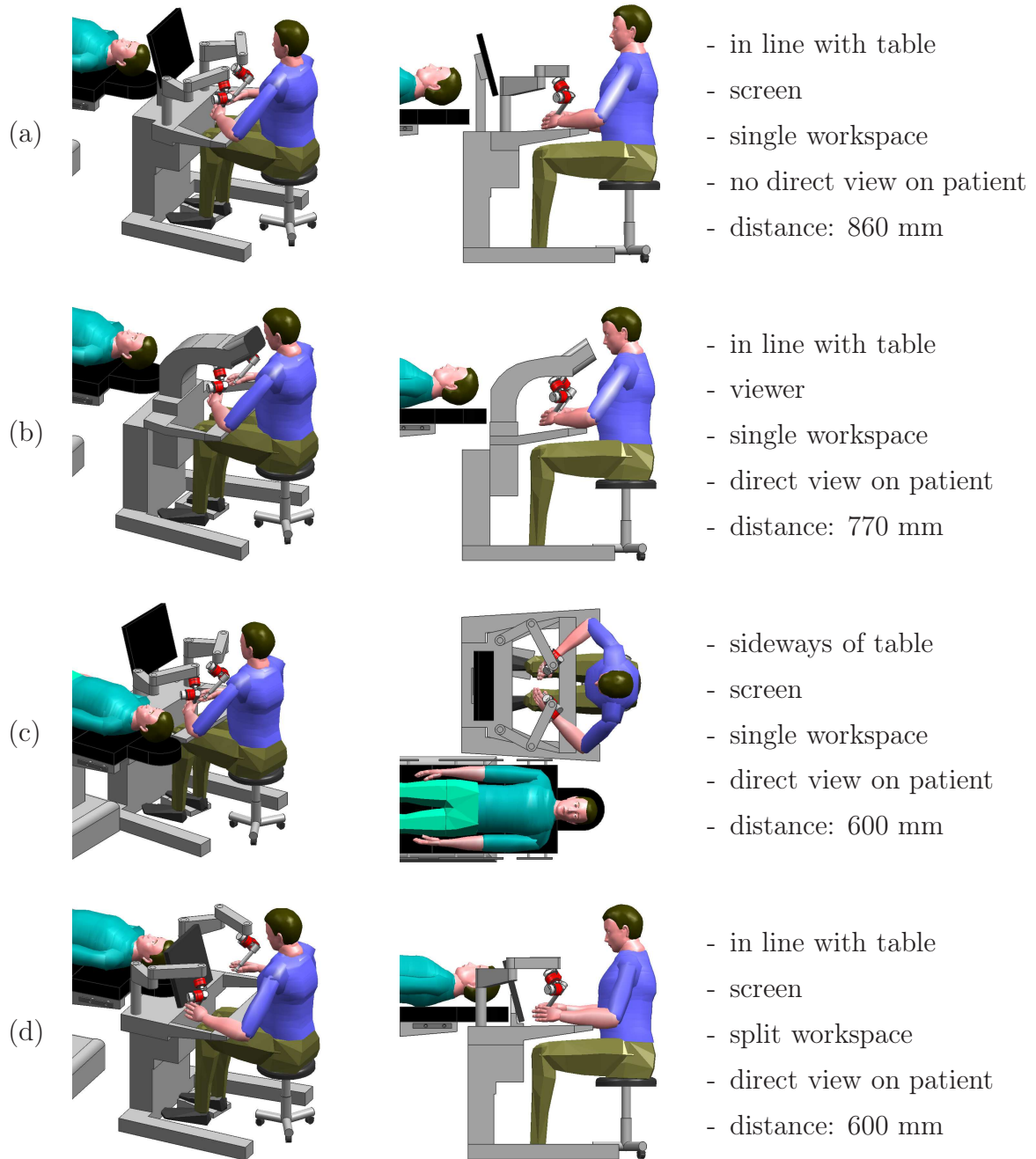
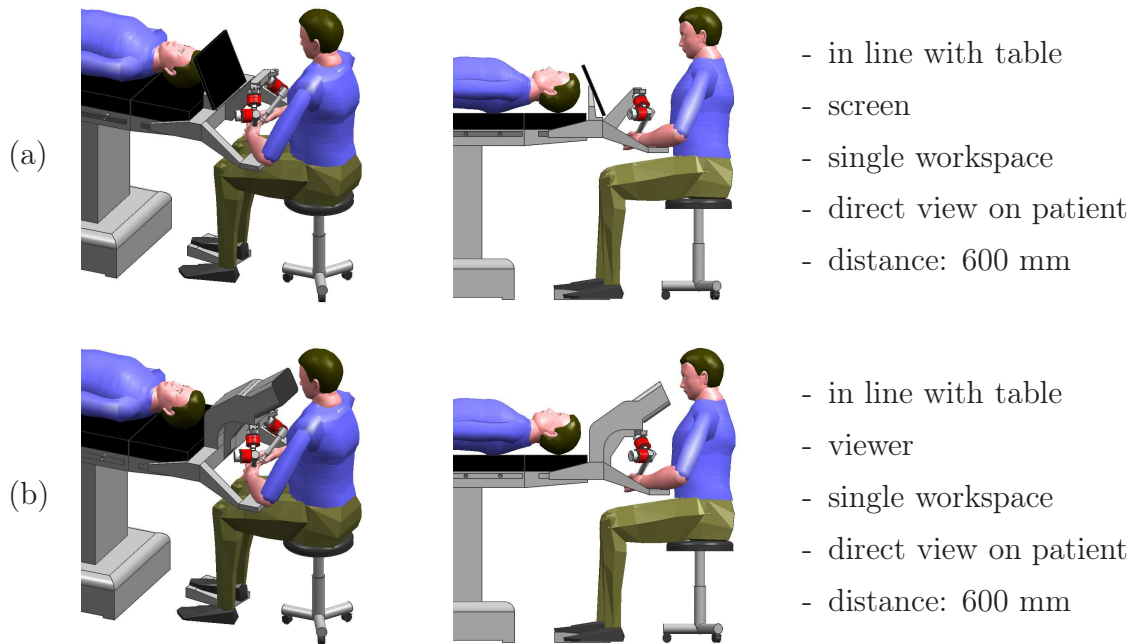


Figure 3.8 / Concept layouts for a freestanding master console.



**Figure 3.9** / Concept layouts for a table mounted master console.

figure 3.9(a), the console in figure 3.9(b) has a binocular viewing device. The screen or viewer, armrest and the two haptic interfaces are placed on one single frame. The frame is mounted to the head support of the operating table.

The layouts in figure 3.9 are appropriate for a male with average body dimensions, see table 3.2. The top of the screen/viewer is  $15^\circ$  below the horizontal sight line of the surgeon. The surgeon sees the patient's head when he looks over the screen/viewer. Like the frame based setups, the image is not collocated with the haptic interfaces. The misalignment is  $15^\circ$ .

The console must be adjustable in height to deal with the variations in body length. This adjustment is done via the operating table. Its height is adjustable between 600-950 mm [52] and is set in this particular case on 880 mm. Fine adjustments of the armrest and screen or binocular viewing device are sufficient to guarantee an ergonomic way of working.

Situations with the stylus nearly horizontal (in nominal position) are left out of consideration, as the human wrist and forearm do not allow to manipulate the stylus freely in all directions for these stylus orientations. As result, the workspace of the coarse adjustment is reduced from  $\varnothing 400$  mm to  $\varnothing 300$  mm. The distance between surgeon and patient is in the order of 600 mm. Both setups do not influence the accessibility of the assistant(s) to the patient.

An additional advantage of a table mounted master console is that the frame can be

used for the slave as well. This is not possible with a freestanding device, unless the position of the slave with instrument manipulators is synchronized with the movements of the head support of the operating table. A combined master-slave system reduces the setup time as the entire device can be placed in one single action. Furthermore, the master and slave electronics can be integrated in the frame. This abandons the need for a separate electronics cabinet and reduces the number of cable connections.

Due to the different advantages, a table mounted device is preferable over a freestanding master console. It can be equipped with a polarized screen or a binocular viewing device for the visual feedback. In first instance, there will be chosen for a screen as a viewer isolates the surgeon in a larger extend from the patient and forces the surgeon to work in a static body posture [38].

## 3.4 Conclusions

The operating room arrangement during manually performed vitreo-retinal eye surgery is almost identical for the ZNA hospital in Middelheim, the AZM in Maastricht and the CZE in Eindhoven. All three operating rooms allow to place a master console in line with or sideways of the headrest of the operating table. The master console must have two haptic interfaces for a bimanual manipulation of the surgical instruments and must provide a 3D visual feedback of the captured microscope and endoscope images.

Five degrees of freedom are sufficient for a stylus based haptic interface. One DoF is for the control of the instrument function and the remaining four for the manipulation of the instrument about the entry point. The rotation point and the orientation of the interface must correspond with those of the instrument for an intuitive way of working. The two interfaces are set in the correct pattern and orientation via two coarse adjustments arms. Together with the visual feedback, it is as if the surgeon grasps the instrument near its tip within the eye. It is also possible to control three or more instruments with only two haptic interfaces. A coarse adjustment arm must have a high stiffness to prevent that the dynamical behavior and the force feedback of the haptic interface is being affected by it. The haptic interfaces must be adjustable within a  $\varnothing$ 300-400 mm large hemisphere.

The two best options for the visual feedback are either a polarized stereoscopic display or a binocular viewing device. A polarized display requires that the surgeon wears passive polarized glasses to filter out the correct images for the left and right eye. This type of display provides full color images and does not restrict the surgeon's head movements to a specific viewing window. Drawback is a reduction in contrast and brightness, elements which require further assessment. A better image quality is obtained with a binocular viewing device, but here head movements are restricted. A sideways movement of more than half the interpupillary distance (30-35 mm) results in crosstalk between the left

and right image and loss of the stereoscopic effect. This means that the surgeon has to work in an almost fixed body posture.

A table mounted master console is chosen as it can be combined with the slave and as it has a more compact design which is easier to place than a freestanding device. Furthermore, it allows the surgeon to have a direct view on and a physical contact with the patient. In first instance, the master will be equipped with a polarized 3D screen, but it is also possible to adapt the design for a binocular viewing device. In both cases, there is no possibility for an exact collocation between the screen image and the haptic interfaces. The misalignment is  $15^\circ$ , only one sixth of the misalignment during manually performed surgery.

The stylus based haptic interface is the most critical part in the master console as it influences the exact design of the coarse adjustment and frame. Furthermore, it must have a high quality of force feedback. Single DoF master-slave systems allow to study the impact of aspects like stiffness, inertia and actuator choice on the haptic feedback in an orderly and fast way.

# Single DoF master-slave setups

---

**Abstract /** The quality of the force feedback of the stylus based haptic interface depends on different design aspects such as stiffness, inertia, actuator choice and the required force levels. Two single DoF master-slave setups are realized to derive the specifications for the interface. One setup is based on a rotation, the other on a translation.

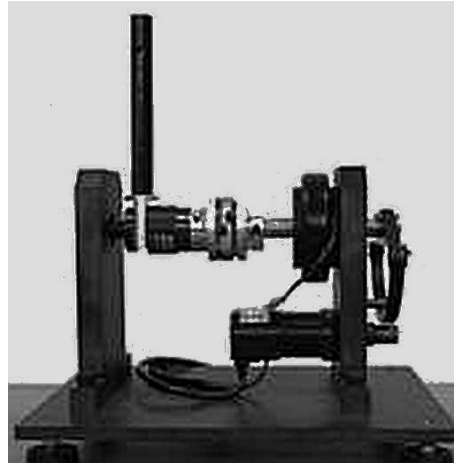
The stylus based haptic interface must have a high quality force feedback. This quality depends on different aspects, like device stiffness, inertia, actuator choice, transmission and the control algorithm. Single DoF master-slave systems allow to study the impact of these aspects on the haptic feedback in an orderly and efficient manner, without the need for a fully operational and expensive multi DoF device. Furthermore, a single DoF device will not suffer from any kinematic or dynamic cross coupling effects and will have better dynamical properties, due to its limited number of joints and links.

There are two distinct classes of haptic devices: impedance controlled devices and admittance controlled devices [51]. In case of impedance control, a movement of the master is detected via for example an encoder on the force feedback motor. The controller uses the position information for a correct presentation of the force and contact stiffness. Admittance control works the other way round. A force sensor at the end effector tip of the master measures the force, the controller takes care of a correct movement of the end effector tip. Combinations of both controller types also exist. These are for example the four channel haptic control algorithms as proposed in [47].

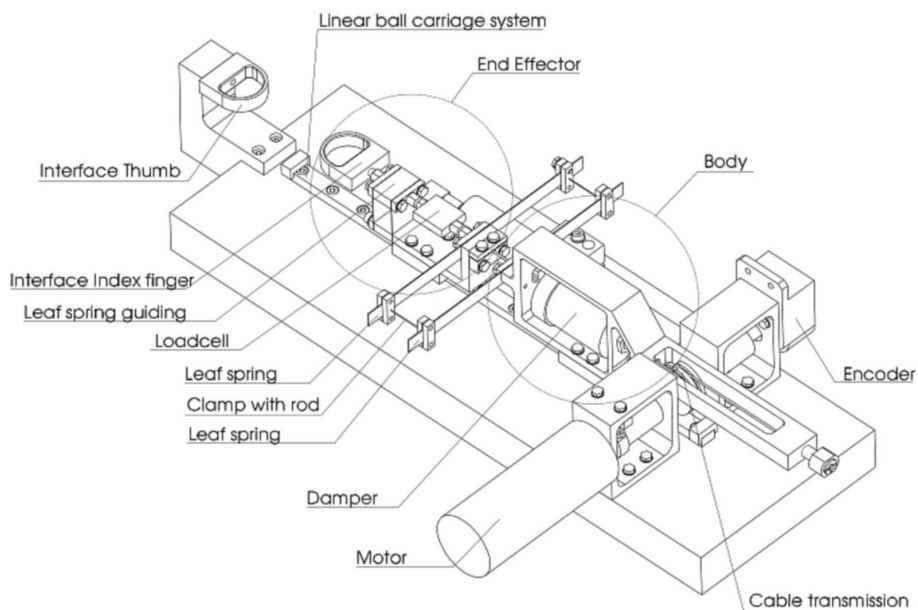
Each category has its own requirements with respect to the mechanical design of the master-slave setup. An admittance controlled device must be equipped with a force or torque sensor and can work with a high gear ratio. On the other hand, an impedance controlled device does not need this sensor, but must be backdriveable.

## 4.1 Existing single DoF master-slave setups

Figure 4.1 gives two examples of experimental setups as realized by An et al. [1] and Fritz et al. [28]. Both systems are backdriveable and equipped with a position sensor and a force or torque sensor.



(a) KAIST rotational setup [1]



(b) TU Delft translational setup [28]

**Figure 4.1** / Experimental 1 DoF setups.

The device in figure 4.1(a) is based on a rotation and has a motion range of  $144^\circ$ . The user grasps the entire handle with his hand. The handle is driven by a motor via a

capstan drive and segment. The transmission ratio is  $i = 1/10$  and the maximum torque is 28 Nm. A torque sensor and a magnetorheological brake are mounted between handle and segment. The torque sensor measures the exerted force on the handle. The setup was created to study the combination of active (like a motor) and passive (like a damper and brake) actuators in haptic devices. The hypothesis is that stability and performance are improved, as a passive actuator can only remove energy from a system. An example of a performance improvement is to simulate a rigid wall which requires a high torque for deceleration. The master is used in combination with simulated environments like a wall and measured force-position profiles.

The setup in figure 4.1(b) is designed in a hard master, soft slave framework. The master reproduces the characteristics of the remote environment and the slave represents the operator's hand. The system is based on a translational movement with a stroke of 50 mm to grasp small objects between index finger and thumb. Two linear ball guides are mounted on the frame to guide the body and end effector part. The motor drives the body via a cable transmission (maximum force: 50 N). Leaf springs and a damper connect the end effector with the body. The damping ratio and stiffness are both adjustable. In the master device, the damper and leaf springs are replaced by a rod. A load cell in the end effector measures the force on the interface with a resolution of 0.05 N. A parallelogram guides this interface. An LVDT measures the position of the end effector. An encoder measures the position of the body via the cable drive. Both systems have a resolution of 30  $\mu\text{m}$ . The friction force is between 0.35 and 0.6 N and the moving mass is 0.4 kg [17].

## 4.2 Design specifications and requirements

A single DoF setup with a stylus like end effector, grasped between the thumb and index finger and operated from wrist and forearm movements has the most similarities with the intended layout for the 5 DoF haptic interface. This layout deviates from the two setups as described above as the first one is based on whole-hand grasping and the second one on a squeezing motion between thumb and index finger. This means that a new device has to be designed and built. The same design will be used for the master and slave device. This design can be based on a rotational or translational movement of the end effector.

In case of a translation, the user feels the inertia of the end effector and the friction of the linear (ball) guides directly. In a rotational setup, the friction force has its origin near the rotation axis and scales downwards with an increasing distance between rotation axis and end effector tip. The apparent moving mass at the tip of the end effector is less, as the contribution of the mass of the different components to the total inertia decreases quadratically with a decreasing distance towards the axis of rotation. Furthermore, it



is to be expected that the friction of the translational setup will increase on long term use, as the unshielded ball races are sensitive to contamination. A work around is to apply air bearings, but this makes the setup more expensive. Therefore, it is preferable to build a device with a rotational layout. Furthermore, three of the four main DoFs during vitreo-retinal eye surgery are rotations as well. A motion range of  $\pm 45^\circ$  equals the  $\varphi$  and  $\psi$  rotation of an instrument during surgery.

Inertia and friction are just two of the design specifications for haptic devices. The following is a listing of the most important specifications as found in [26, 36, 60, 85]. The specifications are valid in combination with impedance control.

- low inertia/moving mass

A high inertia makes it more difficult for the operator to perform a specific task and can result in fatigue. System performance decreases as function of inertia, due to lower eigenfrequencies. This makes it, for example, more difficult to represent the high frequency content of the force feedback. As result of this, the force feedback will be less realistic.

- high stiffness

The device stiffness must be higher than the simulated contact stiffness. Furthermore, it results in higher eigenfrequencies and a higher control bandwidth. Most ideal, but most likely not feasible, is a bandwidth that equals the 1 kHz perceptual bandwidth for vibrotactile stimuli.

- low friction

Friction results in a lower force resolution as it directly interferes with the feedback of the forces as measured at the slave. A lower friction allows a more precise manipulation of the instrument. The friction level should be  $\leq 1\%$  of the continuous force.

- backdrivability

A device without force measurement at the end effector must be backdriveable. This means that the drive train must employ relatively low gear ratios.

- zero backlash

Backlash can result in control instabilities. Furthermore, it has a negative effect on performance as the slave does not instantaneously follow when the end effector is moved in the opposite direction. Direct drive or a preloaded transmission avoids backlash.

- weight compensation

A statically balanced system avoids operator fatigue and reduces the required motor power. Balancing can be done with counterweights, but the additional

mass results in a lower eigenfrequency. An alternative is to use spring based compensation.

- uniform workspace

With an optimal system design, the actuator and sensor capabilities will be consistent throughout the workspace. This minimizes the requirements for the actuators and encoders/sensors. Singularities must be avoided as they create directions in the workspace in which the end effector cannot be moved by the operator. This reduces the manipulability of the system and the dexterity of the user.

- degrees of freedom

Six DoFs is ideal for a general purpose hand controller, but a large number of DoFs has a negative effect on the moving mass, stiffness and friction.

- output force/torque

An operator can generate large static forces and torques. These must be matched by the haptic device to simulate stiff and hard contacts. The output force and torque influences the peak acceleration.

Design specifications such as a high stiffness, low friction and zero backlash are together with a statically determined system design [75] of importance for a reproducible and predictable system behavior.

The requirements for an admittance controlled device are less strict as friction and inertia can be compensated via the force/torque measurement and the control loop. Nevertheless, a good mechanical design reduces the necessary control effort. This means that the design of the 1 DoF setup can be based on the requirements as stated above, as long as it is equipped with a torque or force sensor. The combination of a position measurement system and a force/torque measurement enables the implementation of four channel haptic control algorithms.

The maximum force that can be applied with the index finger is 50 N [13]. Experiments showed that in the case of grasping, discomfort is encountered after 10 minutes at a level of 25% (=12.5 N) of the maximum force. These forces are much higher than the maximum and continuous forces of the commercially available haptic devices in table 2.3. Therefore, the forces are reduced to respectively 30 N and 10 N.

To take full advantage of human haptic capabilities, a resolution of 0.01 N is recommended. Hand motions must be detected with a resolution of at least 50  $\mu\text{m}$ , as this is the accuracy a surgeon can position his hand with [74]. Passive elements, like dampers, are left out as they interfere with the force feedback. With a modular design of the master and slave, it is possible to add them later if it turns out to be necessary for stability reasons.

### 4.3 Single DoF rotational setup

The entire setup is visible in figure 4.2. The three main components are a slave to interact with the environment (for example a spring), a master operated by a user and a cabinet with current amplifiers and a programmable logic controller (PLC) for safety. The master and slave are identical. To control the setup a RTAI Linux environment with Matlab Simulink<sup>®</sup> in combination with a TUE DACS [91] or a dSPACE<sup>®</sup> [23] acquisition system is used.

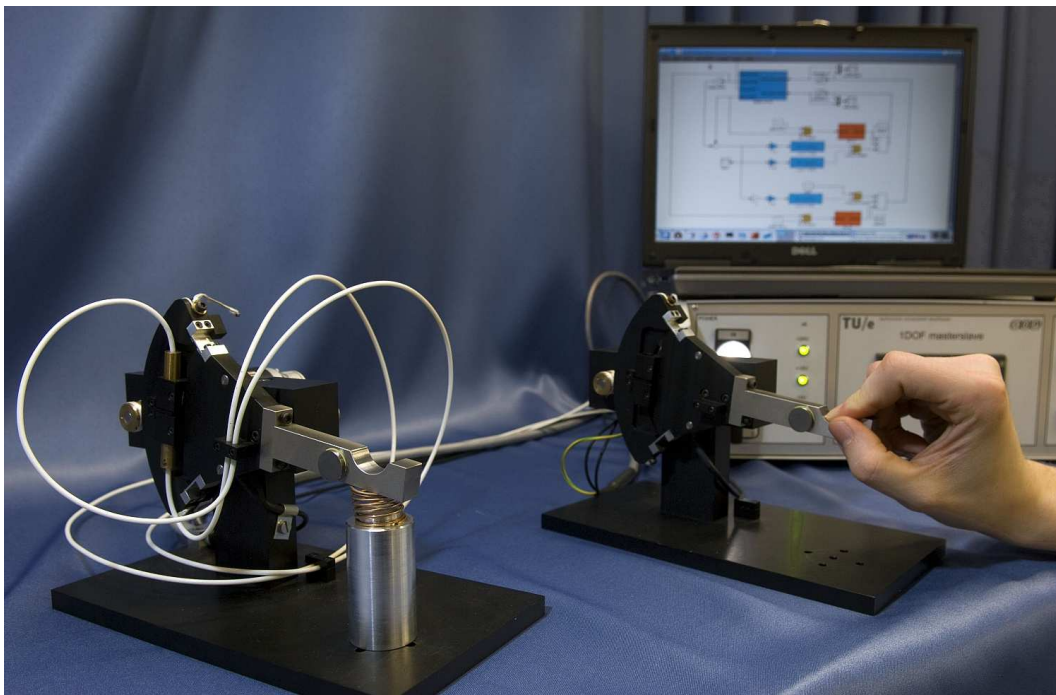
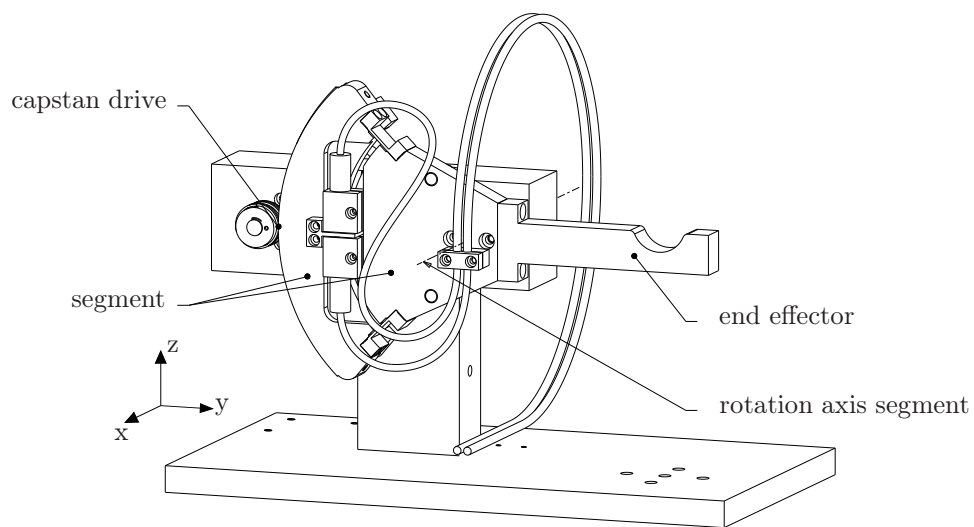


**Figure 4.2** / Single DoF master-slave setup. Visible are (from left to right): slave, master and the electronics cabinet with on top the RTAI Linux environment and control algorithm in Matlab Simulink<sup>®</sup>.

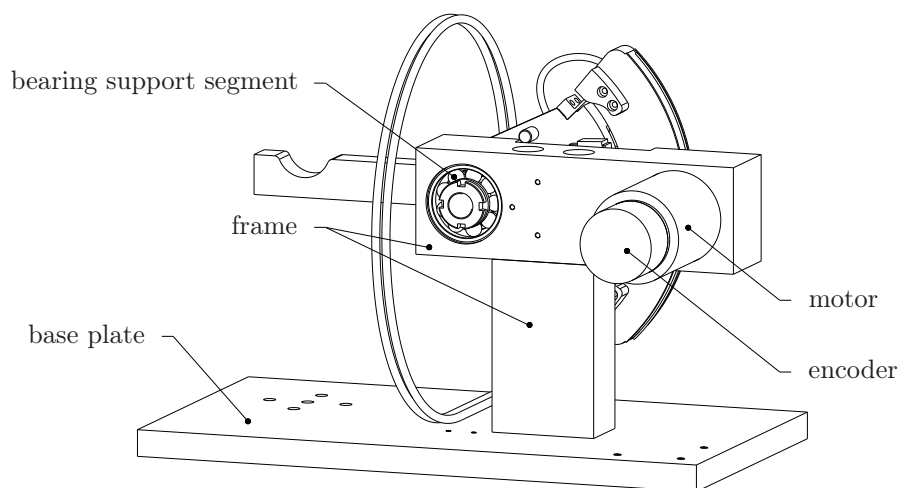
The system is backdriveable and backlash free. A torque sensor is integrated to measure the force on the end effector. This combination makes the setup suitable for impedance, admittance and four channel control algorithms.

#### 4.3.1 Mechanical design

Figure 4.3 gives a schematic overview of the 1 DoF setup. Force feedback is implemented by the use of a DC electric motor which drives the segment via a capstan drive. Two angular contact bearings support the segment. The user or environment interacts with the end effector. An incremental encoder at the rear of the motor measures the rotation



(a) frontside



(b) backside

**Figure 4.3** / Overview of the 1 DoF setup. The frame supports the motor/encoder and segment with end effector. The motor drives the segment via a capstan drive.

of the motor shaft. With the end effector, the segment is statically balanced. It is possible to interchange the end effector without disassembling the remainder of the setup.

## Frame

The frame consists of a base plate and a T-shaped top part consisting of two aluminum blocks. The motor and the angular contact bearings are integrated in the upper frame block. This layout gives maximum freedom around the end effector. The distance between the rotation axis of the segment and base plate is 85 mm. In this way the operator's wrist can rest on the base plate during manipulation of the end effector. This leads to a very short force loop.

The environment is created by placing objects (like a spring or a rigid post) under the end effector of the slave. The base plate has five holes to mount such objects.

## DC motor and encoder

Commutation is required for a DC motor to operate. During commutation, the motor current switches from one coil to another. This can result in a torque ripple and distortion of good haptic feedback. In a brushed DC motor, commutation is performed by the brushes in combination with the collector segments of the rotor. In a brushless DC motor, the coils are stationary and commutation is performed by the amplifier in a block or sinusoidal way. For maximum torque, the angle between the magnetic field of the permanent magnets and coil must be  $90^\circ$ . Only sinusoidal commutation, which has in fact an unlimited number of commutation points, can achieve this. For block and brushed commutation, the number of commutation points is limited. This results in a torque variation of respectively 13% and  $\approx 1\%$ . A ripple is noticeable when 7% of the reference force is exceeded [66], leaving two options: a brushless motor with sinusoidal commutation or a brushed motor. The last one is chosen as it requires only a simple current amplifier and reduces the number of wires due to the absence of Hall sensors.

Simulating touching a rigid wall requires a high deceleration. The maximum acceleration and deceleration is achieved with an inertia match between motor and segment with end effector.

$$\frac{T_{motor}}{i} = \frac{J_{motor}}{i^2} \ddot{\varphi}_{seg} + J_{seg} \ddot{\varphi}_{seg} \quad (4.1)$$

$$\Rightarrow \ddot{\varphi}_{seg} = \frac{T_{motor} i}{J_{motor} + J_{seg} i^2} \quad (4.2)$$

To find a maximum acceleration, the derivative to  $i$  must be equal to 0 (see also figure 4.4):

$$\frac{d\ddot{\varphi}_{seg}}{di} = \frac{T_{motor}(J_{motor} + J_{seg} i^2) - 2J_{seg}T_{motor} i^2}{(J_{motor} + J_{seg} i^2)^2} = 0 \quad (4.3)$$

$$\Rightarrow J_{motor} = J_{seg} i^2 \quad (4.4)$$

The inertia of the segment as visible in figure 4.3(a) is  $7.1 \cdot 10^{-4} \text{ kgm}^2$ . The continuous force is set to  $F_{cont} = 10 \text{ N}$ . Table 4.1 gives an overview of the different motor options. This table is limited to the Maxon RE product range [55]. The column  $i_{nom}$  gives the required transmission ratio to achieve the continuous force of 10 N. Column  $i_{im}$  gives the ratio for an inertia match.  $F_{cont}$  is the achieved continuous force based on the inertia match ratio.

**Table 4.1** / Maxon RE series

Motor	$P$	$i_{nom}$	$i_{im}$	$F_{cont}$
RE 30	60 W	1/8.8	1/14.5	16.4 N
RE 35	90 W	1/8	1/10.1	12.5 N
RE 40	150 W	1/4.4	1/7.1	16.1 N

Based on these figures the RE 35 is chosen in combination with a ratio of  $i = 1/10$ , this to comply with the inertia match and to have a continuous force of  $>10 \text{ N}$ . The maximum force is limited to  $30 \text{ N}$  ( $T_{motor} = 0.23 \text{ Nm}$ ). According to the graph in figure 4.4 the maximum acceleration is  $\ddot{\varphi}_{seg,max} \approx 1.6 \cdot 10^3 \text{ rad/s}^2$ . Also visible is the effect on the maximum acceleration when a different ratio between motor and segment is chosen.

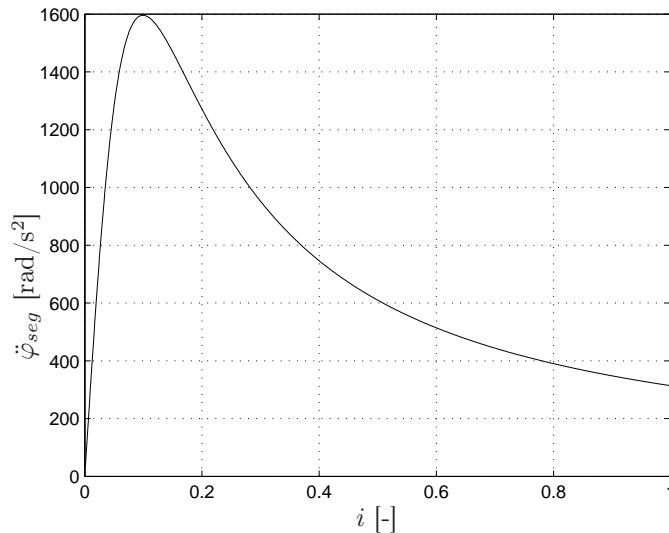


**Figure 4.4** / Maximum acceleration of the segment as function of the ratio  $i$ .

An advantage of the RE 35 is that it is available in combination with a high resolution optical encoder (30,000 counts/rev). This gives a resolution of  $1.6 \mu\text{m}$  at the tip of the

end effector. An alternative is to measure the rotation of the segment directly, but this requires a more expensive, precision angular measurement system.

### Capstan drive

A capstan drive gives a smooth operation compared to a gearwheel transmission. The transmission ratio is set by the diameter of the pulley and segment. A small pulley and segment are desirable to minimize inertia. The radius of the segment is set to 75 mm to have enough room for the torque sensor. Consequently, the pulley diameter is 15 mm. The segment and pulley allows a cable diameter up to 1 mm.

Steel cable is often applied in the capstan drives of commercially available masters (for example the systems from Sensable Technologies, Inc. and Force Dimension). A suitable zinc coated steel cable is a 0.9 mm cable consisting of 49 individual wires with a thickness of 0.1 mm. An alternative is to apply a Dyneema<sup>®</sup> cord. This cord is made up of extremely long polyethylene molecular chain filaments, which all align in the direction of the cord. Each chain is bonded to the others by van der Waals forces. The filaments in this cord are 0.01 mm thick. Compared to steel, Dyneema<sup>®</sup> can be used on a very small pulley, see table 4.2. Also the friction between the individual wires of the cable undergoing bending deformation is lower, resulting in a lower amount of hysteresis for the setup.

**Table 4.2 /** Steel wire compared to Dyneema<sup>®</sup> wire

	steel wire	Dyneema <sup>®</sup> wire
modulus of elasticity	207 GPa	110 GPa
tensile strength	1.8 GPa	3.5 GPa
diameter filaments	0.1 mm	0.01 mm
minimal bending radius	5.8 mm	0.16 mm
load capacity left	23%	98%

A 1 mm thick Dyneema<sup>®</sup> cord is applied. This cord is very supple and has a load capacity of more than 2 kN. With a cross section of  $A = 0.8 \text{ mm}^2$  and a length of  $l = 0.16 \text{ m}$ , the stiffness becomes:

$$c_{dyn} = \frac{EA}{l} = \frac{0.93 \cdot 110 \cdot 10^9 \cdot 0.8 \cdot 10^{-6}}{0.16} = 5.1 \cdot 10^5 \text{ N/m}$$

The factor 0.93 in this formula is a correction factor for the axial stiffness, as the individual strands are placed under an angle of approximately 15°. The calculated stiffness equals a torsional stiffness of  $k_{dyn} = 2.9 \cdot 10^3 \text{ Nm/rad}$  and is sufficiently large, in spite of the lower modulus of elasticity.

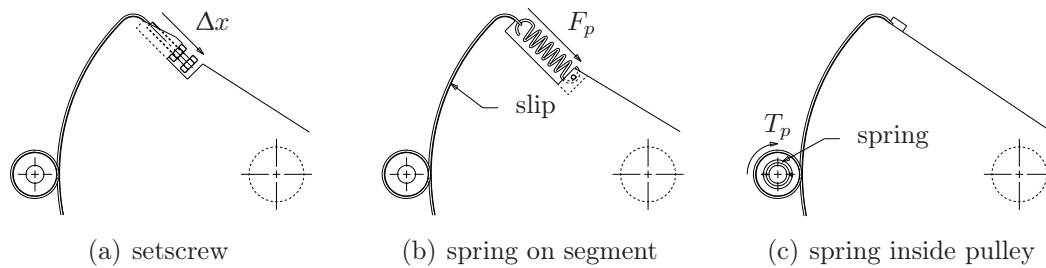


**Figure 4.5** / Preload of the capstan drive

To prevent backlash there must always be a tensile preload force on the cable. In a Phantom<sup>®</sup> (Sensable Technologies, Inc.) for example the cable is preloaded by adjusting the cable length via a setscrew (see figure 4.5(a)). In this case, the force is the elongation times the stiffness of the cable. Due to the high cable stiffness it is very difficult to set the correct force level: either backlash or a higher friction level due to an increased bearing load will be the result.

The force level is also affected over the stroke by eccentricity. If a tolerance is assumed of 10  $\mu\text{m}$  between the different parts (shaft, inner segment part, elastic elements and outer segment part), then the eccentricity of the segment is in the order of 30  $\mu\text{m}$ . The accompanying elongation or shortening of the wire is  $\approx 3.5 \mu\text{m}$  by which the force varies with  $>30 \text{ N}$  when no slip is assumed between cable and segment. Drawback of this variation is that the setup will move to a position with minimal elastic energy.

A preload spring as drawn in figure 4.5(b) deals with these disadvantages. In this case, the force variation is based on the stiffness of the spring instead of the much higher stiffness of the cable. In this layout, elongation and shortening is accompanied by slip between cable and segment. An alternative is to implement the preload spring inside the pulley (figure 4.5(c)). Hereto, the pulley is split in two parts. One pulley with cable is fixed to the motor shaft. The other pulley with cable is preloaded via the spring.

Figure 4.6 gives an exploded view of the capstan drive as implemented in the 1 DoF setup. The pulley at the front is fixed to the motor shaft. The second half pulley is free to rotate around this shaft. A spacer on the motor shaft and the pulley at the front prevents a movement in axial direction. Around both pulleys a wire is wrapped and connected to the segment. One wire goes upwards and the other wire downwards. A chamber inside each half pulley provides the required space for the preload spring. The spring legs are bent in axial direction and each held in an axial hole. The recommended mandrel size of the spring is 6 mm, which is identical to the diameter of the motor shaft.

As fixation of the outer pulley gives the most compact layout and lowest number of individual parts, this option is chosen above fixation of the inner pulley. The drawback is a small decrease in the torsional stiffness of the motor shaft: from approximately



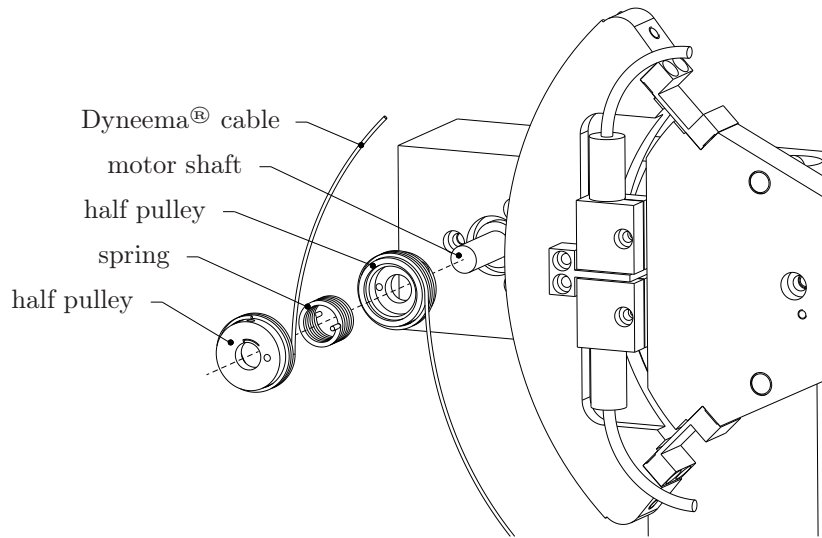


**Figure 4.6** / Exploded view of the internally preloaded capstan drive. Both cables are fixated to the segment.

$k_{ms} = 1.6 \cdot 10^2 \text{ Nm/rad}$  to  $k_{ms} = 1.5 \cdot 10^2 \text{ Nm/rad}$ . This is still five times stiffer than the cable itself when the transmission ratio is taken into account.

The preload force depends on a relative rotation between both pulleys and is set during assembly. A rotation of  $90^\circ$  results in a force of 30 N, which is identical to the maximum force at the tip of the end effector. For the  $3.5 \mu\text{m}$  elongation, the force varies with  $<20 \text{ mN}$ .

### Segment with torque sensor

The exerted force can be measured with a load cell at the tip of the end effector or via a torque sensor. A load cell in the end effector makes the replacement of this part more complicated. There can also be a thermal issue when the user grasps the end effector directly by hand. Therefore, a torque sensor is implemented.

One option is to use a commercially available sensor like a Futek TFF400 series torque sensor [29]. The alternative is to implement the torque measurement inside the segment. The advantages of this alternative are a more compact design and a lower inertia, due to the absence of an additional sensor housing and mounting flanges. The construction and main components of the torque measurement system implemented are visible in figure 4.7.

The segment is split in two concentric parts which are connected by two short and thick leaf springs. The torque is measured indirectly via the relative rotation between the inner and outer segment part (figure 4.8) according to:  $\varphi = \frac{T}{k}$ , with  $T$  the torque and  $k$  the torsional stiffness of the leaf springs. The radial orientation of the springs results

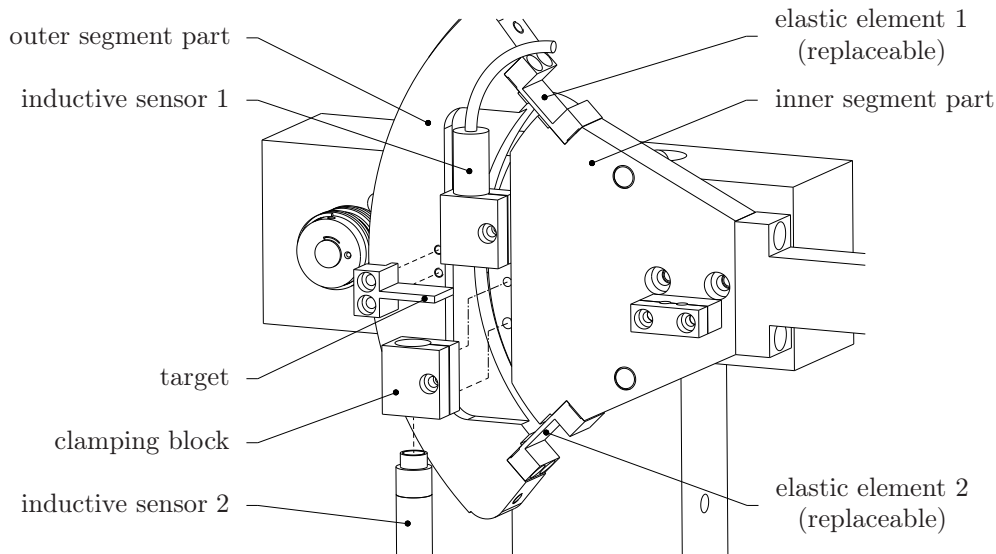


**Figure 4.7** / Exploded view of the torque sensor to measure the exerted force at the tip of the end effector. The elastic elements are replaceable.

in a pole at the rotation axis of the inner segment part. This means that the two parts stay basically concentric.

The actual measurement is done by two inductive sensors in a differential setup with respect to a target. The target, an aluminum strip, is mounted on the outer segment part. The opposing sensors are each fixated via a clamping block on the inner part. The bore of the clamping block protects the tip of the sensor and allows an axial movement to set the offset distance. The measuring range of the inductive sensors is  $\pm 50 \mu\text{m}$ . The typical resolution is 1 part in 10,000. The dual sensor differential setup gives a two times higher sensitivity and compensates for variations in the room temperature. Otherwise, there will be a measuring error of  $0.13 \text{ N/K}$  caused by the 8 mm between target and clamping point in combination with the linear expansion coefficient of aluminum ( $\alpha_{al} = 23 \cdot 10^{-6}/\text{K}$ ).

The aluminum radial leaf springs of the torque sensor are designed on a theoretical stiffness of  $c_{ts} = 2.7 \cdot 10^5 \text{ N/m}$ , which equals a torsional stiffness of  $k_{ts} = 3.5 \cdot 10^3 \text{ Nm/rad}$ . In practice, it is possible that the stiffness will be lower due to the mounting blocks and the transition to the segment parts. According to a FEA analysis of the entire segment, the torsional stiffness of the torque sensor will not be below  $k_{ts} = 2.7 \cdot 10^3 \text{ Nm/rad}$ . Compared to a Futek TFF400 series torque sensor, this sensor has a 12 times higher torsional stiffness.

For the maximum torque of 2.25 Nm (30 N at the tip) the displacement of the target is  $42 \mu\text{m}$  with respect to the inductive sensors. The accompanying stress in the leaf springs is 44 MPa. In the case of a collision, for example due to an instable control algorithm, this stress level can be much higher. The elastic elements are made from

Al 7075 (yield strength of  $>400$  MPa) to prevent plastic deformation. The elements can be replaced if they get damaged in spite of the precautions.

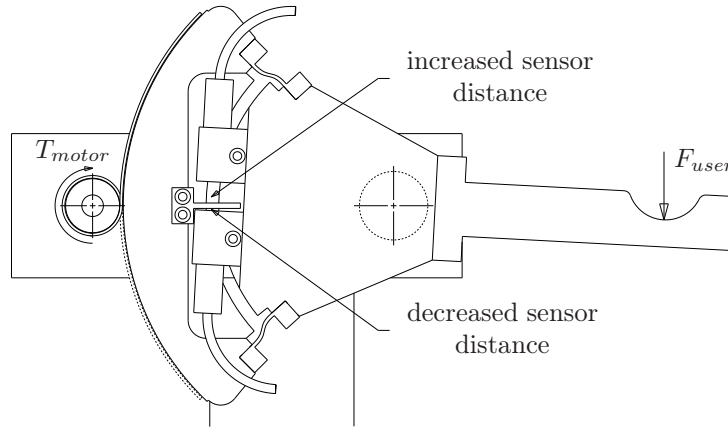


**Figure 4.8** / Working principle of the torque sensor. Visible is the relative rotation between the two segment parts as result of a force  $F_{user}$  exerted by the user and a motor torque  $T_{motor}$ . The rotation is measured by two position sensors.

The typical resolution of the position measurement results in a resolution of 7 mN at the tip of the end effector. The measurement is influenced by the friction of the angular contact bearings, the sensor cables and the non linearity of the sensors. Further, there is a cosine error due to rotation of the target with respect to the sensor (0.8 mrad). According to the inductive sensor application manual [41] this error is neglectable for a nonparallelism up to 35 mrad.

The distance pieces for the segment bearings are fabricated in such way that there is only a light preload of  $\approx 10$  N. This gives a static friction torque of  $\approx 0.2$  Nmm (3 mN at the tip). This friction torque will increase with an increasing load on the end effector to a maximum of  $\approx 1$  Nmm (13 mN at the tip).

A second disturbance force is caused by the damping in and the stiffness of the two sensor cables. These coax cables are the connection between the coils in the sensor and the signal conditioning electronics. The minimum bending radius is approximately 30 mm. Damping is minimized by a minimal bending of the cable while the stiffness effect depends on the amount of elastic energy.

Mounting the cable in a S shape is preferable from this point of view. The segment guides one part of the cable, the other part is guided by a cable guide on the frame. During a rotation, the cable moves from segment to frame and vice versa. The cable length and elastic energy inside the S remains constant. The drawback of this layout is that the large bending radius restricts the freedom around the end effector. Therefore, the cable is lead away in a curl (radius  $r_{cable} \approx 85$  mm) perpendicular to the segment. The cable is fixated by a clamp on the base plate and one on the segment. This last

clamp is placed close to the rotation axis to minimize deformation, while the cable has only to move along with the rotation instead of a rotation and translation.

### End stops and end switches

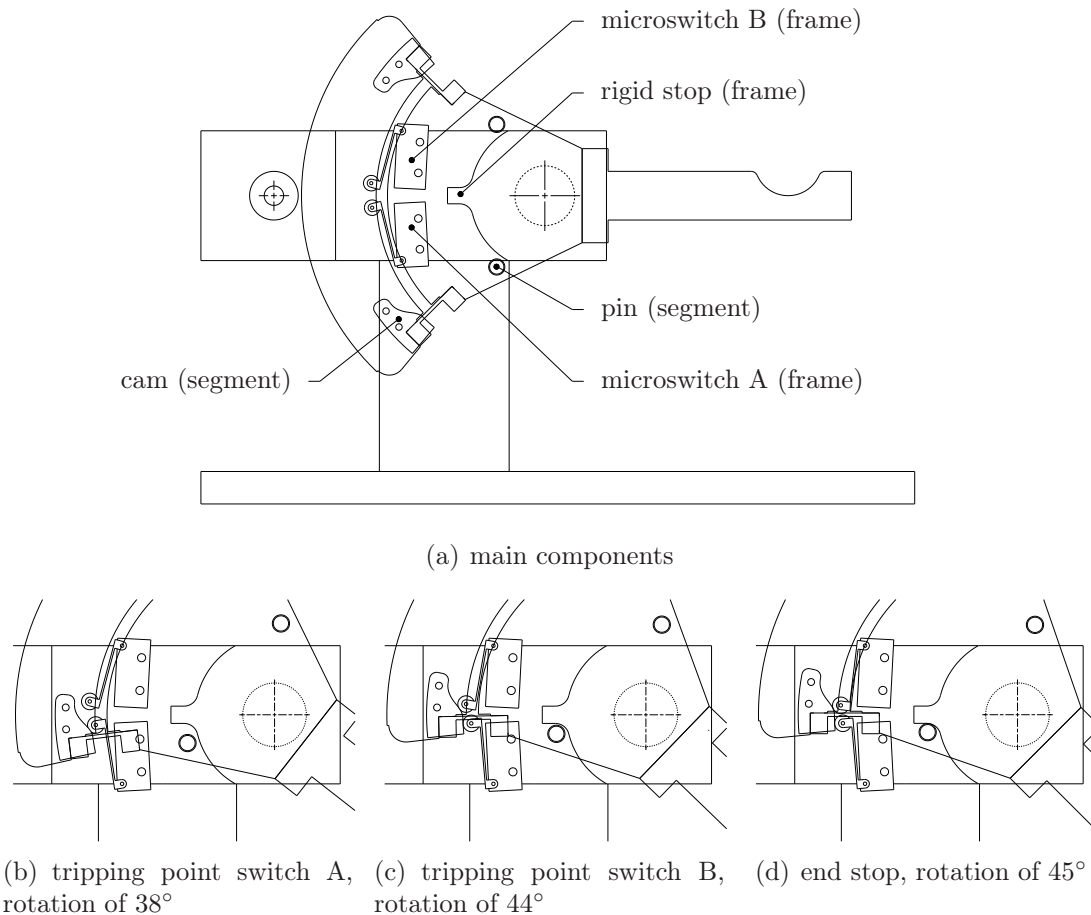


**Figure 4.9 /** Working principle of the end switches and end stops. The contour of the segment and end effector are indicated by a thin line.

Figure 4.9 gives an overview of the integration and the working principle of the end stops and end switches. Two pins on the segment and a rigid stop on the frame limits the rotation of the segment to  $\pm 45^\circ$ . The two microswitches are operated via a cam curve. Two states are detectable: a near end and an end of stroke. The first state is used for initialization, the second as a safety measure to disable the setup. The switches are placed on the frame to prevent additional wires between the moving segment and stationary frame. During operation in a range up to  $\pm 35^\circ$  there is no contact between cams and switches to minimize friction. Tripping points are set on respectively  $38^\circ$  and

44° via the adjustable cams. The margin of 1° guarantees a correct operation of the switch. By monitoring the two signals it is possible to detect the direction of rotation. The actuation in radial direction and the cam geometry prevent that the microswitches can act as an end stop.

### 4.3.2 Electronics and safety

The electronics to operate the setup are integrated in one cabinet, which can be connected via an acquisition system to a PC. Besides the amplifiers and power supplies, a programmable logic controller (PLC) and an emergency stop button are integrated for user's safety and to protect the setup itself.

Three safety measures are programmed inside the PLC, which all result in disabling of the amplifiers. First of all, the master or slave is disabled when the end of the working range is detected via the two microswitches. Secondly, there is a check for a watchdog signal. Absence of this signal from the acquisition system can be the result of a system crash, which means an incorrect input signal to the amplifiers. In the third place, there is a check of the exerted force by monitoring the output voltages of the inductive sensors. An LCD display shows the status of the PLC. A fail safe mode prohibits enabling of the system when the inductive sensors or endswitches are not connected with the electronics cabinet.

Besides the safety measures at hardware level, different safety measurements are implemented in the control algorithms like virtual end stops, limitation of the motor current and the generation of the watchdog signal.

### 4.3.3 Dynamic model and experimental results

Four relevant inertias can be distinguished in the setup. These inertias are:  $J_{m+e} = 7 \cdot 10^{-6} \text{ kgm}^2$  for the motor and encoder combination,  $J_{pulley} = 4.6 \cdot 10^{-7} \text{ kgm}^2$  for the two half pulleys,  $J_{os} = 2.7 \cdot 10^{-4} \text{ kgm}^2$  for the outer segment part and  $J_{is+ee} = 4.4 \cdot 10^{-4} \text{ kgm}^2$  for the inner segment part with end effector. The inertia of all components together is  $J_{tot} = 1.4 \cdot 10^{-3} \text{ kgm}^2$ , equal to an apparent mass of  $m = 0.25 \text{ kg}$  at the tip of the end effector. This value can be reduced to  $0.21 \text{ kg}$  ( $1.2 \cdot 10^{-3} \text{ kgm}^2$ ) by using an aluminum end effector, although it would result in a statically unbalanced system and is therefore not done.

The relevant torsional stiffnesses are  $k_{ms} = 1.5 \cdot 10^2 \text{ Nm/rad}$  for the motor shaft,  $k_{dyn} = 2.9 \cdot 10^3 \text{ Nm/rad}$  for the Dyneema<sup>®</sup> wire and  $k_{ts} = 3.5 \cdot 10^3 \text{ Nm/rad}$  for the torque sensor. Furthermore, there is a deflection of the motor shaft under load. The bending stiffness is  $c_{ms,b} = 1.4 \cdot 10^6 \text{ N/m}$ . This equals a torsional stiffness of  $k_{ms,b} = 7.9 \cdot 10^3 \text{ Nm/rad}$ . The deflection of the main shaft and the bearing stiffness are left out of consideration

as these stiffnesses are an order higher.

Figure 4.10 represents a simplified dynamic model of the setup. The bending stiffness of the motor shaft is placed in series with the stiffness of the Dyneema<sup>®</sup> wire. The following set of equations describes this model:

$$\frac{J_{m+e}}{i} \cdot \ddot{\varphi}_{m+e} = \frac{U}{i} - \frac{k_{ms}}{i} (\varphi_{m+e} - \varphi_{pulley}) \quad (4.5)$$

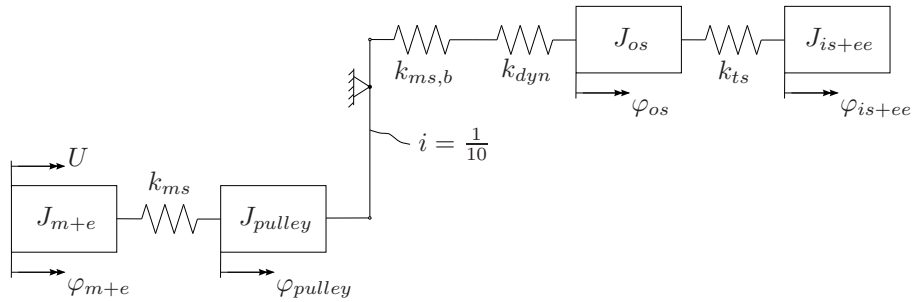
$$\frac{J_{pulley}}{i} \cdot \ddot{\varphi}_{pulley} = \frac{k_{ms}}{i} (\varphi_{m+e} - \varphi_{pulley}) - k_{capstan} (i \cdot \varphi_{pulley} - \varphi_{os}) \quad (4.6)$$

$$J_{os} \cdot \ddot{\varphi}_{os} = k_{capstan} (i \cdot \varphi_{pulley} - \varphi_{os}) - k_{ts} (\varphi_{os} - \varphi_{is+ee}) \quad (4.7)$$

$$J_{is+ee} \cdot \ddot{\varphi}_{is+ee} = k_{ts} (\varphi_{os} - \varphi_{is+ee}) \quad (4.8)$$

with:

$$k_{capstan} = \left( \frac{1}{k_{ms,b}} + \frac{1}{k_{dyn}} \right)^{-1}$$



$$\begin{aligned} J_{m+e} &= 7 \cdot 10^{-6} \text{ kgm}^2 & k_{ms} &= 1.5 \cdot 10^2 \text{ Nm/rad} \\ J_{pulley} &= 4.6 \cdot 10^{-7} \text{ kgm}^2 & k_{ms,b} &= 7.9 \cdot 10^3 \text{ Nm/rad} \\ J_{os} &= 2.7 \cdot 10^{-4} \text{ kgm}^2 & k_{dyn} &= 2.9 \cdot 10^3 \text{ Nm/rad} \\ J_{is+ee} &= 4.4 \cdot 10^{-4} \text{ kgm}^2 & k_{ts} &= 3.5 \cdot 10^3 \text{ Nm/rad} \end{aligned}$$

**Figure 4.10** / Dynamic model of the 1 DoF setup. The input of the actuator and the rotation of the end effector are indicated by respectively  $U$  and  $\varphi$ . The capstan drive has a ratio of  $i = 1/10$ .

Equations (4.5-4.8) are used to draw the Bode plot in figure 4.11. The figure includes the frequency response function (FRF) from motor to encoder and the FRF from motor to end effector for a frequency up to 2 kHz. Damping is left out of consideration. Eigenfrequencies are visible at 320 Hz and 810 Hz. The third eigenfrequency at 3.2 kHz is not drawn.

The FRF from motor to encoder is also measured<sup>1</sup> to verify the dynamical model, see

<sup>1</sup>The frequency response measurements are performed by J. Scholtes [78, 79].

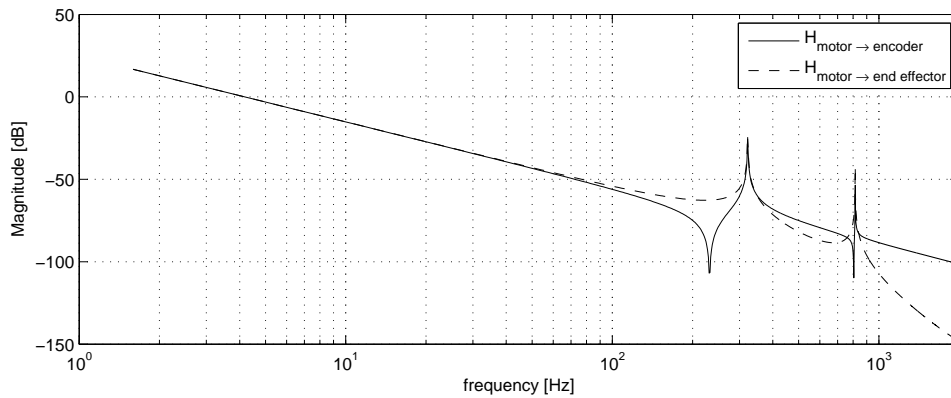


**Figure 4.11** / Frequency response of the dynamic model of the 1 DoF rotational setup for a frequency up to 2 kHz. Eigenfrequencies are visible at 320 Hz and 810 Hz.

figure 4.12. Eigenfrequencies are visible around 310 Hz and 820 Hz. The behavior is typically a result of the collocated sensor-actuator location. The small peak at 150 Hz has to do with the fact that the Bode plot is a combination of two individual measurements, one from 1-150 Hz and one from 150-2000 Hz.

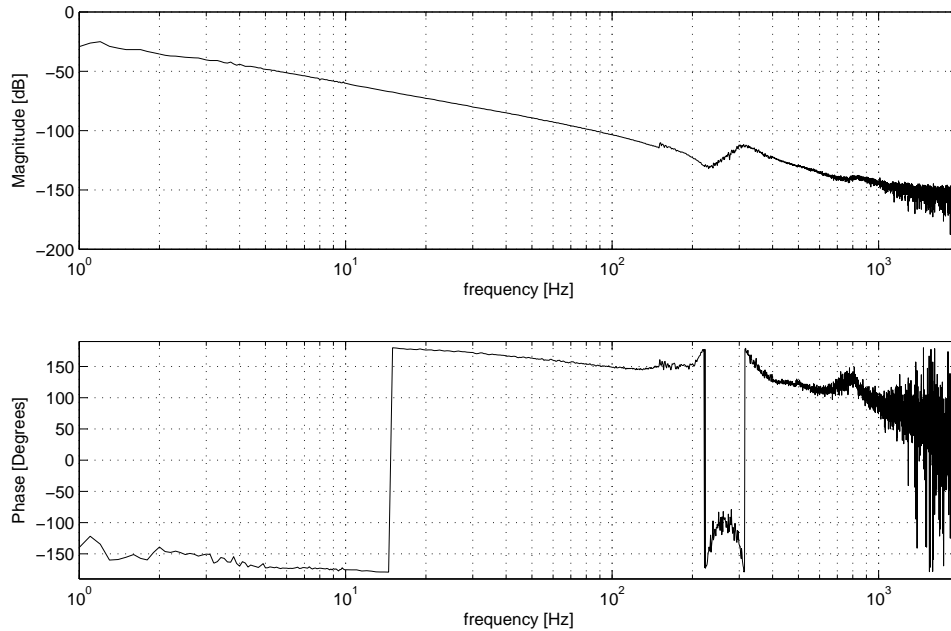


**Figure 4.12** / Plant FRF of the master and slave device. Eigenfrequencies are visible at 310 Hz and 820 Hz.

The quality of the haptic feedback is also influenced by the device friction. The friction force at the tip of the end effector is approximately 0.65 N for a clockwise (CW) segment

rotation (end effector moves downwards) and 0.45 N for a counterclockwise (CCW) segment rotation (end effector moves upwards) [9]. The friction torque of the DC motor itself is respectively 3.5-4 mNm and 2-2.5 mNm. This equals a force of approximately 0.5 N (CW) and 0.3 N (CCW) at the tip. The friction of the setup itself, as caused by the capstan drive and the two angular contact bearings, hence is in the order of 0.15 N.

An explanation for the difference in friction torque can be found in the placement of the brushes with respect to the collector segments. According to [55], the two brushes are made as lever brushes. This means that each brush is supported by a hinge. A spring presses the brush against the collector segments. If the rotation point of the brush is not placed on a line tangential with these segments, then the normal force and friction force depend on the direction of rotation of the rotor. With a continuous force level of 10 N, the friction level does not fulfill the  $\leq 1\%$  requirement as stated in the design specifications in section 4.2.

Another aspect is the torque ripple of the motor. The theoretical ripple of the motor depends on the number of commutation points. For the motor applied, the theoretical ripple is only 0.75% [54]. In practice, the ripple is increased by for instance brush and commutator arcing. The fact that the user can feel these disturbances makes that a DC motor with graphite brushes is not a good choice for a haptic setup.

#### 4.3.4 Position error controller

Based on the FRF data, a position error (PERR) controller is designed. This bilateral control architecture can be found in for example [32, 47]. The minimum bandwidth must be at least 60 Hz as kinesthetic and proprioceptive force sensing go up to about 30 Hz. As visible in figure 4.13, the PERR controller is based on two individual control loops, one for the master and one for the slave. The rotation of both setups is measured and subtracted from each other. This error is used as setpoint information for the lead/lag control loops. The input to the master controller is inverted to create a reaction force, which has an opposite sign with respect to the slave.

The controller is based on a lead/lag scheme, so as to limit the gain at high frequencies. Experiments have revealed that the lead/lag architecture can be tuned for a bandwidth up to 100 Hz in combination with a TUEACS and a sample frequency of 1 kHz. To increase robustness, it is limited to 80 Hz. Additional filters, like a low pass filter to deal with high-frequency noise or a notch filter to suppress resonance peaks are not implemented. The scaling factor between master and slave motion is set via the position scaling gain. The force feedback at the master can be disabled via the force feedback off/on switch. The force scaling switch allows to choose two different scaling levels.

For the situation as drawn in figure 4.13, the master and slave make use of an identical control algorithm. This means that the two setups have the same servo stiffness. When



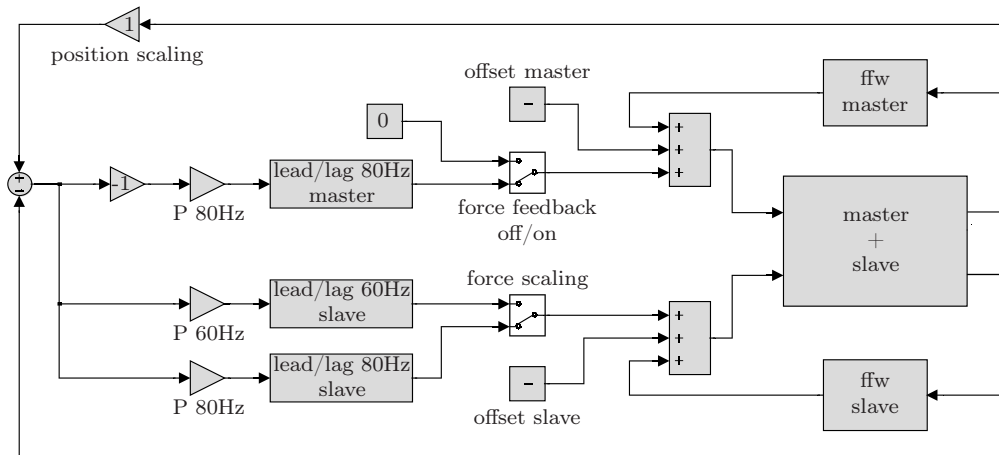


**Figure 4.13** / Position error (PERR) control architecture with feedforward. The position error between master and slave is used as the input for the master and slave controller. Position scaling and force scaling are implemented.

the end effector of the slave comes in contact with the environment, e.g. a rigid post, then the slave is not able to follow the movement of the master anymore. A position error between the master and slave is the result. This error times the servo stiffness results in the interaction force, which is identical for master and slave.

When the bandwidth of the slave is reduced to 60 Hz, then the slave will have a lower servo stiffness than the master. In this case, the interaction force between slave and environment is smaller than the interaction force between master and user: the forces are scaled upwards. The scaling ratio depends on the ratio between the two gains (P 60 Hz and P 80 Hz).

The friction is partially compensated via a friction feedforward (FFW) loop (figure 4.13). The direction of rotation is determined via a sign function (-1 or 1) out of the angular velocity of the setup. Depending on the direction of rotation, the amplifier is provided with a positive or negative offset voltage. A friction reduction of 90% is possible without causing limit cycling. As the desired trajectory is not known in advance, there must be first a rotation of the motor shaft before the friction can be compensated. This is in contrast with setpoint based servo control. The offset master block and offset slave block are added to deal with the asymmetric friction level in CW and CCW direction. Furthermore, it is used to compensate for the offset voltage of the amplifier to get an output current of 0 A.

The servo stiffness is determined by measuring the position error after applying a specific load on the end effector. For 80 Hz, it is  $6.8 \cdot 10^3$  N/m or 38 Nm/rad, for 60 Hz it is  $3.9 \cdot 10^3$  N/m or 22 Nm/rad. Also some initial measurements are done to reveal the forces during operation of the setup. Figure 4.14 gives the results of one of these

measurements. Successively a spring with a stiffness of  $3.0 \cdot 10^2$  N/m,  $1.2 \cdot 10^3$  N/m and a rigid post are placed under the end effector of the slave. The first peaks in each series are forces that a user can exert for a long period of time. The last peak in each series is the maximum force. A user can exert this force only for a short period of time.

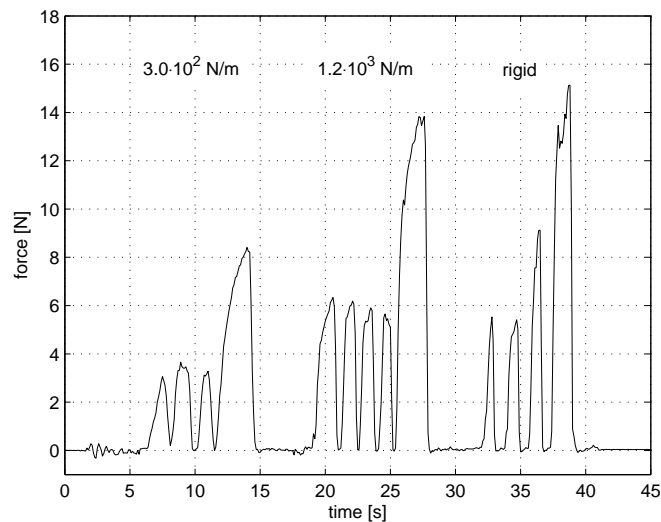


**Figure 4.14** / Typical forces during operation of the setup. Successively three objects with an increasing stiffness are placed under the end effector of the slave. There is no scaling in force or position between master and slave.

The exerted forces are lower than stated in the requirements. The maximum force can be reduced from 30 to 15 N and the continuous force from 10 to 5 N. For a very compliant environment, it is possible to work with a maximum force of 10 N and a continuous force of 3 N.

## 4.4 Single DoF linear setup

Besides the single DoF rotational master-slave, also a single DoF translational master is realized, see figure 4.15. This setup is not completely new designed but based on suitable, existing hardware. The direct drive concept and the absence of friction make it an ideal master for impedance control. A virtual environment or a 1 DoF rotational setup can be used as slave. Measurements and experiments are done to reveal the properties of the setup. The setup has been made available to K.J. Crommentuijn for his research on human factors for haptic feedback in medical robotics [19, 20, 82].

The setup consists of a base plate with two air bearing housings, each fitted with three air bearings. The bearings support the triangular beam and allow it to move in axial

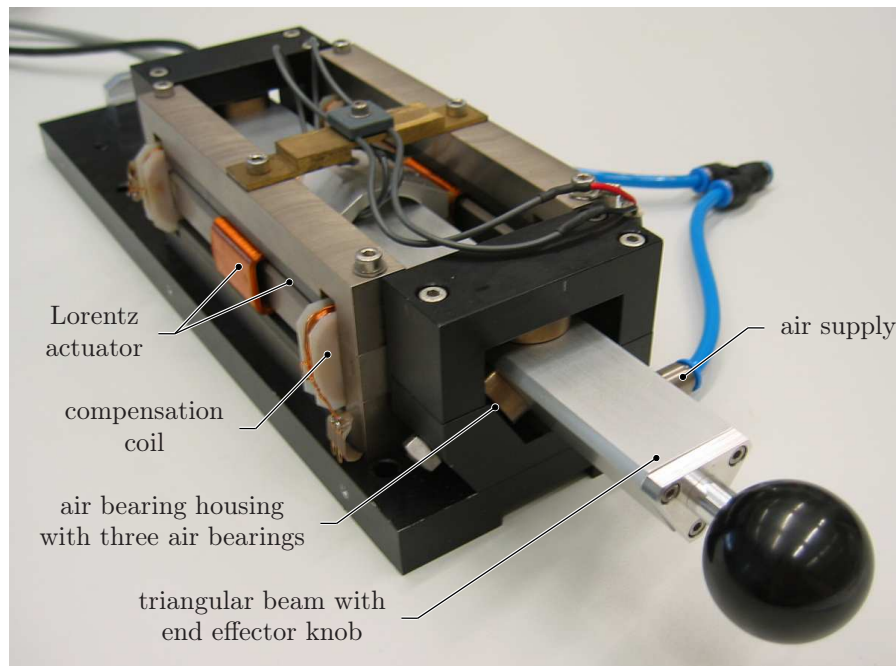


**Figure 4.15** / Single DoF linear setup

direction. The user manipulates the end effector via the knob. Force feedback is created by two, symmetrical placed, Lorentz actuators. The coils are glued to the beam, the yokes with permanent magnets are stationary and mounted on top of the base plate. The stroke of the setup is 80 mm. The moving mass of the beam with actuator coils is 0.53 kg (2.1 times higher than for the rotational setup). The setup can generate a continuous force of 3 N with only a slight increase in coil temperature. The maximum force is not determined.

### **Air bearings and air supply**

Six orifice type air bearings support the triangular beam, see figure 4.16. Two bearings act as preload bearing. The bearings must be aligned with the beam to achieve a parallel air gap in the order of 5-10  $\mu\text{m}$ . Hereto, three of the four lower bearings are supported by a bearing ball. The fourth bearing is supported by two bearing balls. In this way, the triangular beam is fixed in five DoFs, leaving one DoF: the axial movement of the beam. The preload bearings are piston type bearings. An o-ring seal allows the bearing to align with the bearing face of the beam. Bores in the bearing housings and bearing balls feed the air to the bearings.

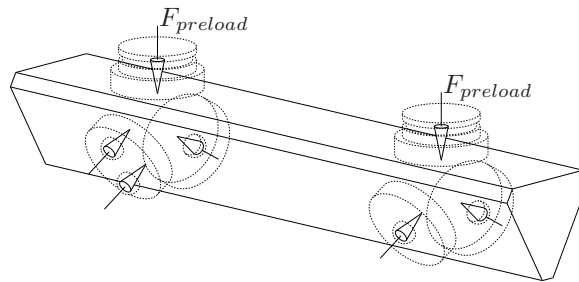


**Figure 4.16** / The triangular beam is supported in 5 DoF via the bearing balls and air bearings as indicated by the arrows. The two arrows at the top represent the two preload forces.

### Lorentz actuator

Two actuators are placed sideways of the beam. Each actuator consists of a yoke and a moving coil. The yoke is constructed out of three individual limbs. Two individual flux paths are created by ferrite magnets on the upper and lower limb. Both magnetic flux paths are closed symmetrically through the center limb. The flux density in the air gap is measured to be  $B = 0.16$  T. This value is relative low for Lorentz actuators, but this construction enables a long stroke without the need for commutation.

Since the cross section of the center limb is in the same order as that of the other two, this limb has the highest flux density. According to a FEA analysis with Ansoft Maxwell, the maximum flux density is  $B = 1.2$  T.

The flux in the air gap (and yoke) is influenced by the actuator coil itself. This effect is measured, see figure 4.17.

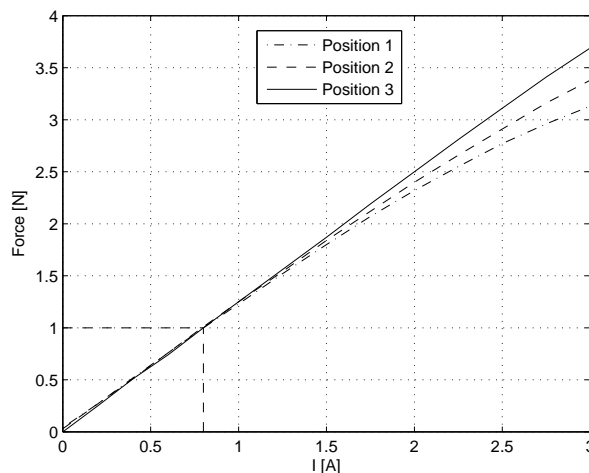


**Figure 4.17** / Actuator force as function of the current for three different coil positions. The relevant working area (up to 1 N) is indicated.

Position 1, 2 and 3 indicate a coil position at 0 mm, 40 mm and 80 mm of the stroke. For position 3, the actuator constant is  $K = 1.2 \text{ N/A}$ . For position 1, the same actuator constant is found for a current up to 1 A. For larger currents the actuator constant begins to drop. The additional coils on the center limb allow to compensate for this effect, but this is not necessary as the setup is only used for force levels up to 1 N [20].

### Position measurement

The system is provided with a differential variable reluctance transducer (DVRT) coil<sup>2</sup>, placed inside a central bore in the triangular beam. DVRTs have a single coil with a center tap. An AC excitation voltage is applied across the coil; the voltage at the center tap is proportional to the position. This working principle is comparable with a resistive voltage divider.

A new core and driving circuit are made to replace the missing parts. The driving circuit is based on a universal AD698 (half bridge) LVDT signal conditioner IC [2]. The IC contains a low distortion sine wave oscillator and a signal conditioning subsystem. The output gain and driving frequency are set by external capacitors and resistors. The frequency is set to 5 kHz giving an operational bandwidth of 0.5 kHz. The driving circuit and printed circuit board are visible in figure 4.18.

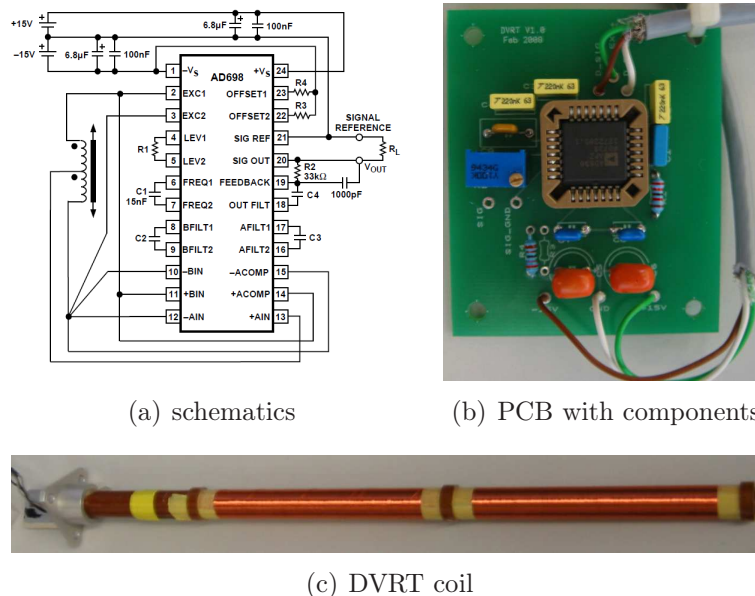


**Figure 4.18** / Differential variable reluctance transducer coil with driving circuit. The oscillator frequency of 5 kHz results in a bandwidth of 0.5 kHz.

<sup>2</sup>also known as half bridge linear variable differential transformer (half bridge LVDT)

The main advantage of a DVRT position measurement system is that it is absolute, which avoids the need for a homing procedure. The sensor characteristics are measured for different core lengths, see figure 4.19. The y-axis gives the output voltage of the driving/measurement circuit as function of the beam position (x-axis), as measured by a laser vibrometer. By varying the core length the system can be optimized for linearity or for minimal hysteresis. Achieved is a hysteresis level of 0.2 mm.

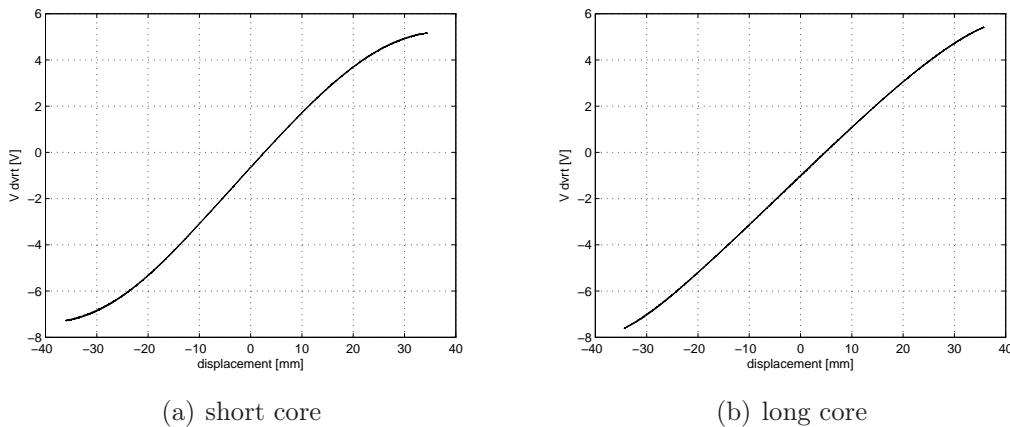


**Figure 4.19** / Output voltage of the DVRT as function of the displacement.

A higher accuracy is required to be able to use the setup as master device. Therefore, an optical encoder is added. The encoder read head with wires is mounted on the base plate. The encoder scale (40  $\mu\text{m}$  pitch) is glued to the bottom side of the beam. If desired, both measurement systems can be used simultaneously. The resolution of the optical encoder is 0.2  $\mu\text{m}$  with interpolation. The translational setup with optical encoder can be used directly in combination with the electronic cabinet for the rotational setup.

## 4.5 Conclusions

A single DoF master-slave system is designed and realized. The system has an identical master and slave with a rotational degree of freedom. The drive electronics with a PLC are integrated in a single electronic cabinet. Also, a single DoF translational master is realized out of existing hardware. It can be used in combination with the single DoF master-slave system. Table 4.3 gives the device properties of each of these systems.

The rotational setup is a compact, modular device. It has a high stiffness and is statically balanced for a uniform system behavior. A high resolution force and high resolution position measurement make it possible to use the system with different types

**Table 4.3** / Properties of the single DoF setups. The properties are measured at the tip of the end effector.

	rotational setup	linear setup
DoF	rotation	translation
continuous force	10 N	3 N
maximum force	30 N <sup>a</sup>	
resolution, position	1.6 $\mu\text{m}$	0.2 $\mu\text{m}$
resolution, force	10 mN	
inertia/ moving mass	0.25 kg	0.53 kg
friction (CCW/CW)	0.45/0.65 N	0 N
stiffness (motor shaft blocked)	$2 \cdot 10^5$ N/m	
lowest eigenfrequency	310 Hz	

a: limited for safety

of controllers, including the four channel haptic control algorithms. Force feedback is created via a brushed DC motor. The maximum force is  $F_{max} = 30$  N. Inertia match between motor and segment results in a high acceleration and deceleration. The motor drives a segment with an end effector via a backlash free and backdriveable capstan drive. The torque sensor to measure the force on the end effector is based on two inductive displacement sensors. The dual sensor differential setup gives a two times higher sensitivity and compensates for variations in room temperature. A PLC monitors the setup and disables the motor amplifiers in case of an unsafe situation, for example when an output force becomes too high or when something is wrong with the acquisition system. The system can be used with a TUE DACS or with a dSPACE<sup>®</sup> system.

The friction of the master and slave is between 0.45-0.65 N and depends on the direction of rotation. The main source is the friction torque of the motor. This torque is amplified 10 times by the capstan drive. The dependency to the direction of rotation is caused by the lever construction of the brushes.

Theoretically, the torque ripple is  $\leq 1\%$ , but in practice it is larger due to the interaction between the graphite brushes and the commutator. As the user feels this ripple, it is better to use a brushless DC motor in a haptic setup.

The simplified dynamic model and the FRF measurement show that the first eigenfrequency is approximately 310 Hz. The FRF model is used to design a position error controller. The controller is based on a lead/lag scheme and can be tuned for a bandwidth up to 100 Hz (in combination with a TUE DACS, 1 kHz sample frequency). This control algorithm shows that it is feasible to achieve force feedback and force scaling without measuring any forces. Experiments revealed that the force levels can be reduced with a factor three to  $F_{cont}=3$  N and  $F_{max}=10$  N.

---

The linear setup has a stroke of 80 mm and operates without friction. Force feedback is created by two, symmetrical placed, Lorentz actuators. This direct drive concept does not require commutation, is free of cogging and exhibits no torque ripple. The position is measured via a DVRT and an optical encoder. The encoder resolution is 0.2  $\mu\text{m}$ . The setup is used to study the impact of friction on positioning tasks. Hereto, different friction forces between 0 and 0.7 N are simulated [20]. Concluded is that a friction between 0.15 and 0.42 N gives an optimum in positioning speed and accuracy. This is less than the friction obtained from the rotational setup.





## CHAPTER FIVE

# Haptic interface

---

**Abstract /** Two haptic interfaces are realized for a bimanual manipulation of the instruments. Each haptic interface has five degrees of freedom. All DoFs have a force feedback motor and an encoder for the position measurement. Disturbance forces are minimized as they interfere with the force feedback. The interface allows to manipulate an instrument in an intuitive and comfortable way.

This chapter discusses the design considerations, the design and the working principle of the haptic interface. Section 5.3 is about the results.

## 5.1 Design considerations

All five DoFs of the interface (see figure 3.5) must have a position encoder to measure the hand motions and a force feedback motor to provide the surgeon with the upscaled instrument forces. Motors and encoders must be placed in such way that they do not interfere with the surgeon's hand and forearm. For safety, the motors and encoders must operate in the low voltage range. This means that  $V_{max}=42$  V.

As concluded in chapter 4, it is better not to use DC motors with graphite brushes. Therefore, the haptic interface will be based on brushless DC motors. There are two types: ironless and iron core motors. An ironless motor is preferable, as it features cogging free operation. The force feedback is further improved if the total friction is kept low by applying a direct drive concept or a low geared transmission. This also guarantees backdrivability, which is necessary as the haptic interface will not be equipped with a force/torque sensor.

The most comfortable feeling during a  $\varphi$  and  $\psi$  rotation is achieved when the rotation point of the stylus is placed directly above the surgeon's wrist. For the human hand, the distance between wrist joint and finger tips is  $\approx 150$ - $175$  mm. This value is adopted

for the length of the stylus and gives a scaling ratio of 1:6-1:7 for an insertion depth of 24 mm. The surgeon manipulates the stylus via a button part.

Scaling proportional to the pen length leads to a  $z$  stroke of 150-175 mm. A stylus length of  $\ll 150$  mm or  $\gg 175$  mm gives a forced and uncomfortable  $\varphi$ - $\psi$  rotation of the button part between the fingertips. Therefore, the applicable  $z$  stroke is smaller. To control the instrument in its whole range, one could think of a jogging mode: a combination of velocity and positional control. Such mode is also useful for the  $360^\circ + \theta$  rotation of the instrument, as the human hand does not allow for larger rotations than  $180^\circ$ .

The button part has to be small enough to fit nicely in between the fingers of the surgeon, but must leave enough free space for an actuator and an encoder. Actuation of this fifth DoF must not result in a lateral or axial movement of the stylus and instrument tip, as this makes it more difficult to grasp and peel a membrane. A precise operation of the forceps can be obtained if the surgeon grasps the button part like a pen. The surgeon uses his thumb and middle finger to grab and manipulate the button part. With his index finger he operates the button.

Table 5.1 gives the requirements for the different DoFs of the haptic interface. The requirements are based on the instrument movements as summarized in table 2.1 and the force levels as found during the experiments with the single DoF rotational setup ( $F_{cont} = 3$  N,  $F_{max} = 10$  N). To calculate the  $\theta$  torque, it is assumed that the surgeon's thumb and middle finger are each at 10 mm from the centerline. This distance times the interaction force gives the desired torque. The  $\theta$  resolution is based on the same distance in combination with the surgeon's hand accuracy of  $50 \mu\text{m}$  [74].

The maximum  $z$  force and  $\theta$  torque are limited to respectively 5 N and 50 mNm to prevent slip between the surgeon's fingers and the button part. These values as well as the  $z$  range and the *button* force are determined empirically. Furthermore, the  $\psi$  range is enlarged with  $10^\circ$  to match the  $\varphi$  range. This gives a more symmetrical workspace. In the last place, the button has a two times larger stroke for a more precise operation of a forceps. These two improvements do not have a negative side effect on the design of the haptic interface.

Besides the haptic interfaces, it is also necessary to have a support frame with coarse adjustment abilities to do the initial experiments.

## 5.2 Design and working principle

Figure 5.1 is a photo of the two haptic interfaces with temporary test frame and coarse adjustment arms [31, 37, 48]. The operator can manipulate two instruments simultaneously.

**Table 5.1** / Requirements for the haptic interface. The DoFs are according to figure 1.6. The resolution and force levels in  $\varphi$  and  $\psi$  are specified at the tip of the interface.

	$\varphi$	$\psi$	$z$	$\theta$	button
range	$\pm 45^\circ$	$\pm 45^\circ$	15 mm	$\pm 90^\circ$	5 mm
resolution	50 $\mu\text{m}$	50 $\mu\text{m}$	50 $\mu\text{m}$	0.3°	50 $\mu\text{m}$
continuous force/torque	3 N	3 N	3 N	30 mNm	2 N
maximum force/torque	10 N	10 N	5 N	50 mNm	5 N

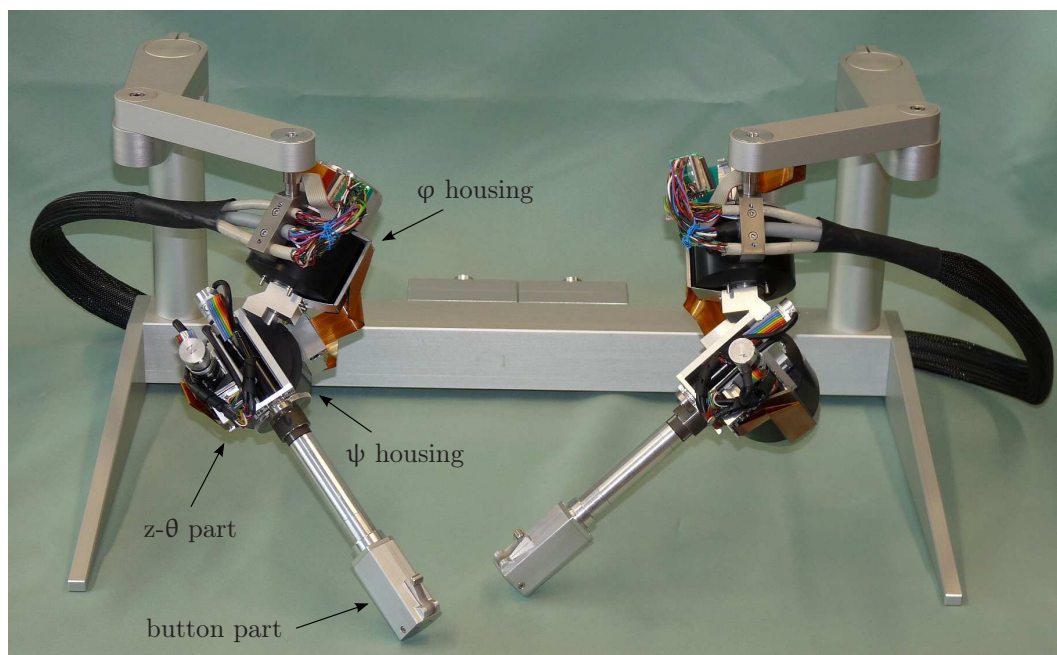


**Figure 5.1** / 5 DoF haptic interfaces. Visible are the left and right pen with a temporary supporting frame.

There are four parts in each haptic interface in accordance with the different DoFs:  $\varphi$  housing,  $\psi$  housing,  $z$ - $\theta$  part and a button part (see figure 5.2). The  $z$  and  $\theta$  DoF are actuated in a parallel way. The other three DoFs are placed in a serial layout. Allocation is according to the instrument movements during surgery. For example, the  $z$  movement and  $\theta$  rotation is always along the centerline of the instrument and therefore they are placed after  $\varphi$  and  $\psi$  in the kinematic chain.

A serial  $\varphi$ - $\psi$  layout is chosen to simplify the design and to have an identical kinematic layout for the master and slave. Although there is no strict necessity, this simplifies the initial tests and experiments. Furthermore, the  $\varphi$  and  $\psi$  range can be increased easily without negative side effects like a reduction in stiffness. This can be useful for working with various scaling factors. A disadvantage of the serial layout is a higher inertia since the  $\psi$  motor moves along with a  $\varphi$  rotation. Alternative layouts are investigated in

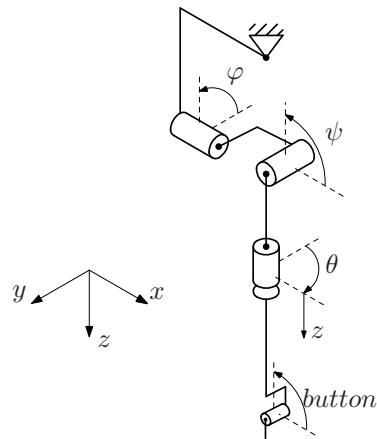


**Figure 5.2** / Kinematic layout of the 5 DoF interface.

chapter 6. They may require custom 2 DoF spherical motors or alternative, parallel layouts.

### 5.2.1 $\varphi$ and $\psi$ housing

The mechanical design of the  $\varphi$  and  $\psi$  part is almost identical and therefore only the  $\varphi$  part as visible in figure 5.3 is discussed.

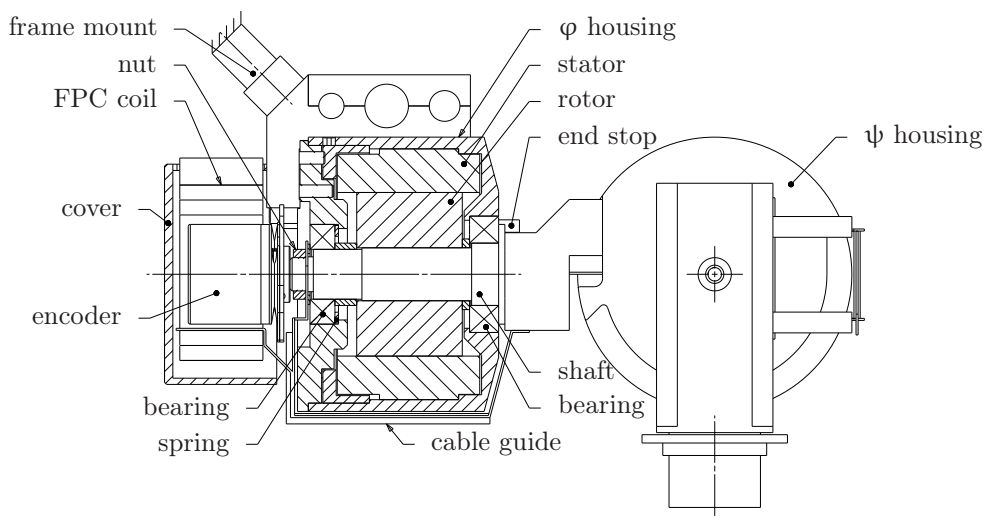


**Figure 5.3** /  $\varphi$  housing. A cross section of the  $\varphi$  axis reveals the mechanical layout.

The core of the  $\varphi$  part is a frameless and brushless DC motor. The stator of the motor is glued in a compact housing. The housing is made in two parts, a cup and a cover, each fitted with a ball bearing to support the shaft. A nut fixates the rotor and the

inner rings of the ball bearings on the shaft by axial compression via the distance pieces. The spring pretensions both bearings via the outer rings to achieve an O arrangement. This is done to increase the stiffness and to eliminate play. The  $\psi$  housing, visible on the right side of figure 5.3, is attached to the right side of the shaft. The encoder to measure the  $\varphi$  rotation of the haptic interface is placed on the left end of the shaft. Around the encoder a flexible printed circuit (FPC) is wrapped, which goes to the  $\psi$  housing via a cable guide. A cover protects the encoder and FPC. Two end stops limit the  $\varphi$  rotation to  $\pm 90^\circ$ . The end stop for the  $\psi$  rotation is integrated in the housing. Here, the maximum rotation is set to  $-45^\circ$  and  $+88^\circ$ . The latter to prevent a singularity due to the otherwise possible alignment of the two rotation axes. In figure 5.4 the end of range positions are drawn.

### DC motor and encoder

A brushless DC motor is implemented to prevent the torque ripple as discussed in section 4.3.3. As visible in figure 5.5(a), the stator of the motor is an iron core type. Compared to an ironless motor, this motor features a more compact layout and reduces the inertia of the  $\varphi$  movement. A small drawback is the cogging torque of 0.01 Nm (0.06 N at the tip), induced by the variable reluctance between stator and rotor. This is only a low frequency variation and it is to be expected that the user will not notice this at all. Otherwise, a feedforward can be implemented as compensation.

The specifications of the motor are summarized in table 5.2.

**Table 5.2** / Motor specifications for the  $\varphi$  and  $\psi$  DoF.

continuous stall torque	0.51 Nm	pole pairs	6
continuous current	3.2 A	inertia	$3.46 \cdot 10^{-5} \text{ kgm}^2$
maximum torque	1.66 Nm	resistance	2.6 $\Omega$
maximum current	9.9 A	back EMF	17.3 V/krpm
motor constant	0.17 Nm/A		

Different winding types are available for the motor. The winding with the highest resistance is chosen to minimize the motor current and the requirements for the amplifiers. Additionally, a lower current reduces the power dissipation in the wiring between amplifier and motor (see section 5.2.4). The motor requires a bus voltage of 26 V to generate the maximum torque of 1.66 Nm. Influence of back EMF is negligible as interface movements are very slow.

As the direct drive layout has no transmission, it is not possible to tune for inertia

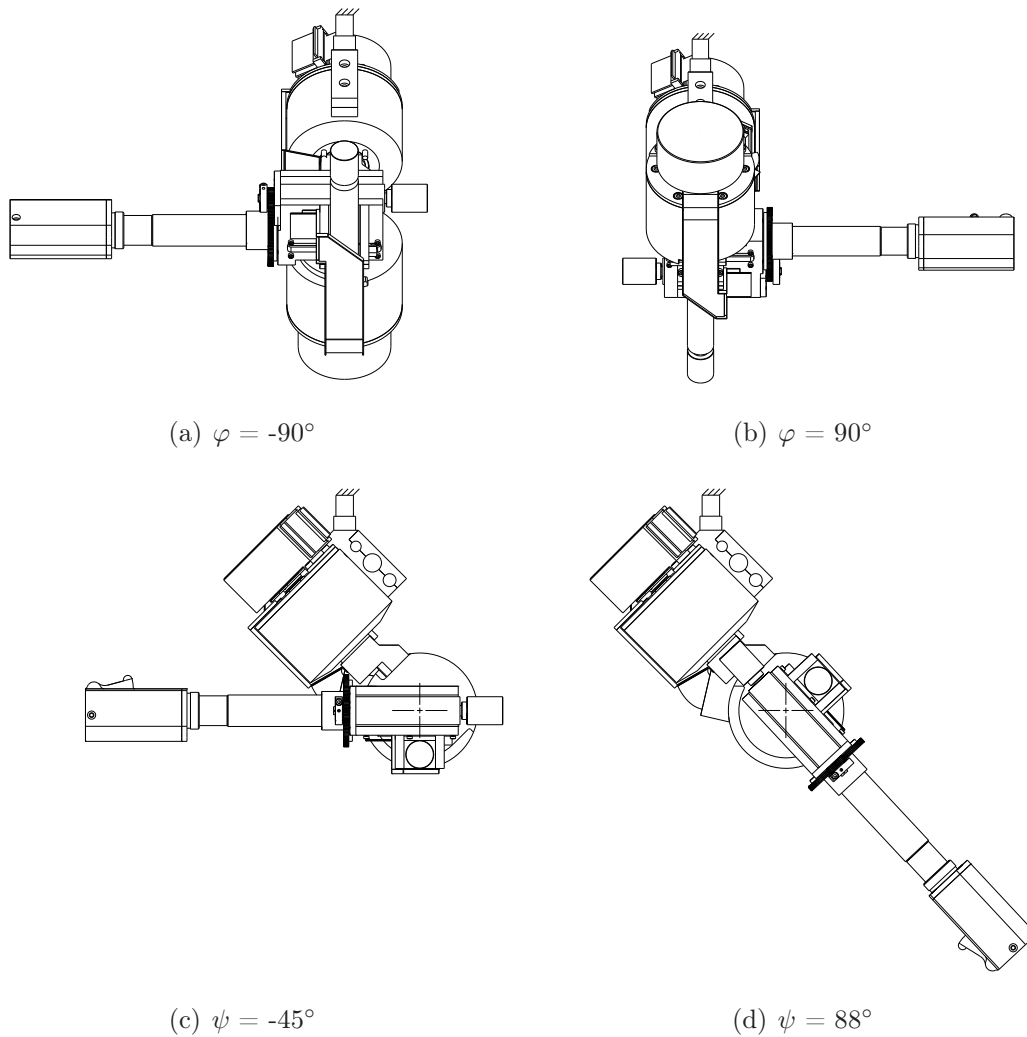


**Figure 5.4** / Range of motion of the  $\varphi$  and  $\psi$  DoF. Four end stops are integrated to protect the flexible printed circuits. The end stop in the positive  $\psi$  direction is set on  $88^\circ$  to prevent a singularity.

match between motor and load (haptic interface). Here, the motor is specified on the continuous and maximum torque. Maximum acceleration and deceleration is given by the maximum torque and the total system inertia. With a  $\varphi$  and  $\psi$  inertia of  $4.9 \cdot 10^{-3} \text{ kgm}^2$  and  $2.9 \cdot 10^{-3} \text{ kgm}^2$  and a torque of 1.66 Nm, the accelerations are  $\pm 3.4 \cdot 10^2 \text{ rad/s}^2$  and  $\pm 5.7 \cdot 10^2 \text{ rad/s}^2$ . This allows a representation of a stiffness up to  $5 \cdot 10^6 \text{ N/m}$  at the tip when an angular velocity of 0.06 rad/s (velocity at the tip:  $v_{tip}=1 \text{ cm/s}$ ) is assumed. A stiffness in the order of 60-140 N/m [43] is required.

The encoder is identical to the one applied in the 1 DoF rotational setup. In this case, the 30,000 counts/rev. results in a resolution of  $37 \mu\text{m}$  at the tip of the haptic interface. This corresponds with  $5 \mu\text{m}$  at the instrument tip if no additional scaling is applied.



(a) frameless DC motor (stator),  
dimensions:  $\varnothing 60 \times 34$  mm

(b) hollow shaft encoder, dimen-  
sions:  $\varnothing 24 \times 20$  mm

**Figure 5.5** / The motor and encoder as applied for the  $\varphi$  and  $\psi$  DoF. The encoder is provided with a flexible coupling to prevent an over-constrained construction between motor and encoder shaft.

The encoder shaft and motor shaft are each suspended in two ball bearings. Mounting the encoder directly on top of the motor housing results in a five times over-constrained construction. The flexible coupling between encoder and motor decouples these five DoFs. The sixth DoF, the rotation of both shafts, is coupled with a high stiffness.

### 5.2.2 z- $\theta$ module

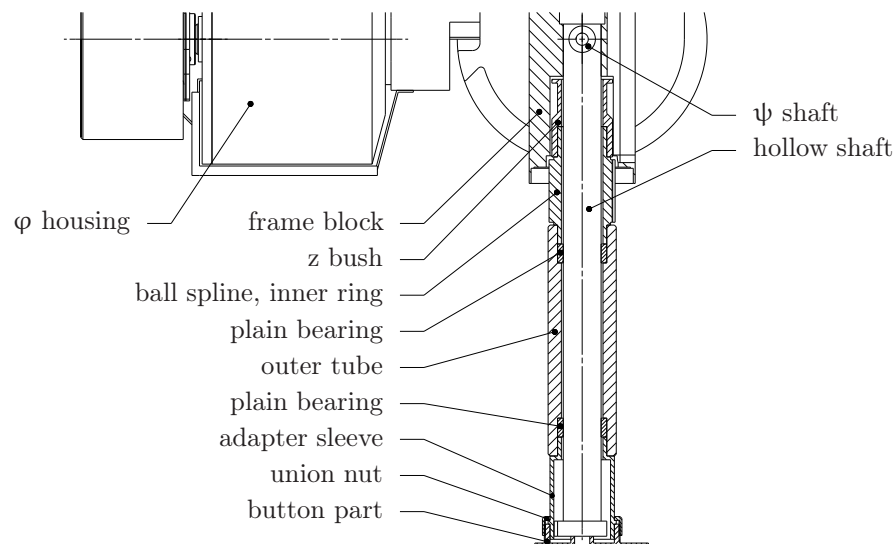


**Figure 5.6** / Detail  $\theta$ -z module. The shaft is fixated in the frame block and acts as a guidance for the hand held outer tube with button part.



The frame block and the hollow shaft are the base parts of the  $z$ - $\theta$  module. The frame block is the rigid connection of the hollow shaft to the  $\psi$  shaft. Two bearing bushes guide the hand held outer tube around this hollow shaft leaving two degrees of freedom:  $\theta$  and  $z$ , each driven by a DC motor which serves for force feedback to the surgeon in the way described below. Two encoders on the rear of the DC motors measure the  $z$  displacement and  $\theta$  rotation. The button part is mounted at the lower end of the outer tube.

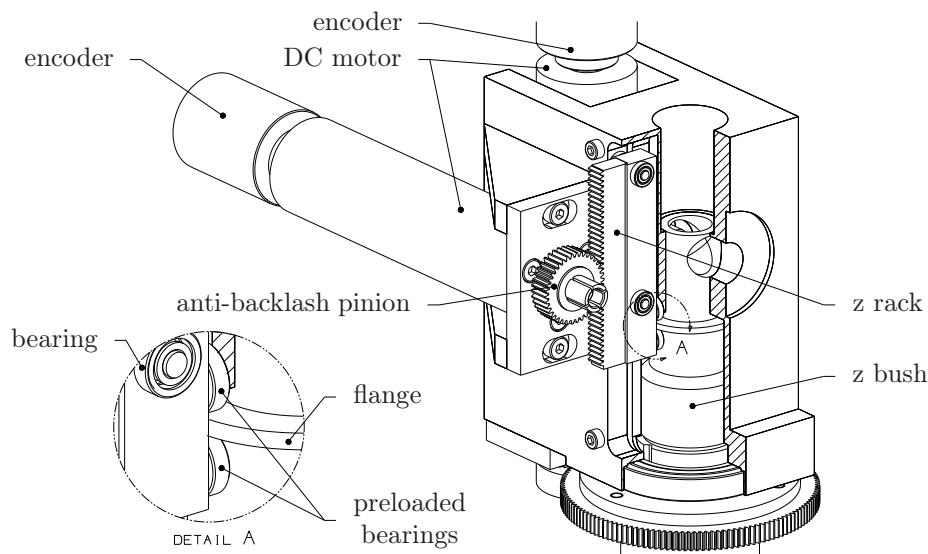


**Figure 5.7** / Detail of the  $z$  drive. The motor torque is transmitted via a pinion and rack and from there via two preloaded ball bearings on a flange (which frees  $\theta$ , see detail A) to the hand held outer tube.

Figure 5.7 is a section view of the  $z$  drive. This  $z$  drive works with a rack and pinion transmission. The pinion is an anti-backlash gearwheel, mounted on the motor shaft. The gear module is chosen small: 0.3 to achieve a smooth operation. Two preloaded bearings on the  $z$  rack drive the  $z$  bush via a flange to decouple the  $z$  drive from the  $\theta$  rotation. Four miniature bearings (one indicated) guide the rack inside a slot in the frame block.

A ball spline decouples the  $\theta$  drive from the  $z$  movement (figure 5.8). The outer and inner ring of the ball spline are each provided with three mating axial v-grooves. Three miniature bearing balls are placed in each set of opposed grooves. The inner ring is thereby connected in rotation and radially to the hand held outer tube. The radial ball bearing supports the outer ring in  $z$  direction. The motor drives the outer ring via a pinion/gearwheel transmission. To prevent backlash, the balls in the v-grooves are pretensioned and for the pinion an anti-backlash type is used.

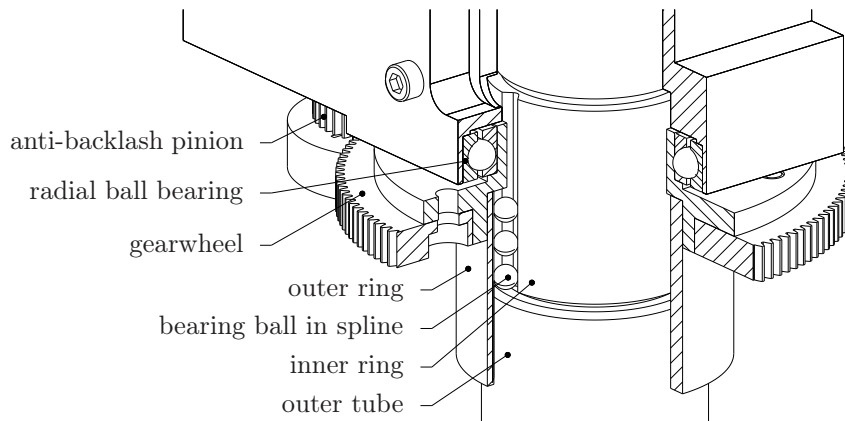


**Figure 5.8** / Detail  $\theta$  drive. The motor torque is transmitted via a pinion and gearwheel and from there via a ball spline to the hand held outer tube. The ball spline decouples the  $\theta$  drive from the  $z$  movement.

### DC motor and encoder

The  $z$ - $\theta$  frame block moves along with the  $\varphi$  and  $\psi$  rotation. Small force feedback motors for the  $z$  and  $\theta$  DoFs are desirable for a compact design. Therefore, two 16 mm ironless, brushless DC motors with gearwheel transmission are implemented. Table 5.3 gives the specifications of the  $z$  and  $\theta$  motor. The motors are equipped with a 20,000 counts/rev. encoder. This gives a resolution of  $1.8 \mu\text{m}$  in  $z$  and  $88 \mu\text{rad}$  in  $\theta$ .

**Table 5.3** / Motor specifications for the  $z$  and  $\theta$  DoF.

continuous stall torque	13.9 mNm	pole pairs	1
continuous current	2.5 A	inertia	$1.3 \cdot 10^{-7} \text{ kgm}^2$
maximum torque	184 mNm	resistance	$0.7 \Omega$
maximum current	33.5 A	back EMF	$0.57 \text{ V/krpm}$
motor constant	$5.5 \text{ mNm/A}$	nominal voltage	24 V

### 5.2.3 Button part

The button part measures  $26 \times 30 \times 58 \text{ mm}^3$  and offers two parallel surfaces for a tight grasp between thumb and middle finger. The surgeon uses his index finger for the operation of the button. The button remains always in reach, as it moves along with the surgeon's hand motions.

A section view is visible in figure 5.9. The gear segment with button is supported by two small diameter plain bearings in the two housing parts. A flat DC motor provides

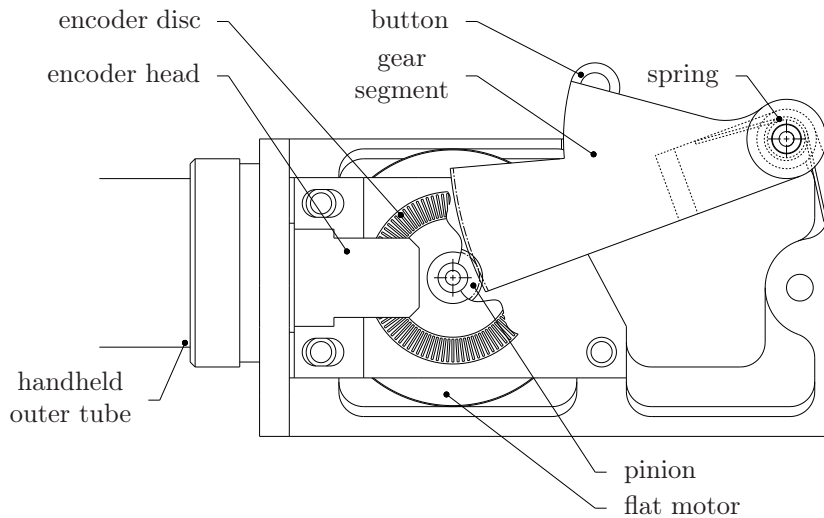


**Figure 5.9** / Section view of the button part. A flat DC motor provides the force feedback.

the force feedback (see table 5.4). Due to the limited space, a self commutating DC motor with precious metal brushes is applied. This is in contrast with the brushless motors as applied for the other four DoFs. The precious metal brushes make that the relative torque variation of the flat motor is less than that of a DC motor with graphite brushes.

**Table 5.4** / Motor specifications for the flat motor.

continuous stall torque	3 mNm	inertia	$6.8 \cdot 10^{-8} \text{ kgm}^2$
continuous current	0.16 A	resistance	36.5 $\Omega$
maximum torque	6.2 mNm	back EMF	2 V/krpm
maximum current	0.32 A	nominal voltage	12 V
motor constant	19.1 mNm/A		

The flat motor drives the gear segment via a pinion. The gear ratio is  $i = 1/12.5$ . Motor and pinion are adjustable to minimize backlash. The encoder head measures the rotation of the motor shaft via the encoder disc. The head is also adjustable to set the correct optical radius.

The surgeon operates the button by pushing it inwards. A small and light spring is added to move the button outwards, thereby maintaining contact with the index finger within the operating range of the button. Hereby, the flat motor can provide a force to simulate for instance a clamping force of a pair of tweezers via software scaling.

### 5.2.4 Wiring and electronics

Table 5.5 gives an overview of the number of wires per degree of freedom and the continuous and maximum current per wire.

**Table 5.5** / Number of wires per DoF and continuous and maximum current.

	component	$I_{cont}$ [A]	$I_{max}$ [A]	number of wires
$\varphi$ and $\psi$	motor	3	10	2x3
	hall	-	0.09	2x5
	encoder	-	0.04	2x8
$z$	motor	2	4	3
	hall	-	0.09	5
	encoder	-	0.04	8
$\theta$	motor	1.2	2	3
	hall	-	0.09	5
	encoder	-	0.04	8
<i>button</i>	motor	0.15	0.3	2
	encoder	-	0.04	4

In total, 70 wires are required, 54 of these wires have to jump from the  $\varphi$  to the  $\psi$  housing, 38 from  $\psi$  to the  $z$ - $\theta$  module and six from  $z$ - $\theta$  to the button part. As the stiffness and damping of the wires interfere with the force feedback, it is important that the disturbance forces are as low as possible. Therefore, two 40 way, 0.5 mm pitch, flexible printed circuits (FPCs) are implemented. They are placed on top of each other and are wrapped loosely around the encoders of the  $\varphi$  and  $\psi$  DoF to keep the length and diameter of the housings within limits. Cable guides direct the FPCs over the  $\varphi$  and  $\psi$  housings towards the  $z$ - $\theta$  module. One cable is for the *button* and  $\psi$  DoF, the second is for  $z$  and  $\theta$ . The  $\varphi$  motor and encoder are stationary and are connected directly to the interface cables. The connection between the  $z$ - $\theta$  module and the button part is made via a standard 6 way flat flexible conductor (FFC). The FPCs realized and a part of the routing are visible in figure 5.10 and 5.11.

The conductors at the top layer are 70  $\mu\text{m}$  thick and have three different widths: 2.3 mm for the  $\psi$  motor, 0.8 mm for the  $z$  and  $\theta$  motor and 0.3 mm for the hall signals, encoder signals and the motor inside the button part. The maximum FPC length is restricted to 600 mm, 400 mm less than required. Therefore, two identical FPCs are placed in series for  $z$ - $\theta$  and two for the button. The interconnection between the FPCs and with the  $\psi$  motor is made via PCBs on the  $\psi$  housing.

Each motor phase conductor is shielded by +5V and GND signals to prevent an electromagnetic interference (EMI) with the TTL signals of the encoder and hall sensors.

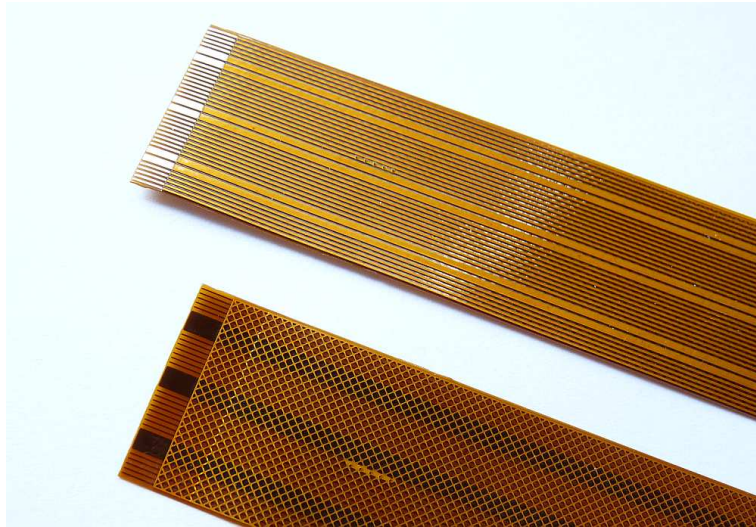


**Figure 5.10** / Front and backside of the 20.5 mm wide FPCs. The 2.3 and 0.8 mm wide conductors are for the motor currents, the 0.3 mm conductors are for the hall and encoder signals. The hatched shielding protects against electromagnetic interference between the two stacked FPCs.

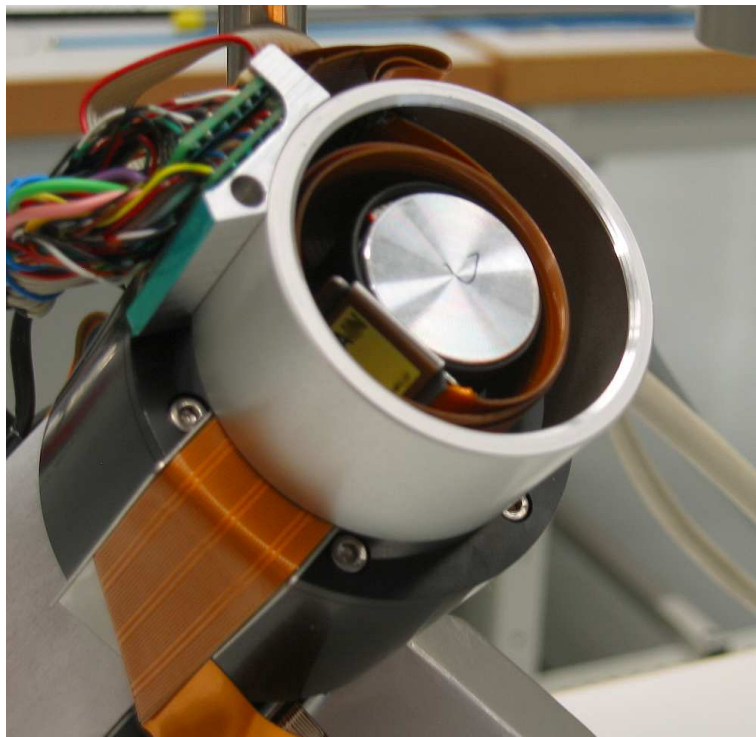


**Figure 5.11** / Detail view of the wiring on the  $\varphi$  housing. Visible are the FPC coil around the  $\varphi$  encoder, the cable guide and two printed circuit boards for the interconnection between the interface cables and FPCs.

The hatched shielding at the bottom layer is connected to GND and prevents EMI between the two stacked FPCs. It also acts as a heat sink for the power dissipation in the 0.8 and 2.3 mm wide motor phase conductors. Table 5.6 gives an overview of this dissipation.

**Table 5.6** / Dissipation in the FPCs per DoF per meter as result of the nominal motor currents. The  $\varphi$  DoF is not listed, as it is directly connected to the interface cables.

	$A_{conductor}$ [mm <sup>2</sup> ]	$I_{cont}$ [A]	$R$ [ $\Omega$ ]	$P_{diss}$ [W]
$\psi$	$2.3 \cdot 0.07$	3	$2 \cdot 0.1$	1.8
$z$	$0.8 \cdot 0.07$	2	$2 \cdot 0.3$	2.4
$\theta$	$0.8 \cdot 0.07$	1.2	$2 \cdot 0.3$	0.9

The highest current density and the largest FPC length is found around the  $\varphi$  encoder. With a length of 0.3 m, the power dissipation is approximately 1.5 W. Temperature measurements revealed that the increase in FPC temperature is neglectable compared to the temperature rise of the motors itself.

Two different types of amplifiers are required for the five DoF haptic interface. One to drive the electronic commutated, brushless motors and one to drive the brushed motor inside the button part. The difference is that a brushless motor amplifier energizes the three motor windings according to the hall and encoder signals of the motor. A brushed motor drive does not need this feature, as commutation is performed by the motor itself. Furthermore, the maximum current of the motor in the button is much lower than for the other DoFs.

Initially, functional tests on the  $\varphi$ ,  $\psi$ ,  $\theta$  and  $z$  DoFs are done with a four channel amplifier cabinet (figure 5.12). Integrated are a power supply and four Maxon DES 50-5 servo amplifiers. This amplifier has a 50 kHz pulse width modulation and a sinusoidal commutation to minimize torque ripple. A serial RS232 connection allows configuration (like setting current limits), monitoring and to use a DoF directly in current or speed mode.

Besides RS232, a connection can be made with an acquisition system like dSPACE<sup>®</sup>. This enables experiments in more DoFs simultaneously. Different safety measures are implemented in the digital signal processor (DSP) of the amplifier: continuous and maximum motor current, hall sensor signal check and encoder signal check are the most important ones. The DSP disables the H-bridge (output stage) in case of an error. Therefore, no additional PLC layer is added.

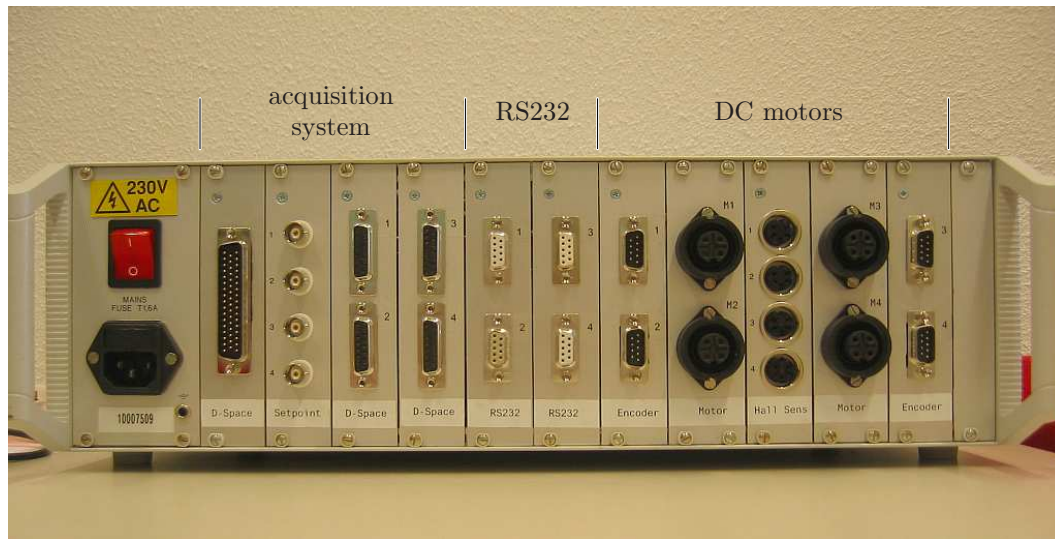


**Figure 5.12** / Four channel amplifier cabinet. The connectors for the acquisition system and for the motors with encoders are grouped. Configuration and monitoring is done via the four RS232 connectors.

### 5.3 Results

Table 5.7 gives an overview of the properties of the realized haptic interface. All ranges and resolutions are better than specified in table 5.1. This is not the case for some of the forces. Initial experiments show that this is not a problem at all as the force and torque levels were set to high. The maximum force and torque can be reduced to 5 N for  $\varphi$  and  $\psi$ , 3 N for  $z$ , 40 mNm for  $\theta$  and 2 N for the *button*. The continuous force or torque can be set on one third of these values.

**Table 5.7** / Properties of the 5 DoF haptic interface, measured at the tip in nominal position without PCBs and wires. The moving mass/inertia is determined via the CAD package NX.

	$\varphi$	$\psi$	$z$	$\theta$	<i>button</i>
continuous force/torque	3 N	3 N	2,4 N <sup>a</sup>	0.05 Nm	1.9 N <sup>a</sup>
maximum force/torque	9.5 N <sup>a</sup>	9.5 N <sup>a</sup>	32 N <sup>b</sup>	0.65 Nm <sup>b</sup>	3.9 N <sup>a</sup>
range	180°	133°	16 mm	340°	5 mm
resolution	37 $\mu$ m	37 $\mu$ m	1.8 $\mu$ m	0.1 mrad	25 $\mu$ m
moving mass/ inertia	0.17 kg	0.11 kg	0.16 kg	$2.2 \cdot 10^{-5}$ kgm <sup>2</sup>	0.04 kg
friction (left/right)			0.35/0.5 N	3/4.5 mNm	

a: requirement not met

b: will be limited for safety

An explanation for these differences can be found in the way how the user operates the single DoF rotational setup and the five DoF haptic interface. In the first case, the user holds the end effector in a pinch grip (between thumb and index finger) and pushes directly with the thumb on the end effector. This grip makes it easier to exert large forces than with the pencil like grip as applied with the haptic interface. Here, a possible slip between the button part and the user's fingers limits the force feedback level.

Furthermore, four SISO closed loop measurements are made on the right haptic interface to reveal the dynamical properties of respectively the  $\varphi$ ,  $\psi$ ,  $\theta$  and  $z$  DoF.

Figure 5.13 gives the block scheme. Measured are the signals  $u_t$  and  $u_s$ . A multisine is used as input  $i$ .

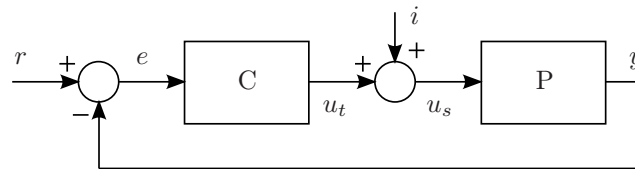


**Figure 5.13** / Block scheme as used for the closed loop measurements, with: controller  $C$ , plant  $P$ , reference signal  $r$ , error  $e$ , input  $i$  and output  $y$ . The signals  $u_t$  and  $u_s$  are measured.

The measurements provide the sensitivity, i.e. transfer of  $i$  to  $u_s$ ,  $S = 1/(1 + CP)$  and complementary sensitivity, i.e. transfer of  $i$  to  $u_t$ ,  $T = CP/(1 + CP)$  with  $C$  the controller and  $P$  the plant. The open loop system is obtained by:  $CP = T/S$ . As the controller  $C$  is known, it is possible to reconstruct the plant  $P$ .

The  $\varphi$  DoF is identified with the stylus in its nominal position, the other three DoFs are identified with the stylus moving in a horizontal plane. The Bode plot of the  $\varphi$  axis is visible in figure 5.14. The other three plots can be found in appendix B.

The lowest eigenfrequency is measured for the  $\varphi$  axis and equals 37 Hz, where approximately 60 Hz is desired. The main reason is the relative high inertia for this DoF, as a result of the serial kinematic layout. The  $\theta$  and  $z$  measurements are (strongly) influenced by the friction. This means that these DoFs need additional attention to improve the haptic feedback.

Currently, the interface is not statically balanced. This unbalance acts as a disturbance force on the surgeon's hand. This force depends on the orientation of the stylus. The maxima in  $\varphi$ ,  $\psi$  and  $z$  are respectively 1.3 N, 1.2 N and 1.6 N for a nominal  $z$  position. The  $\varphi$  and  $\psi$  force are almost identical, in spite of the additional  $\psi$  motor, encoder and housing. This is a result of the orientation of the  $\varphi$  axis. Counterweights can be added



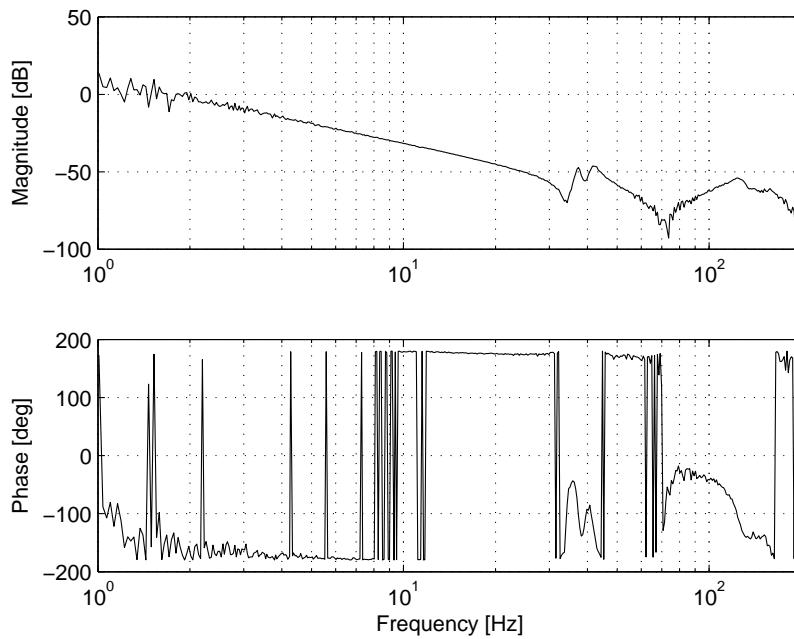


**Figure 5.14** / Bode plot of the  $\varphi$  DoF. The measurement is done with the stylus in its nominal position.

to balance the interface, but in first instance, it will be done via a feedforward on the  $\varphi$ ,  $\psi$  and  $z$  DoF.

The similarity in DoFs between vitreo-retinal eye surgery and minimally invasive surgery makes it possible to do experiments in combination with a slave robot for laparoscopic and thoracoscopic surgery [7, 8]. The slave robot is realized at the TU/e and consists of a table mounted coarse adjustment with a maximum of three instrument manipulators (IMs). Each IM enables an instrument to be moved in  $\varphi$ ,  $\psi$ ,  $\theta$  and  $z$ . The haptic interface allows to manipulate an instrument in a comfortable and intuitive way.

## 5.4 Conclusions

A preliminary design is made of a five DoF haptic interface. Two interfaces are realized for bimanual manipulation. Each device consists of four modules: a  $\varphi$  housing, a  $\psi$  housing, a  $z$ - $\theta$  part and a button part. The modules are placed in series. The surgeon manipulates the interface via the button part about a virtual entry point, which is the intersection point of the three rotation axes. The rotation point is placed above the surgeon's wrist. The distance between the virtual entry point and the button is 175 mm. Furthermore, a temporary test frame and a four channel amplifier cabinet are built to do the functional tests and initial experiments in  $\varphi$ ,  $\psi$ ,  $z$  and  $\theta$ . The amplifiers feature a sinusoidal commutation to avoid torque ripple.

A direct drive concept is applied for the  $\varphi$  and  $\psi$  DoF. The actuation in  $\theta$  and  $z$  is done via backlash free gearwheel transmissions, as the available space is too small for direct drive. The three rotations and the  $z$  translation are driven by brushless DC motors and measured with commercially available high resolution encoders. The button part is equipped with a brushed DC motor and a modified optical encoder. The damping and stiffness of the required motor and encoder wires will interfere with the force feedback. Therefore, two 40 way, 0.5 mm pitch, flexible printed circuits are implemented. The disturbance force as felt by the surgeon of these FPCs is only 10 mN. The required bus voltage is  $\leq 30$  V. This means that the haptic interface operates in the low voltage range.

The initial experiments with the haptic interface and the slave robot for laparoscopic and thoracoscopic surgery show that a multi DoF slave can be operated in an intuitive way. A weight compensation is successfully integrated via a feedforward signal on the  $\varphi$ ,  $\psi$  and  $z$  DoF. In the near future, a start will be made with the implementation of force feedback. User experience of surgeons and others is exploited to improve the haptic interface further. First of all, the forces can be reduced with approximately 50%. Second, a larger  $z$  range enhances the manipulation of the instrument in  $z$  direction. In the third place, a mechanical balancing will reduce the heat dissipation of the motors. It is also desirable to reduce the inertia and friction even further, the last especially for the  $z$  and  $\theta$  DoF. A higher bandwidth and improved haptic feedback will be the result. The shape of the button part can be optimized to provide a firmer hold. Chapter 6 discusses new actuation concepts to deal with these issues.



# Improvements for the haptic interface

---

**Abstract /** Alternative, parallel actuation concepts for the  $\varphi$ - $\psi$  and  $z$ - $\theta$  degrees of freedom improve the performance of the haptic interface. A parallel  $\varphi$ - $\psi$  actuation reduces the inertia, simplifies the cable layout and gives better thermal properties for the  $\psi$  motor. A combined  $z$ - $\theta$  actuation and suspension enlarges the  $z$  stroke of the stylus.

The initial experiments with the haptic interface and the slave robot for laparoscopic and thoracoscopic surgery show that it is feasible to operate a multi DoF slave in an intuitive way. As indicated in the previous chapter, there is room for improvement with respect to the inertia, weight compensation, force levels,  $z$  stroke and friction. This chapter discusses new actuation concepts for the  $\varphi$ - $\psi$  module and the  $z$ - $\theta$  module.

## 6.1 Actuation concepts

The kinematic chain of the haptic interface (chapter 5) is chosen accordingly to the instrument movements during surgery. This layout will be maintained for the second version of the haptic interface. Therefore, the same groups of DoFs can be distinguished:  $\varphi$ - $\psi$  for the lateral movements of the instrument tip,  $z$ - $\theta$  for the movements along the centerline of the instrument and a button to operate the instrument.

### 6.1.1 $\varphi$ and $\psi$ module

In the first design, the  $\psi$  motor is mounted to the  $\varphi$  motor shaft. The  $\psi$  motor is placed aside the  $\varphi$  rotation axis to leave enough room for the  $\theta$ - $z$  module. This design has some drawbacks. In the first place, the inertia in  $\varphi$  is increased proportionally with the motor mass times the distance between motor and  $\varphi$  axis to the square. Secondly, it requires balancing to prevent a continuous effort of the surgeon to keep the interface

in its nominal position. Furthermore, the motor and encoder wires for the  $\psi$  DoF move along with the  $\varphi$  rotation.

Improvements can be made by applying a modified serial layout, a parallel actuation concept with two single DoF actuators or a parallel actuation concept with a multi DoF spherical motor.

### $\psi$ motor on $\varphi$ rotation axis

A way to reduce the inertia and imbalance is to place the  $\psi$  motor on the centerline of the  $\varphi$  motor. This concept is drawn schematically in figure 6.1. The kinematic layout of this concept is identical to the first version of the haptic interface.

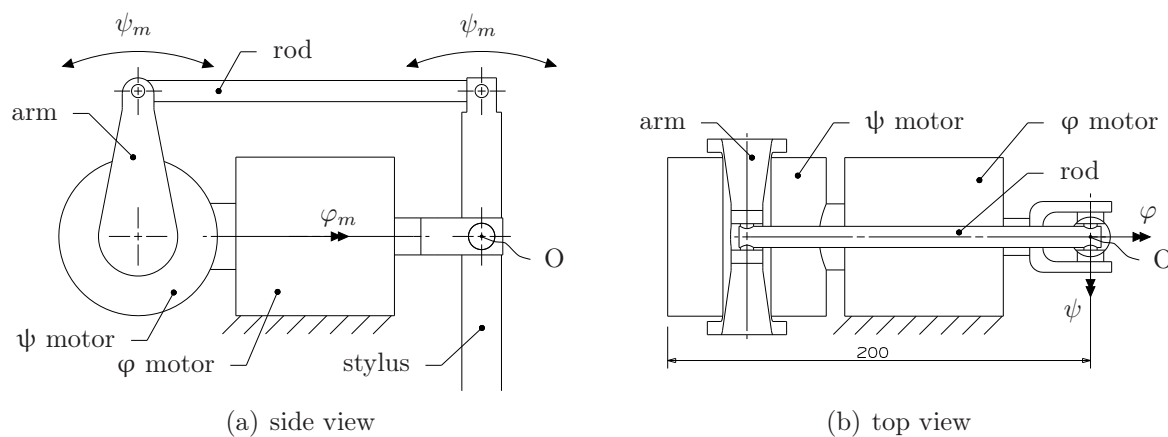


**Figure 6.1** / Serial actuation with the  $\psi$  motor on one line with the  $\varphi$  motor. A rod connects the stylus with the  $\psi$  motor to leave enough room for a  $\theta$ -z module. Point O indicates the rotation point of the stylus.

The  $\varphi$  motor is attached to the frame/coarse adjustment. The  $\psi$  motor is placed on the left side of the  $\varphi$  motor shaft and the stylus is attached to the right side of the shaft. The  $\psi$  motor as well as the stylus move along with a  $\varphi$  rotation. Actuation in  $\psi$  is done via the arm and the connecting rod. In this way, there is enough room for a  $\theta$ -z module. The inertia as felt at the tip is reduced according to the Steiner's parallel axis theorem with approximately 0.03 kg to 0.14 kg, assuming that no modifications are made with respect to the motors, the  $\theta$ -z module and the button. The maximal disturbance force as result of the unbalance is reduced to 0.9 N in  $\varphi$  direction. The total length of the  $\varphi$ - $\psi$  module is 200 mm (see figure 6.1(b)), approximately 70 mm longer than in the first design.

An alternative way to deal with the inertia and statical unbalance is by implementing a parallel actuation concept. In such layout, the two DC motors will be frame mounted

and stationary or replaced by a two or three DoF spherical motor. Additional advantages are that there is no need for a flexible cable connection between frame and  $\psi$  motor and that the heat of the motor(s) is conducted directly into the supporting frame.

### Spherical motors

A spherical motor must be placed in the virtual entry point O of the stylus, see figure 6.2. The working principle of this two DoF spherical motor is comparable with a brushless DC motor. It consists of a diametrically magnetized rotor and two sets of stator coils. One set is for the  $\varphi$  rotation and the other for the  $\psi$  rotation. A spherical motor can also have 3 DoFs. This requires a different stator winding layout and rotor magnetization pattern.

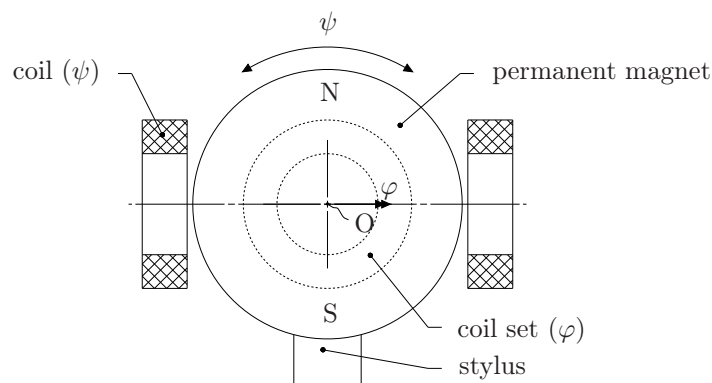


**Figure 6.2** / Parallel actuation via a 2 DoF spherical motor. The rotor and stylus are in the nominal position. The coils at the left and right side are for the  $\psi$  rotation, the coils at the front and back side (indicated by the dashed line) are for the  $\varphi$  rotation. The two rotations are about point O.

Multi DoF spherical motors with a working principle comparable to brushless DC motors are found in [93] and [98]. Table 6.1 gives an overview of the specifications of these motors.

Special attention has to be paid to the suspension of the rotor, as the stator has only a small opening around the motor shaft. In [93], a low friction surface coating between rotor and stator is chosen. An alternative is to build a cardanic suspension or a gimbal system around the motor itself. Due to the motor construction, there is only little room left for the the  $z$  (and  $\theta$ ) module, which is a drawback of this type of actuators.

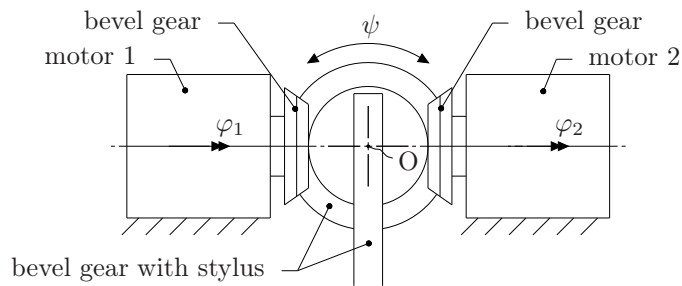
### Actuation via bevel gears

A parallel actuation with two frame mounted DC motors can be implemented via three bevel gears. A concept is visible in figure 6.3.

**Table 6.1** / Properties of the two and three DoF spherical motors.

	2 DoF [93]	3 DoF [93]	3 DoF [98]
peak torque [Nm]	0.4	0.6	4
continuous torque [Nm]	0.15	0.25	?
$\varphi$ and $\psi$ range [°]	$\pm 45$	$\pm 45$	$\pm 11^a$
$\theta$ range [°]	-	$> 360$	$> 360$
outer diameter rotor [mm]	48	62	93
outer diameter stator [mm]	88	120	225

a: can be increased up to about  $\pm 45^\circ$

**Figure 6.3** / Parallel actuation in  $\varphi$  and  $\psi$  via three bevel gears. The two motors are placed collinear and mounted to the frame.

The two motors are placed collinear with the  $\varphi$  axis. Each motor drives a bevel gear. The pen is mounted to the third bevel gear and rotates about point O. When the two motors have the same angular velocity, then the stylus will also rotate in  $\varphi$ . When one motor rotates in the opposite direction, then there will be a  $\psi$  rotation of the stylus. This means that the two DoFs are coupled. The range of motion is  $>180^\circ$  for  $\varphi$  and  $\pm 45^\circ$  for  $\psi$ .

It is advisable to apply spiral bevel gears. As multiple teeth are in contact simultaneously, the user will not feel the individual transitions between the teeth. This gives a better force feedback. The spiral bevel gear on the motor shaft is provided with an additional preloaded gearwheel to guarantee a backlash free operation. As the gears are situated directly around the pivot point O of the stylus, there is only little space left for the  $\theta$ -z module. Assembling of spiral gears is more critical than for example spur gears. For a smooth operation, it is important that the bevel gears are matched and that they are well aligned and mounted at the correct distance of the rotation point.

### Actuation via two rods

A parallel actuation via two rods as drawn in figure 6.4 gives more freedom around the pivot point.

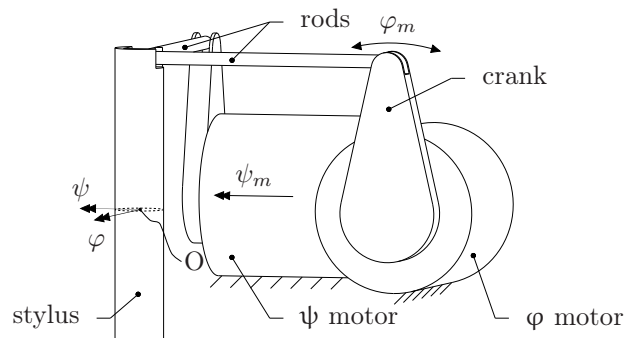


**Figure 6.4** /  $\varphi$  and  $\psi$  actuation via two rods. Suspension of the stylus in point O can be done with a cardan joint. A top view is visible in figure 6.5(a)

The stylus is supported in point O, for example with a cardan joint. The remaining two DoFs,  $\varphi$  and  $\psi$ , are actuated via two motors. These are placed sideways of the stylus and are mounted on the supporting frame. The rotation point O and the centerlines of the two motor shafts are in the same plane. Each motor is provided with a crank and drives the stylus via a rod. A ball joint at one side of the rod and a universal joint at the other side of the rod prevent that the mechanism is over-constrained. The two rods are connected to a central point at the top of the stylus, approximately 50 mm above the rotation point O.

The two rotations are not decoupled. A stylus rotation about for example the principal  $\psi$  axis requires also a rotation of the  $\psi$  motor to compensate for the sideways movement of the rod. This phenomenon is visible in figure 6.5: a principal stylus rotation of for example  $45^\circ$  in  $\psi$  is only possible when, in this particular case, a  $\varphi$  rotation of  $11^\circ$  is made as well. This value is determined via the motion package in NX and varies with the crank and rod length.

Due to the non linear system behavior, the mapping between the output torque of the two motors and the output torque of the stylus as felt by the user will vary over the workspace. The same is valid for the rotation of the motor shafts and the rotation of the stylus. As stated in the design specifications for haptic devices (section 4.2), it is desirable to have a uniform workspace as it gives a more efficient use of the actuators and encoders/sensors.

Different kinematic layouts for two and three DoF spherical mechanisms are proposed and analyzed in literature to achieve a more uniform input-output mapping. Examples can be found in [14, 30, 49, 50, 53, 77]. The proposed mechanisms differ strongly in the



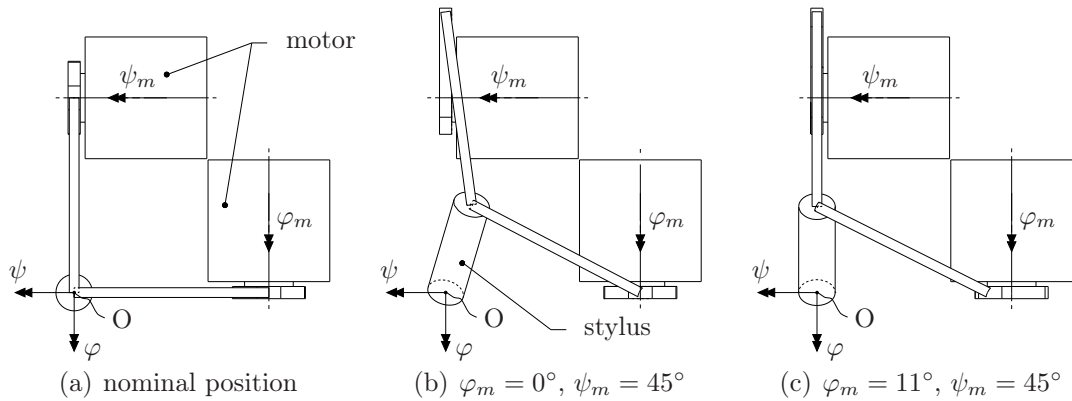


**Figure 6.5** / Top view of the parallel actuation via two rods. A compensation via the  $\varphi$  motor is required for a principal  $\psi$  rotation of the stylus (in this case  $\psi = 45^\circ$ ). Only the part of the stylus above the rotation point O is drawn.

number of the individual links and joints. The two DoF spherical mechanism in [49] has for example 8 links and 10 joints, two times more than the mechanism in [77] with only four links and five joints.

A low number of links and joints makes it easier to achieve a high stiffness and a low friction. It is worth mentioning that the stiffness also strongly depends on the geometry of the links. Only the mechanisms in [77] and [50] are investigated further. These two are drawn in respectively figure 6.6 and 6.7.

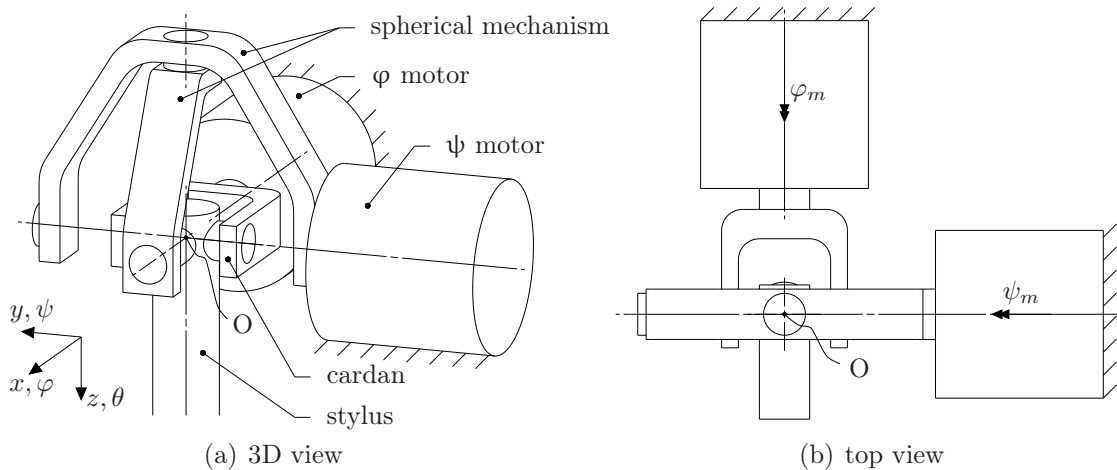


**Figure 6.6** / Parallel actuation via a cardan joint and a spherical mechanism. The spherical mechanism decouples the  $\psi$  rotation from the  $\varphi$  rotation.

A cardan joint and a spherical mechanism can be distinguished in the setup in figure 6.6.

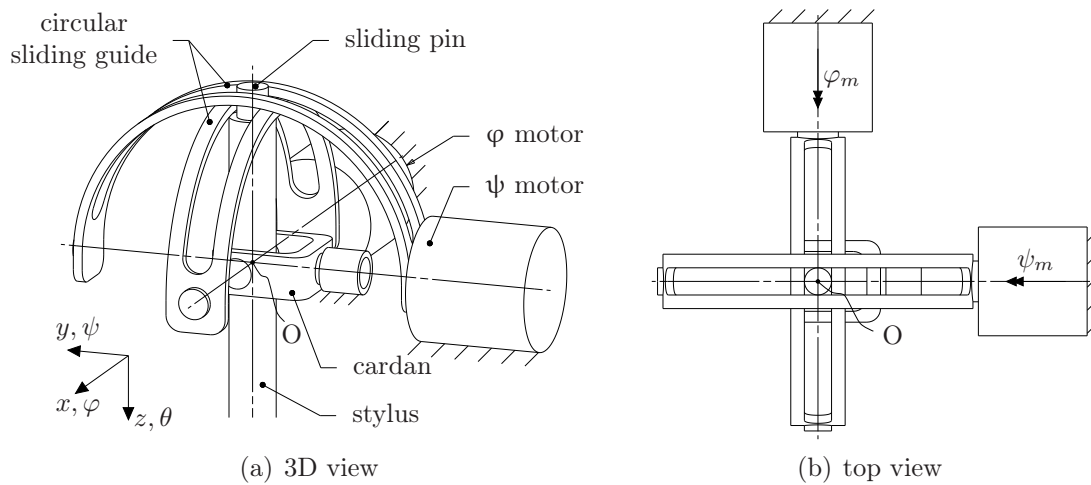


**Figure 6.7** / Parallel  $\varphi$  and  $\psi$  actuation via two circular sliding guides. The cardan is frame mounted and supports the stylus in the remaining four DoFs.

The first motor actuates the stylus in  $\varphi$  via the cardan joint and the second motor actuates the stylus in  $\psi$  via the spherical mechanism. The cardan joint constrains four DoFs:  $x$ ,  $y$ ,  $z$  and  $\theta$ . The spherical mechanism constrains three DoFs of the stylus:  $x$ ,  $y$  and  $z$ . This means that the entire mechanism is three times over-constrained.

The mechanism in figure 6.7 is intentionally meant as measuring system for a spherical motor. A stylus and a cardan joint are added. The cardan supports the stylus in  $x$ ,  $y$ ,  $z$  and  $\theta$ . Actuation in  $\varphi$  and  $\psi$  is done via the two circular sliding guides and the two motors. The guides and the motors are placed  $90^\circ$  apart. A sliding pin connects the stylus with the two guides. A slot in the  $\varphi$  guidance enables the stylus to rotate in  $\psi$  and vice versa. The two rotation axes and the rotation point  $O$  of the stylus are in the same plane.

The mechanism can be simplified if the  $\varphi$  or  $\psi$  actuation is combined with the cardanic suspension of the stylus itself, see figure 6.8. In this case, the  $\varphi$  motor drives and supports the stylus. The second motor performs the  $\psi$  actuation of the stylus via the circular guidance. This layout is more compact and has a reduced number of individual links and joints. The forward and backward kinematics are identical to the mechanism in figure 6.7.

The most critical part in this setup is the circular guidance with sliding pin as it can induce friction and/or backlash, even when it is replaced by a circular ball guidance. Furthermore, it is not very stiff and it restricts the free space around the stylus. An alternative is to use a parallelogram structure for the  $\psi$  actuation of the stylus.

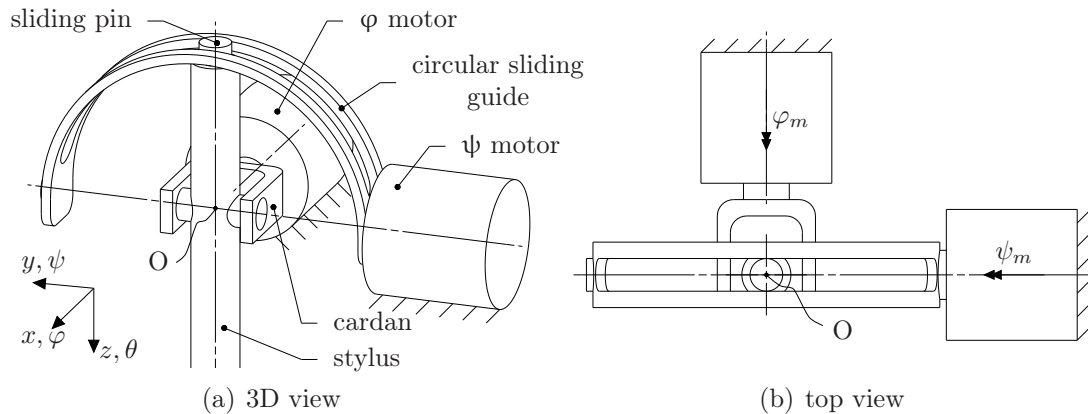


**Figure 6.8** / Parallel  $\varphi$  and  $\psi$  actuation via a cardan and one circular sliding guide. The cardan is mounted on the motor shaft.

### Bridge structure

The parallelogram structure in figure 6.9 replaces the circular guidance. It consists of three parts: a cardan, an arm and a bridge. The  $\psi$  motor drives the arm via the cardan. The bridge connects the arm with the stylus. A revolute joint is placed between arm and bridge. A ball joint forms the connection between bridge and stylus. There are no changes with respect to the suspension and  $\varphi$  actuation of the stylus. The mechanism has five links and six joints, two links and two joints more than the setup in figure 6.8. Therefore, it is important that the parallelogram has a low mass and high stiffness and that the pivot points have a minimum of friction.

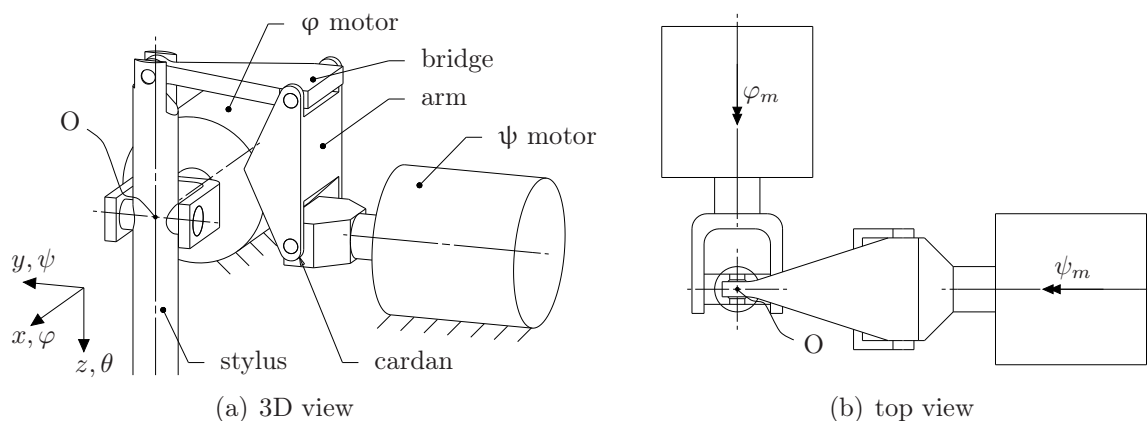


**Figure 6.9** / Parallel  $\varphi$  and  $\psi$  actuation via a cardan and a parallelogram. The  $\varphi$  motor supports the stylus.

Figure 6.10 gives a top and front view of the system for a combined  $\varphi$  and  $\psi$  rotation.

The two rotations are in this specific case:  $\varphi_m = \psi_m = 35.3^\circ$ . The corresponding angle between stylus and  $z$  axis is  $45^\circ$ . The angles  $\varphi_m$  and  $\psi_m$  are determined via the motion package in NX and verified with the kinematic model in appendix C.

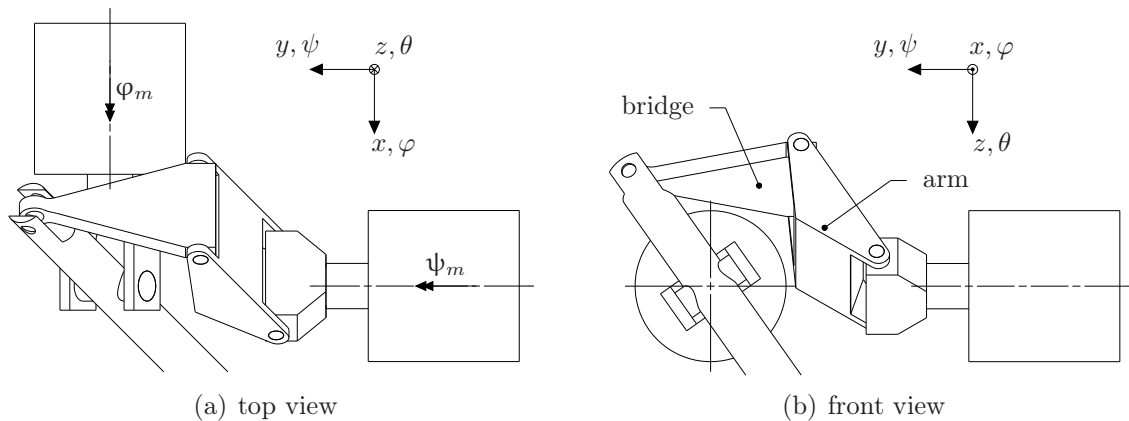


**Figure 6.10** / Combined  $\varphi$ - $\psi$  rotation of the parallelogram structure. With  $\varphi_m = \psi_m = 35.3^\circ$ , the stylus makes an angle of  $45^\circ$  with respect to the  $z$  axis.

The bridge must have a high bending stiffness in  $x$  direction. The requirements for the arm depend on the actual  $\varphi$  rotation. In the nominal position ( $\varphi_m = 0$ ), it must have a high torsional stiffness around the  $z$  axis and a high bending stiffness in  $x$  direction. For large  $\varphi$  rotations, the bending stiffness becomes more important than the torsional stiffness as the arm and bridge are more and more aligned. This means that the geometry of the arm must be optimized over the entire  $\varphi$  range. A high stiffness and a low moving mass can be achieved with thin wall, box shaped structures. The weight of the arm and bridge will be in the order of 25 g each. The contribution to the moving mass as felt by the surgeon is with  $\leq 4$  g neglectable. The different pivot points must be equipped with miniature ball bearings to minimize friction.

### Concept choice

Different concepts are proposed. The concept with the modified serial layout is feasible, but is relative large and still requires a flexible cable connection between frame and  $\psi$  motor. The two concepts with a spherical motor or with bevel gears are not practical as only little space is left for the  $z$ - $\theta$  module. This is not the case for the concepts as drawn in the figures 6.4-6.9. Here, the motors are placed sideways of the stylus. The actual actuation of the stylus is done via for example two rods or a cardan in combination with a parallelogram. Out of these five concepts, the last one with the parallelogram structure will be chosen. First of all, it has a more uniform workspace than the concept with the two rods. This gives a better use of the motor and encoder. Secondly, it is

more compact and has a higher stiffness than the concepts with a circular sliding guide. In the last place, it is not over-constrained, like the concept in figure 6.7 is.

Table 6.2 gives an estimation of the moving mass of the concept with parallelogram/bridge structure (figure 6.9), assumed that no further modifications are made to the haptic interface. The moving mass in  $\varphi$  is reduced with 35% and equals that of  $\psi$ . The maximal disturbance force in  $\varphi$  direction as result of the unbalance is reduced with 30% from 1.3 N to 0.9 N.

**Table 6.2** / Estimation of the moving mass in  $\varphi$  and  $\psi$  direction as felt by the surgeon, assuming that no modifications are made with respect the  $\theta$ -z module and the button part. The modified serial layout is listed for comparison. All values are obtained via NX.

	serial layout	modified serial layout	parallel with bridge
moving mass $\varphi$ [kg]	0.17	0.14	0.11
moving mass $\psi$ [kg]	0.11	0.11	0.11

### 6.1.2 z and $\theta$ module

The  $z$  and  $\theta$  range of motion of the haptic interface in chapter 5 is smaller than required for the instrument. Therefore, a jogging mode is implemented. Each range is divided in three regions, two for the velocity control (in positive and negative direction) and one for the positional control. The  $\theta$  range is with  $330^\circ$  sufficient large to implement the jogging mode. This is not the case for  $z$ . Due to the limited stroke of 16 mm, only 10-12 mm is left for this positional control. A larger  $z$  stroke is desirable, but can only be implemented in the current layout if the intermediate distance between the bearing bushes is reduced. With a  $z$  stroke of for example 32 mm, the spacing becomes 22 mm instead of 46 mm. This has a negative effect on the lateral stiffness of the stylus and therefore it is necessary to make a new design for the  $z$ - $\theta$  module. Besides a larger  $z$  stroke, it is also desirable to reduce the friction. This can be done by improving the suspension of the stylus. It must be possible to generate a force of 3 N and a torque of 40 mNm.

For the new version of the  $z$ - $\theta$  module, it is possible to maintain a parallel layout with two bearing bushes and two frame mounted motors, each decoupled in one DoF. The alternative is to combine the actuation with the suspension of the stylus itself to increase the  $z$  range even further.

### Voice coil/ motor

The concept design in figure 6.11 is based on a direct drive concept. Actuation of the two DoFs is done in a parallel way. The  $z$  range is 38 mm. The  $\theta$  range will be restricted to  $\approx 360^\circ$ .

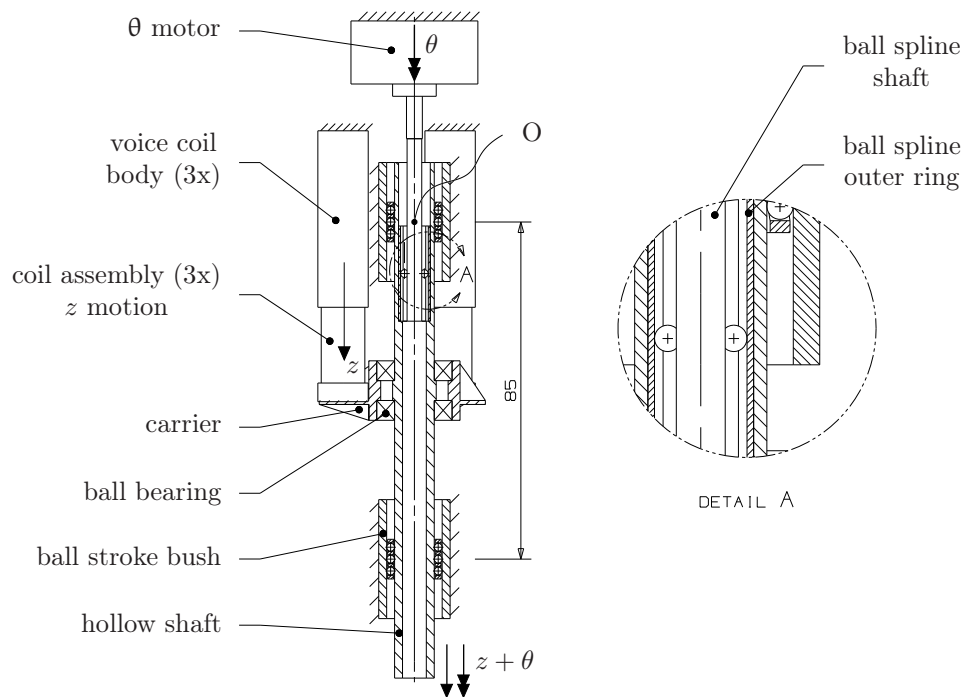


**Figure 6.11** / Concept for a parallel actuation of the  $z$  and  $\theta$  DoF via respectively voice coils and a DC motor. A fixed world symbol indicates that the component is fixed to a frame block (not drawn). Point O indicates the intersection point of the three rotation axes.

The handheld part of the interface is mounted at the lower end of the hollow shaft. Two ball stroke bushes or plain bearings guide this shaft with respect to a  $z$ - $\theta$  frame block, which is placed in series with the  $\varphi$ - $\psi$  module. The distance between the bearings is 85 mm. The motor is for the force feedback in  $\theta$ , the three voice coils for the feedback in  $z$  direction. All four actuators are mounted in the  $z$ - $\theta$  frame block. Point O indicates the intersection point of the  $\varphi$ ,  $\psi$  and  $\theta$  axis.

The  $z$  actuation is placed between the two ball stroke bushes to make a more efficient use of the available space and to enlarge the distance between the two bearing bushes of the hollow shaft. An increased lateral stiffness at the tip of the end effector is the result. The voice coils are placed under 3 times  $120^\circ$ . This gives a three times higher force level ( $F_{max}=6.6$  N,  $F_{cont}=2.1$  N) and a symmetric actuation about the centerline of the hollow shaft. The third voice coil is necessary as the output force decreases near

the end of stroke. Each voice coil consists of a body with a permanent magnet and a coil. The body is stationary and the coil assembly is via the carrier connected to the shaft. This layout minimizes the moving mass. As a consequence, the coil wires move along with the  $z$  motion. The number of wires is limited to two as a voice coil works without electronic commutation. In comparison, a brushless DC motor has three wires for the motor windings and five wires for the hall sensors.

The hollow shaft with the carrier guides the coil assemblies in five DoFs. Two ball bearings decouple the carrier in  $\theta$ . A simple guidance (for example a roller in a slot) is sufficient to suppress the remaining  $\theta$  DoF of the carrier itself and to maintain an air gap between the voice coil body and the coil assembly.

The  $\theta$  motor is placed concentrically with the hollow shaft. A 15 W, 32 mm flat Maxon motor with electrical commutation can be applied. This motor has a maximum torque of 84 mNm. A ball spline transmits the  $\theta$  rotation and decouples the  $z$  translation. The working principle is identical to the ball spline in the first version of the haptic interface (section 5.2.2), but now it is based on a commercially available product. The outer ring is placed in the hollow shaft, the shaft of the ball spline is connected to the motor shaft. To increase the stroke to approximately 40 mm, the ball cage of the ball spline is modified and the number of bearing balls is reduced. The lower torque rating of  $\approx 0.2$  Nm is not an issue, as it is still higher than the required 40 mNm.

### Spindle with two nuts

Figure 6.12 gives a concept for an alternative layout of the  $z$ - $\theta$  part. This type of actuator is applied in the FAMM robot [69]. The main parts are a spindle and two nuts. One part of the spindle has a left handed thread, the other part has a right handed thread. The two threads have the same pitch  $p$ . Each nut has three pairs of rollers and is actuated in  $\theta$ .

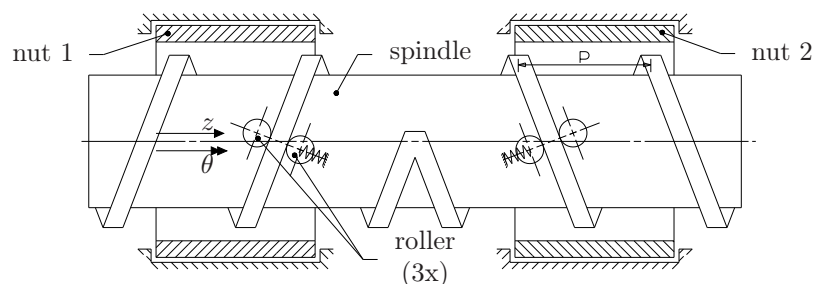


**Figure 6.12** / Two DoF actuator based on a spindle and two nuts. Each nut is driven in  $\theta$  by an electric motor. Depending on the angular velocity of both motors, the spindle rotates and/or translates along its centerline.

Actuation of the two nuts with an angular velocity  $\omega_{nut1}$  and  $\omega_{nut2}$ , results in one of

the following three possibilities:

1.  $\omega_{nut1} = \omega_{nut2}$ : spindle rotates in  $\theta$  with  $\omega_{spindle} = \omega_{nut1}$
2.  $\omega_{nut1} = -\omega_{nut2}$ : spindle moves in  $z$  direction with  $v_z = \frac{1}{2\pi} p \cdot \omega_{nut1}$  [m/s]
3.  $\omega_{nut1} \neq \omega_{nut2}$ : the spindle makes a combined  $\theta$  rotation and  $z$  movement with  $\omega_{spindle} = \frac{1}{2}(\omega_{nut1} + \omega_{nut2})$  and  $v_z = \frac{1}{2\pi} p \frac{1}{2}(\omega_{nut1} - \omega_{nut2})$

Besides the actuation, the nuts are also used to suspend the spindle in the remaining four DoFs. Therefore, no additional plain bearings or stroke bushes are required. The absence of these bearings and the absence of the components to decouple the  $z$  and  $\theta$  DoFs make that the two nuts can be placed well apart. This results in a high lateral stylus stiffness. The drawback of the spindle is that it is a relatively complex part, but it is also possible to use a friction wheel drive as drawn schematically in figure 6.13.

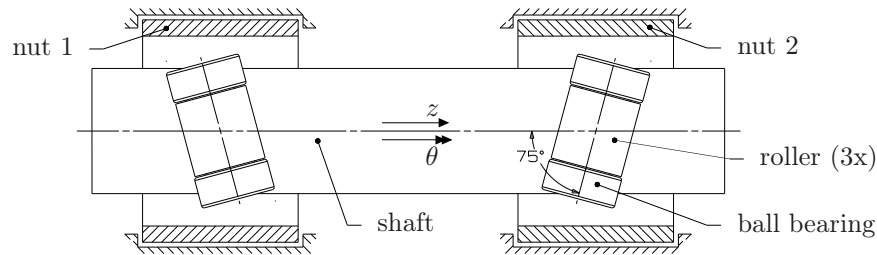


**Figure 6.13** / Two DoF actuator based on a friction wheel drive. Each nut is driven in  $\theta$  by an electric motor. The spindle rotates and/or translates along its centerline.

The spindle is replaced by a straight, ground shaft with an outer diameter of 10 mm. The rollers inside the nut are pressed against the shaft. Each nut has three rollers. The rollers are placed under an angle of  $3 \times 120^\circ$ . One nut has a left handed thread, the other nut has a right handed thread. Each roller is narrowed near the ends and supported in two miniature ball bearings. This minimizes the friction and reduces the required space. Axial play of the roller must be suppressed as it influences the  $z$  and  $\theta$  position of the shaft.

Figure 6.14 gives a concept layout for the friction wheel drive. The motor is a frameless, brushless DC motor and has no cogging. It measures  $\varnothing 38.1 \times 8.3$  mm. The inner diameter is 14 mm, so it leaves enough room for the shaft. The rotor and carrier are supported by two ball bearings. The continuous and maximum torque are 42 and 61 mNm. The inertia is  $J_{nut} = 6.5 \cdot 10^{-6}$  kgm<sup>2</sup>.

The inclination of the rollers with respect to the centerline of the shaft is set to  $75^\circ$  (see figure 6.13). This gives a pitch of  $p = 117$  mm and a transmission ratio of  $i = p/2\pi = 18.6 \cdot 10^{-3}$  m/rad. The force in  $z$  direction equals  $F_z = T_{motor}/i$ . With 42 and 61 mNm,



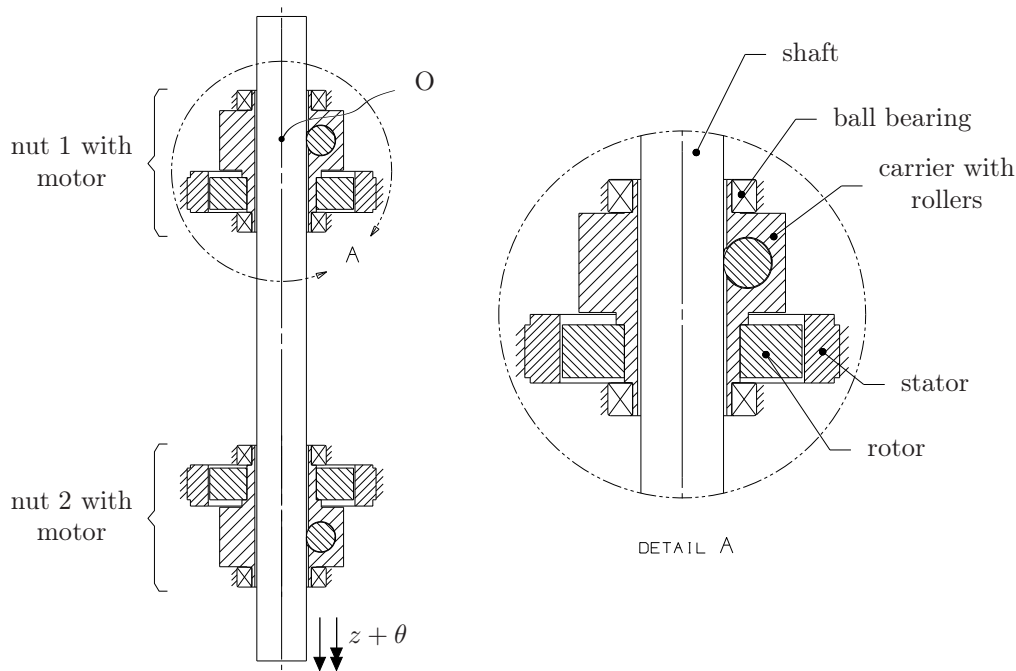


**Figure 6.14** / Concept for a parallel actuation via a friction wheel drive. A fixed world symbol indicates that the component is fixed to a frame block (not drawn). Point O indicates the intersection point of the three rotation axes.

the forces are  $F_{z,cont} = 2.2 \text{ N}$  and  $F_{z,max} = 3.3 \text{ N}$ . It is possible to enlarge this force, but as consequence the moving mass as felt in  $z$  direction will increase quadratically. Now, it is  $m_z = J_{nut}/i^2 = 19 \cdot 10^{-3} \text{ kg}$  per nut.

The radial preload force of each roller must be well defined to prevent slip between roller and shaft and to limit the Hertzian contact stress. Furthermore, it influences the friction, especially in  $z$  direction. A radial preload force of 40-50 N is sufficient. With three rollers, a friction coefficient of  $\mu = 0.1$  and a shaft radius of  $r_{shaft} = 5 \text{ mm}$ , each nut can transfer the maximum motor torque of 61 mNm.

The  $z$  range is 50 mm. The  $\theta$  rotation will be restricted on  $\approx 360^\circ$ . The translation and rotation of the shaft are measured by two optical encoders, one on each nut. This encoder information is also used for the sinusoidal commutation of the brushless DC motors. A resolution of  $0.3 \mu\text{m}$  ( $z$ ) and  $16 \mu\text{rad}$  ( $\theta$ ) can be achieved, if the same type of encoder is applied as in the single DoF linear setup. Additional reference marks on the shaft speed up the homing procedure and allow to detect creep between the rollers and shaft.

## Concept choice

Table 6.3 gives the estimated friction and moving mass/inertia for the preliminary version and the two new concepts for the  $z$ - $\theta$  actuation. For the moving mass and inertia, it is assumed that no modifications are made to the button part.

The last concept is preferable as it has a lower friction torque and a larger  $z$  stroke, this in spite of the higher inertia. The friction in  $z$  is only slightly reduced.

**Table 6.3** / Estimation of the friction and moving mass/inertia. The last two are determined via CAD models in NX.

	preliminary version	voice coil with DC motor	spindle-nut
$z$ stroke [mm]	16	38	50
moving mass $z$ [kg]	0.16	0.17	0.17
inertia $\theta$ [kgm <sup>2</sup> ]	$2.2 \cdot 10^{-5}$	$1.5 \cdot 10^{-5}$	$2.3 \cdot 10^{-5}$
friction force $z$ [N]	0.35-0.5	0.4	0.4
friction torque $\theta$ [mNm]	3-4.5	2.5	1.5

## 6.2 Concept layout

Figure 6.15 gives the concept layout of the haptic interface. It combines the parallelogram/bridge structure ( $\varphi$ - $\psi$ ) with the spindle-nut drive concept ( $z$ - $\theta$ ). The button part is identical to the button as discussed in section 5.2.3. The setup is drawn in its nominal position, only the button is slightly rotated for clarity.

Compared to figure 6.9, the  $\varphi$  and  $\psi$  drives are swapped to get some more free space around the surgeon's hand to make a rotation in  $\varphi$  direction. This does not affect the kinematics, as this mechanism has a symmetric workspace (see appendix C, equation (C.1), (C.2) and (C.5)). The  $z$ - $\theta$  module has a tube shaped housing in which the two nuts with the shaft (see figure 6.14) are placed. Suspension of the tube is done via the  $\psi$  motor. A labyrinth seal between the button part and the  $z$ - $\theta$  module protects the shaft against contamination. This is done to guarantee a smooth operation of the  $z$  and  $\theta$  DoF. The seal is constructed with two concentrically placed tubes and does not induce friction.

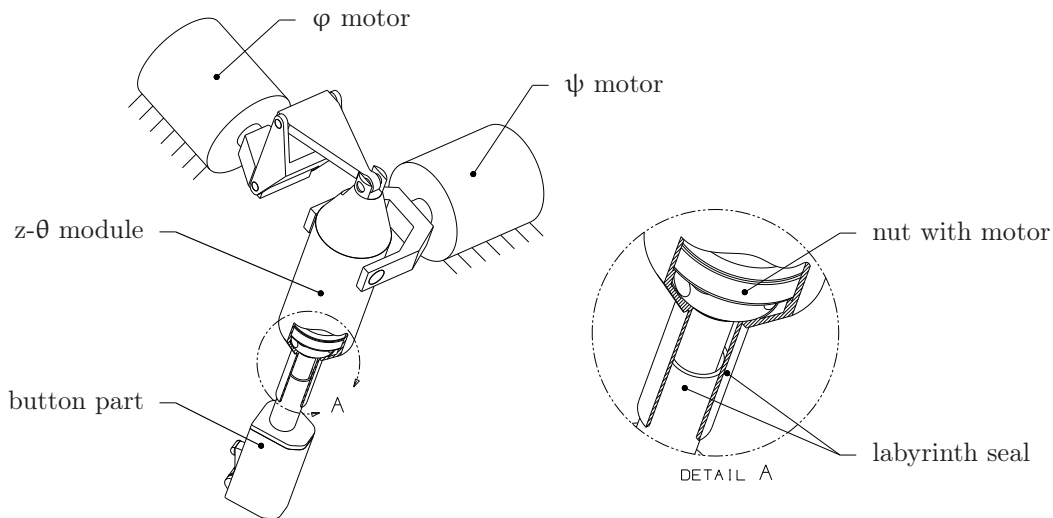


**Figure 6.15** / Concept layout of the haptic interface. It is based on the parallelogram/bridge structure and the spindle-nut drive concept.

### 6.3 Conclusions

The haptic interface as discussed in chapter 5 is feasible to control a slave device. This does not mean that it is not possible to make some improvements. The haptic interface has, for example, a limited  $z$  stroke and a relatively high inertia in  $\varphi$  direction. Different new design concepts are proposed for both the  $\varphi$ - $\psi$  and the  $z$ - $\theta$  module to deal with these issues. The kinematic chain of the five DoFs as applied in the first version of the haptic interface is almost unchanged, as it is the most practical one for eye surgery. The only difference is that the focus is now on a parallel  $\varphi$ - $\psi$  actuation instead of a serial one.

The most important advantages of a parallel layout are the absence of a flexible cable connection between frame and  $\psi$  motor, a reduced system inertia and the fact that the dissipated motor heat is transferred directly to the frame. Parallel layouts can be found with a large variety in the number of individual links and joints and with or without a uniform workspace. Here, a design that combines the suspension of the stylus with the  $\psi$  actuation is chosen. Actuation of the  $\varphi$  DoF is done via a parallelogram. The parallelogram decouples the  $\varphi$  motor in  $\psi$ . The design features a compact layout with a uniform workspace for an optimal use of the motor and encoder. It leaves enough free space for the  $z$ - $\theta$  module.

The spindle-nut concept for  $z$ - $\theta$  combines the actuation and suspension of the stylus. It has a  $z$  range of 50 mm, which is three times larger than the  $z$  stroke in the first design of the haptic interface. The friction torque in  $\theta$  is reduced with 40% to 1.5 mNm, the friction in  $z$  is almost unchanged with respect to the first design. The reason for this

---

difference is that the friction in  $z$  is mainly caused by the miniature ball bearings of the six preloaded rollers, while the  $\theta$  friction has its origin in the four ball bearings, which are responsible for the suspension of the two nuts. The estimated  $z$  friction is within the desired friction level of 0.15-0.42 N [20].



# Conclusions and recommendations

---

**Abstract /** In this chapter, the main conclusions of this thesis are summarized and recommendations for future work are presented.

## 7.1 Conclusions

A dedicated master-slave robotic system with force feedback for vitreo-retinal eye surgery will assist a surgeon during surgical tasks such as vitrectomy, membrane peeling and repair of a retinal detachment. In this thesis, the concept design of a master console and the realized haptic interfaces as part of this console are discussed. The master console is part of the EyeRhas (Eye Robot for Haptically Assisted Surgery) project.

The master console provides an ergonomic and intuitive working environment to the surgeon. It consists of a frame with armrest, a polarized 3D screen and two haptic interfaces with a coarse adjustment arm each. The console is mounted to the patient's headrest of the operating table and is combined with the slave. A table mounted device with screen is compact, easy to place and allows the surgeon to have a direct view on and a physical contact with the patient. Furthermore, the surgeon is not forced to work in a static body posture.

The surgeon uses the haptic interfaces to control the instruments. Each haptic interface has five degrees of freedom. These DoFs comply with the DoFs of the instrument inside the eye. The two interfaces are set in the correct pattern and orientation via the two coarse adjustments arms. Together with the visual feedback, it is as if the surgeon directly grasps the instrument near its tip, inside the eye. This provides an intuitive way of working. Mode switching enables to control three or more instrument manipulators with only two haptic interfaces.

Two single DoF master-slave setups are used to derive the requirements for the

mechanical design of the haptic interface, especially to find a suitable actuator for force feedback and to determine the necessary forces.

The first single DoF setup has a rotational degree of freedom with a range of  $\pm 45^\circ$  and a maximum force of 30 N. It consists of a master, a slave and an electronics cabinet. The master and slave device are fully identical. The combination of a backdriveable transmission, position measurement and force measurement makes it suitable for impedance, admittance and four channel haptic control. For the experiments, a position error (impedance) controller is used. The output force of the master and slave is the position error between the two devices times the servo stiffness.

The second, linear master device has a stroke of 80 mm and has no friction. A virtual environment acts as a slave. The setup is used to study the influence of simulated friction on positioning tasks.

The main results for the 5 DoF haptic interface are that a maximum/continuous force of 10/3 N is sufficient for the representation of the upscaled instrument forces and that it is possible to achieve force feedback without measuring any forces, as long as the device is backdriveable and the disturbance forces are low. This requires direct drive or a low geared transmission in combination with a brushless DC motor. Friction must stay below 0.4 N.

The haptic interface has four modules: a  $\varphi$  and a  $\psi$  part to manipulate an instrument in lateral direction, a  $z$ - $\theta$  module for the translation and rotation along the instrument axis and a button part to open and close a forceps. The four modules are placed in series. The  $\varphi$  part is suspended by the coarse adjustment arm. The surgeon manipulates the interface via the button part about a virtual entry point, which is the intersection point of the three rotation axes. This point is placed above the surgeon's wrist to provide a comfortable feeling during manipulation. Experiments in combination with a slave robot for laparoscopic and thoracoscopic surgery show that an instrument can be manipulated in an intuitive way.

These experiments also reveal that it is desirable to have a larger  $z$  stroke. Force feedback can be further improved if the inertia and friction are reduced, the last especially for the  $z$  and  $\theta$  DoFs.

A parallel actuation concept for  $\varphi$  and  $\psi$  reduces the inertia, eliminates the flexible cable connection between frame and  $\psi$  motor and allows the heat of the  $\psi$  motor to be transferred directly to the frame. A new concept layout is made where the suspension of the  $z$ - $\theta$  module and stylus is combined with the  $\psi$  actuation. Actuation of the  $\varphi$  DoF is done via a parallelogram. The design has a compact layout with a uniform workspace and leaves enough space for a  $z$ - $\theta$  module. The  $z$ - $\theta$  module is based on a spindle-nut concept. It combines the actuation and suspension of the stylus. The  $z$  stroke is three times larger than in the first design of the haptic interface.

In summary, two single DoF experimental setups and two (left and right) five DoF haptic interfaces are realized. The interface fits in the design of a master console for robotically assisted vitreo-retinal eye surgery.

## 7.2 Recommendations

The first tests have been done with a slave robot for laparoscopic and thoracoscopic surgery in combination with position control. A start is made with the evaluation of the haptic feedback interface. User experience of surgeons and that of others must be utilized to test this version and a forthcoming version of the haptic interface further. In combination with a 3D screen it is possible to test the ergonomics of the master console. Features such as additional scaling and mode switching between different instruments can be implemented in the control software.

The instrument manipulator for vitreo-retinal eye surgery is expected to become available in the third quarter of 2011. Feasibility studies can be performed with the haptic interface and instrument manipulator. These studies must include vitrectomy and membrane peeling and can be done on a phantom eye or porcine eye. Additionally, a study on intraocular cannulation can be performed. It is (almost) not possible to do this by hand as it requires an accuracy in the order of 10  $\mu\text{m}$ . Parallel, a further system integration of the master with slave can be made and the frame with coarse adjustment arms can be realized.

For the second version of the haptic interface, it is worthwhile to investigate the possibility to place a three channel amplifier and acquisition print on the  $z$ - $\theta$  module for the  $z$ ,  $\theta$  and *button* DoF. This will reduce the number of wires drastically, as only a maximum of 8 wires is required (power supply and communication bus) instead of the 38 wires in the current layout. The reduction in wires makes the electrical connection more reliable and easier to install. The same acquisition and amplifier print can be used for  $\varphi$  and  $\psi$ . Furthermore, the shape of the button part can be optimized for a firmer grip with less effort. Mechanical balancing of the stylus reduces the dissipation of the motors and allows for smaller motors, leading to a design with less inertia. The proposed improvements motivate the realization of this second version of the haptic interface.

It is to be expected that the master-slave system for vitreo-retinal eye surgery is beneficial for both the surgeon and the patient by allowing more precise surgery in a more ergonomic environment for the surgeon. It contributes to a reduction in surgery time. The compact layout makes that the system easily fits in the current operating room arrangement. As with all new technologies, it is likely that it will lead to new surgical approaches which are not possible with manually performed surgery.





## APPENDIX A

# Principal planes in human anatomy

---

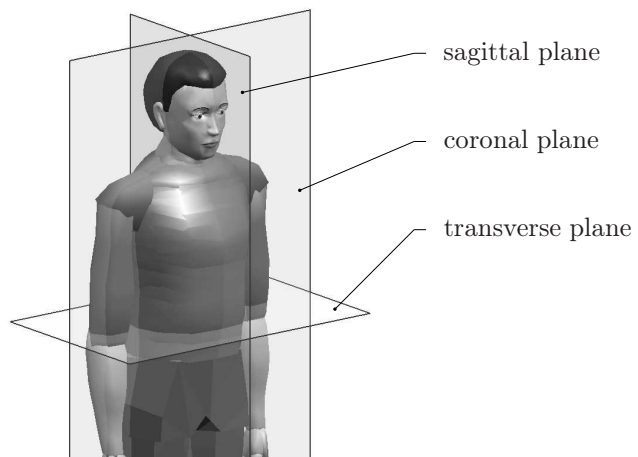


Figure A.1 / Principal planes used in human anatomy.



# Identification of the haptic interface

---

This appendix gives the Bode plots of the  $\psi$ ,  $\theta$  and  $z$  DoFs for a frequency up to 200 Hz. All three DoFs are identified with the stylus moving in a horizontal plane. The measurements are made on the right haptic interface.

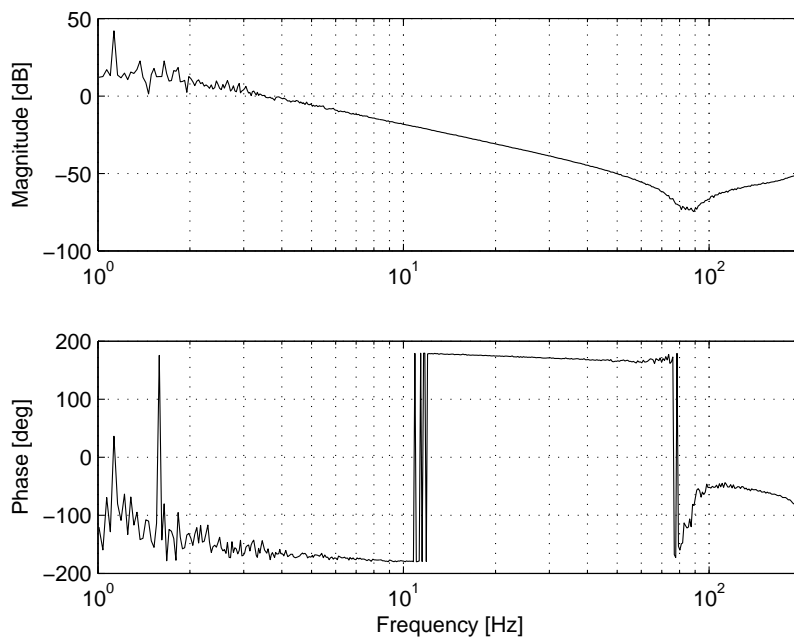


**Figure B.1** / Bode plot of the  $\psi$  DoF.

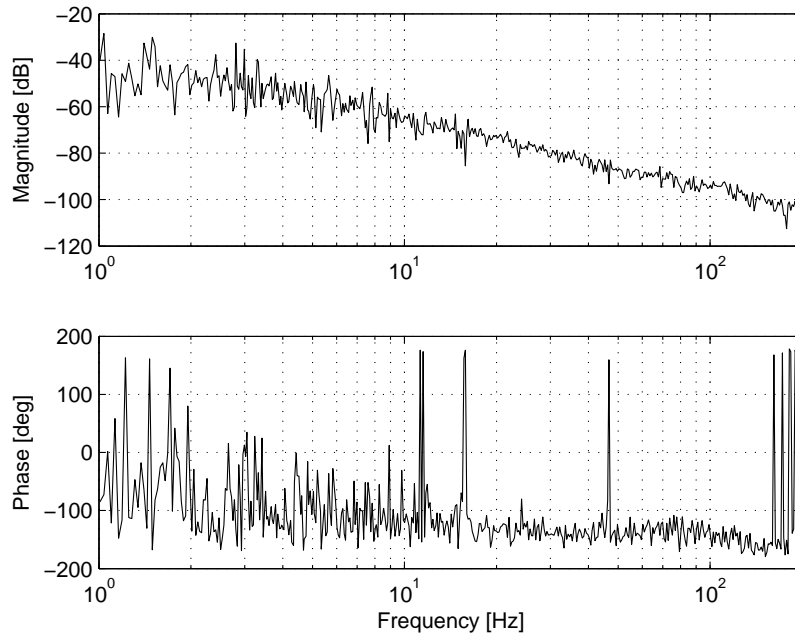


Figure B.2 / Bode plot of the  $z$  DoF.

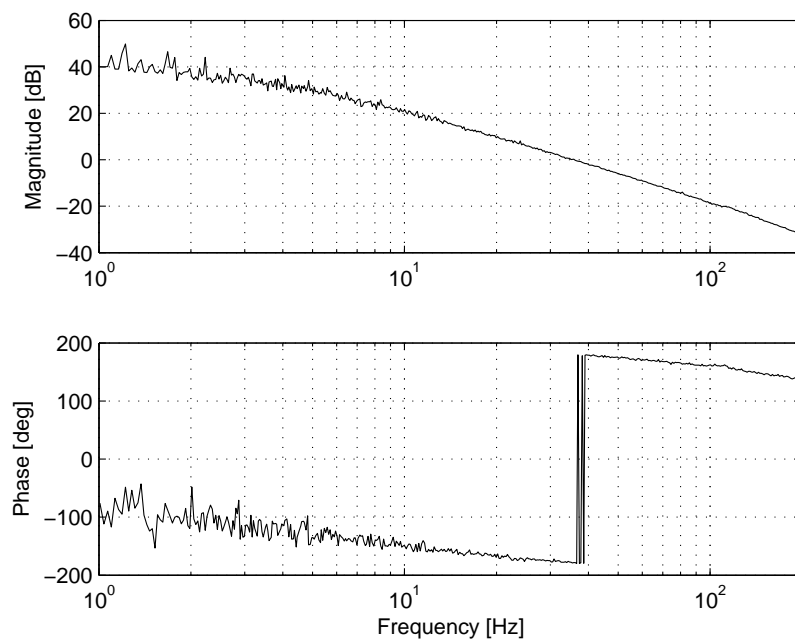
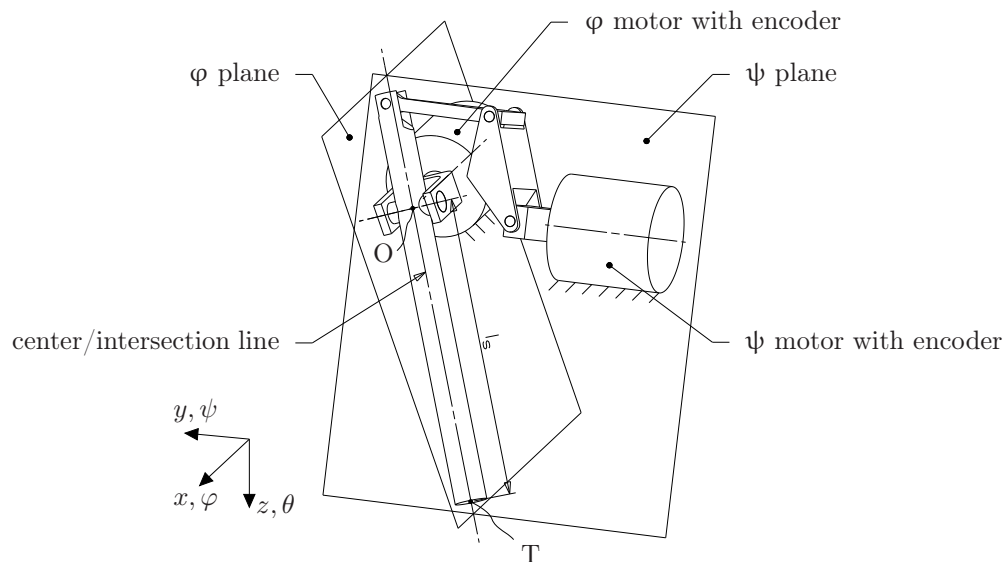


Figure B.3 / Bode plot of the  $\theta$  DoF.

## Kinematics of the bridge structure

The position of the stylus tip can be derived by use of two auxiliary planes, see figure C.1 and figure C.2. Point O is the rotation point of the stylus. Point T represents the tip of the stylus. The length of the stylus is  $l_s$ . The two motors are equipped with an encoder to measure the  $\varphi$  and  $\psi$  rotation. The centerline of the stylus complies to the intersection line of the  $\varphi$  and  $\psi$  plane.



**Figure C.1** / Combined  $\varphi$ - $\psi$  rotation of the stylus. The position of the tip (point T) can be calculated by use of two auxiliary planes and the stylus length  $l_s$ .

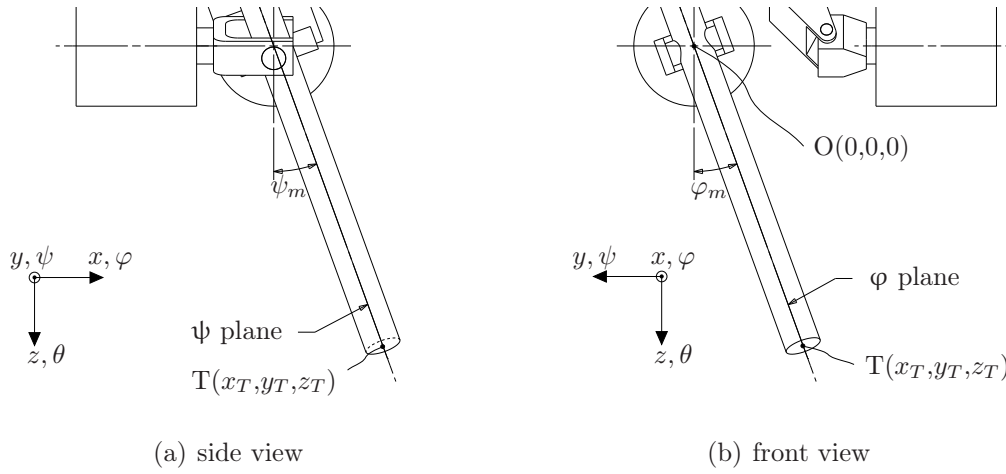


**Figure C.2** / Principal views along the  $-y$  and  $-x$  axes for the stylus orientation as drawn in figure C.1.

The two planes are described by:

$$\tan(\varphi_m) = \frac{-y_T}{z_T} \quad (\text{C.1})$$

$$\tan(\psi_m) = \frac{x_T}{z_T} \quad (\text{C.2})$$

Furthermore, the  $x$ ,  $y$ , and  $z$  coordinates of the tip (point T) comply to:

$$l_s^2 = x_T^2 + y_T^2 + z_T^2 \quad (\text{C.3})$$

Substitution of equation (C.1) and (C.2) in (C.3) gives:

$$l_s^2 = z_T^2(\tan^2(\varphi) + \tan^2(\psi) + 1) \quad (\text{C.4})$$

$$\Rightarrow z_T = \sqrt{\frac{l_s^2}{\tan^2(\varphi) + \tan^2(\psi) + 1}} \quad (\text{C.5})$$

Subsequently,  $x_T$  and  $y_T$  are calculated by substitution of  $z_T$  in equation (C.1) and (C.2).

# Bibliography

---

- [1] J. An and D.-S. Kwon. Haptic experimentation on a hybrid active/passive force feedback device. *IEEE International Conference on Robotics and Automation (ICRA)*, (4):4217 – 4222, 2002.
- [2] Analog Devices, Inc. Universal LVDT signal conditioner ad698, 1995.
- [3] W. T. Ang, C. N. Riviere and P. K. Khosla. An active hand-held instrument for enhanced microsurgical accuracy. *MICCAI*, pages 878 – 886, 2000.
- [4] D. A. Atchison and G. Smith. *Optics of the human eye*. Butterworth Heinemann, 2000, ISBN 0750637757.
- [5] R. Baumann and R. Clavel. Haptic interface for virtual reality based minimally invasive surgery simulation. *IEEE International Conference on Robotics and Automation (ICRA)*, 1:381 – 386, 1998.
- [6] R. Baumann, W. Maeder, D. Glauser and R. Clavel. The pantoscope: a spherical remote-center-of-motion parallel manipulator for force reflection. *IEEE International Conference on Robotics and Automation (ICRA)*, 1:718 – 723, 1997.
- [7] L. J. M. van den Bedem. *Realization of a demonstrator slave for robotic minimally invasive surgery*. PhD thesis, Technische Universiteit Eindhoven, 2010, ISBN 9789038623009.
- [8] L. J. M. van den Bedem, R. Hendrix, P. C. J. N. Rosielle, M. Steinbuch and H. Nijmeijer. Design of a minimally invasive surgical teleoperated master-slave system with haptic feedback. *IEEE International Conference on Mechatronics and Automation (ICMA)*, pages 60 – 65, 2009.
- [9] M. N. de Beukelaar. Wrijvingsidentificatie van een 1 dof systeem, DCT 2008.105, TU/e, 2008, in Dutch.
- [10] S. J. Bolanowski Jr., G. A. Gescheider, R. T. Verrillo and C. M. Checkosky. Four channels mediate the mechanical aspects of touch. *Journal of the Acoustical Society of America*, 84(5):1680 – 1694, 1988.
- [11] D. H. Bourla, J. Hubschman, M. Culjat, A. Tsirbas, A. Gupta and S. D. Schwartz. Feasibility study of intraocular robotic surgery with the da vinci surgical system. *Retina*, 28(1):154 – 158, 2008.
- [12] C. M. Brooks. Telerobotic response requirements. *IEEE International Conference on Systems, Man and Cybernetics*, pages 113 – 120, 1990.
- [13] G. C. Burdea. *Force and touch feedback for virtual reality*. John Wiley & Sons, Inc., 1996, ISBN 0471021415.
- [14] M. Carricato and V. Parenti-Castelli. A novel fully decoupled two-degrees-of-freedom parallel wrist. *The International Journal of Robotics Research*, 23(6):661 – 667, 2004.



- [15] M. W. Charles and N. Brown. Dimensions of the human eye relevant to radiation protection. *Physics in Medicine and Biology*, 20(2):202 – 218, 1975.
- [16] S. Charles, H. Das, T. Ohm, C. Boswell, G. Rodriguez, R. Steele and D. Istrate. Dexterity-enhanced telerobotic microsurgery. *IEEE International Conference on Advanced Robotics (ICAR)*, pages 5 – 10, 1997.
- [17] G. A. V. Christiansson. *Hard master soft slave haptic teleoperation*. PhD thesis, Technische Universiteit Delft, 2007, ISBN 9789085593072.
- [18] A. P. Ciardella, Y. L. Fisher, C. Carvalho, J. S. Slakter, R. G. Bryan, J. A. Sorenson, R. F. Spaide, K. B. Freund, D. R. Guyer and L. A. Yannuzzi. Endoscopic vitreoretinal surgery for complicated proliferative diabetic retinopathy. *Retina*, 21(1):20 – 27, 2001.
- [19] K. J. Crommentuijn. *User centered guidelines for designing (surgical-) teleoperation systems*. PhD thesis, Technische Universiteit Eindhoven, 2011, to be published.
- [20] K. J. Crommentuijn and D. J. Hermes. The effect of coulomb friction in a haptic interface on positioning performance. *Eurohaptics*, 2010.
- [21] H. Das, H. Zak, J. Johnson, J. Crouch and D. Frambach. Evaluation of a telerobotic system to assist surgeons in microsurgery. *Computer Aided Surgery*, 4(1):15 – 25, 1999.
- [22] N. A. Dodgson. Autostereoscopic 3D displays. *Computer*, 38(8):31 – 36, 2005.
- [23] dSPACE, Jan. 2010. <http://www.dspace.de>.
- [24] C. Eckardt. Transconjunctival suturless 23-gauge vitrectomy. *VitroTech Online, DORC International B. V.*, 9(1):32 – 50, 2006. <http://www.dorc.nl/vitreotech>.
- [25] F. Faude and P. Wiedemann. Vitreoretinal endoscope for the assessment of the peripheral retina and the ciliary body after large retinectomies in severe anterior pvr. *International Ophthalmology*, 25(1):53 – 56, 2004.
- [26] P. Fischer, R. Daniel and K. V. Siva. Specification and design of input devices for teleoperation. *IEEE International Conference on Robotics and Automation (ICRA)*, 1:540–545, 1990.
- [27] Force Dimension. Delta haptic device, 6-DoF force feedback interface, Datasheet, 2004.
- [28] E. C. Fritz, G. A. V. Christiansson and R. Q. van der Linde. Haptic gripper with adjustable inherent passive properties. *Eurohaptics*, pages 324 – 329, 2004.
- [29] Futek, Apr. 2010. <http://www.futek.com>.
- [30] C. M. Gosselin and F. Caron. Two degree-of-freedom spherical orienting device. *United States Patent No. 5966991*, 1999.
- [31] J. H. Grasman. Mechanical design and construction of a 5 dof haptic master device for an eye-surgery robot, DCT 2008.111, TU/e, 2008.
- [32] B. Hannaford. A design framework for teleoperators with kinesthetic feedback. *IEEE Transactions on Robotics and Automation*, 5(4):426 – 434, 1989.
- [33] B. Hannaford. Experimental measurements for specification of surgical mechanisms and understanding of surgical skill. *Lecture Notes of the European Summer School on Surgical Robotics*, 2003.
- [34] Haption S.A. Haptic device Virtuose™ 6D35-45, technical specification, Datasheet, 2005.
- [35] Haption S.A. Virtuose™ 6D Desktop, Datasheet, 2007.
- [36] V. Hayward. Toward a seven axis haptic device. *IEEE/RSJ International Conference on Intelligent Robots and Systems (IROS)*, 3:133 – 139, 1995.

- [37] R. Hendrix, P. C. J. N. Rosielle and H. Nijmeijer. Design of a haptic master interface for robotically assisted vitreo-retinal eye surgery. *IEEE International Conference on Advanced Robotics (ICAR)*, pages 1 – 6, 2009.
- [38] R. Hendrix, P. C. J. N. Rosielle, H. Nijmeijer and M. D. de Smet. Design of a master device to perform robotically assisted vitreo-retinal eye surgery. *International Conference of Society for Medical Innovation and Technology (SMIT)*, page 53, 2009.
- [39] N. S. Holliman. 3D display systems. Technical report, 2005.
- [40] Intuitive Surgical, Inc., May 2010. <http://www.intuitivesurgical.com>.
- [41] Kaman. Application handbook noncontact position sensors, 1999.
- [42] M. Kilchenman and M. Goldfarb. Force saturation, system bandwidth, information transfer and surface quality in haptic interfaces. *IEEE International Conference on Robotics and Automation (ICRA)*, pages 1382 – 1387, 2001.
- [43] Y. Kurita, R. Kempf, Y. Iida, J. Okude, M. Kaneko, H. K. Mishima, H. Tsukamoto, E. Sugimoto, S. Katakura, K. Kobayashi and Y. Kiuchi. Contact-based stiffness sensing of human eye. *IEEE Transactions on Biomedical Engineering*, 55(2):739 – 745, feb 2008.
- [44] D.-S. Kwon, K. Y. Woo and H. S. Cho. Haptic control of the master hand controller for a microsurgical telerobot system. *IEEE International Conference on Robotics and Automation (ICRA)*, 3:1722 – 1727, 1999.
- [45] D.-S. Kwon, K. Y. Woo, S. K. Song, W. S. Kim and H. S. Cho. Microsurgical telerobot system. *IEEE/RSJ International Conference on Intelligent Robots and Systems (IROS)*, 2:945 – 950, 1998.
- [46] W. T. Latt, U.-X. Tan, C. Y. Shee and W. T. Ang. A compact hand-held active physiological tremor compensation instrument. *IEEE/ASME International Conference on Advanced Intelligent Mechatronics*, pages 711 – 716, 2009.
- [47] D. A. Lawrence. Stability and transparency in bilateral teleoperation. *IEEE Transactions on Robotics and Automation*, 9(5):624 – 637, 1993.
- [48] L. van Leeuwen. Haptische pen met 4 vrijheidsgraden, LIS, 2008, in Dutch.
- [49] W. Li, J. Sun, J. Zhang, K. He and R. Du. A novel parallel 2-dof spherical mechanism with one-to-one input-output mapping. *WSEAS International Conference on Robotics, Control and Manufacturing Technology*, pages 6 – 11, 2006.
- [50] Z. Li, Q. Wang, X. Bao and K. Xia. Motion control algorithm and kinematic analysis of a spherical stepper motor. *International Conference on Electrical Machines and Systems (ICEMS)*, 2:1659 – 1664, 2005.
- [51] R. Q. van der Linde and P. Lammertse. Hapticmaster - a generic force controlled robot for human interaction. *Industrial Robot*, 2003.
- [52] Maquet GmbH & Co. KG. Mobile operating table alphastar, 2005.
- [53] F. Marco, F. Antonio, S. Fabio and B. Massimo. Kinematics of a new 2-dof wrist with high angulation capability. *IEEE International Conference on Robotics and Automation (ICRA)*, pages 1524 – 1529, 2006.
- [54] Maxon motor. Technical training, 2007.
- [55] Maxon motor. High precision drives and systems, 2009/2010.
- [56] D. F. McAllister. *Encyclopedia of imaging science and technology*, chapter Display technology: stereo & 3D display technologies, pages 1327 – 1344. John Wiley & Sons, Inc., 2002, ISBN 9780471332763.

- [57] H. C. M. Meenink, R. Hendrix, P. C. J. N. Rosielle, M. Steinbuch, H. Nijmeijer and M. D. de Smet. A master-slave robot for vitreo-retinal eye surgery. *Proceedings of the 10th International Conference of the European Society for Precision Engineering & Nanotechnology (EUSPEN)*, 2:408 – 411, 2010.
- [58] H. C. M. Meenink, P. C. J. N. Rosielle, M. Steinbuch and M. D. de Smet. Instrument manipulator for a master-slave robot for vitreo-retinal ophthalmic surgery. *International Conference of Society for Medical Innovation and Technology (SMIT)*, page 53, 2009.
- [59] H. C. M. Meenink, P. C. J. N. Rosielle, M. Steinbuch and M. D. de Smet. A slave robot for vitreo-retinal ophthalmic surgery. *International Conference of Society for Medical Innovation and Technology (SMIT)*, 2010.
- [60] P. A. Millman and J. E. Colgate. Design of a four degree-of-freedom force-reflecting manipulandum with a specified force/torque workspace. *IEEE International Conference on Robotics and Automation (ICRA)*, pages 1488 – 1493, 1991.
- [61] J. F. M. Molenbroek. Dined tabel, 2004.
- [62] MPB Technologies, Inc. Freedom 6S force feedback hand controller, Datasheet, 2006.
- [63] A. P. Mulgaonkar, J. Hubschman, J. Bourges, B. Jordan, C. Cham, J. T. Wilson, T. Tsao and M. O. Culjat. A prototype surgical manipulator for robotic intraocular micro surgery. *Studies in health technology and informatics*, 142:215 – 217, 2009.
- [64] T. Nakano, N. Sugita, T. Ueta, Y. Tamaki and M. Mitsuishi. A parallel robot to assist vitreoretinal surgery. *International Journal of Computer Assisted Radiology and Surgery*, 4(6):517 – 526, 2009.
- [65] G. Niemeyer, C. Preusche and G. Hirzinger. *Springer Handbook of Robotics*, chapter 31, Telerobotics, pages 741 – 757. Springer Berlin Heidelberg, 2008, ISBN 9783540239574.
- [66] X. D. Pang, H. Z. Tan and I. Durlach. Manual discrimination of force using active finger motion. *Perception & Psychophysics*, 49(6):531 – 540, 1991.
- [67] E. Papadopoulos, K. Vlachos and D. Mitropoulos. Design of a 5-dof haptic simulator for urological operations. *IEEE International Conference on Robotics and Automation (ICRA)*, 2:2079 – 2048, 2002.
- [68] S. Pastoor and M. Wöpking. 3-D displays: A review of current technologies. *Displays*, 17(2):100 – 110, 1997.
- [69] Philips Centre for Manufacturing Technology. FAMM: fast and accurate manipulator modules, Datasheet, 1989.
- [70] P. W. Poels. Design of the frame and arms of a master for robotic surgery, DCT 2007.090, TU/e, 2007.
- [71] B. R. Prashant, A. P. Rowley, R. N. Khurana, C. M. Deboer, R. M. Kerns, L. P. Chong and M. S. Humayun. Evaluation of a stereoscopic camera-based three-dimensional viewing workstation for ophthalmic surgery. *American Journal of Ophthalmology*, 143(5):891 – 892, 2007.
- [72] Quanser, Inc. 5-DoF Haptic Wand, Datasheet, 2008.
- [73] C. N. Riviere, W. T. Ang and P. K. Khosla. Toward active tremor canceling in handheld microsurgical instruments. *IEEE Transactions on Robotics and Automation*, 19(5):793 – 800, 2003.
- [74] C. N. Riviere, R. S. Rader and P. K. Khosla. Characteristics of hand motion of eye surgeons. *IEEE Engineering in Medicine and Biology Society*, pages 1690 – 1693, 1997.
- [75] P. C. J. N. Rosielle and E. A. G. Reker. Constructieprincipes 1 - bedoeld voor het nauwkeurig bewegen en positioneren, Lecture notes 4007 (in Dutch), TU/e, 2000.

- [76] R. B. Rusu, W. Meeussen, S. Chitta and M. Beetz. Laser-based perception for door and handle identification. *IEEE International Conference on Advanced Robotics (ICAR)*, pages 1 – 8, 2009.
- [77] E. Samson, D. Laurendeau, M. Parizeau, S. Comtois, J.-F. Allan and C. Gosselin. The agile stereo pair for active vision. *Machine Vision and Applications*, 17(1):32 – 50, 2006.
- [78] J. Scholtes. Control of a 1-dof haptics system, DCT 2007.108, TU/e, 2007.
- [79] J. Scholtes. Analysis of a haptic control architecture, DCT 2009.056, TU/e, 2009.
- [80] Sensable Technologies, Inc. Specifications comparison for the Phantom<sup>®</sup> Premium 1.5/6DoF & 1.5 high force/6DoF haptic devices, Datasheet, 2006.
- [81] Sensable Technologies, Inc. Specifications for the Phantom<sup>®</sup> Premium 3.0/6DoF haptic device, Datasheet, 2006.
- [82] Senternovem/Agentschap NL, Dec. 2010. <http://www.senternovem.nl/iopmensmachine-interactie>.
- [83] M. D. de Smet and M. Mura. Minimally invasive surgery - endoscopic retinal detachment repair in patients with media opacities. *Eye*, 22:662 – 665, 2008.
- [84] W. E. Smiddy, R. G. Michels and W. R. Green. Lens and peripheral retinal relationships during vitrectomy. *Retina*, 11(2):199 – 203, 1991.
- [85] L. J. Stocco, S. E. Salcudean and F. Sassani. Optimal kinematic design of a haptic pen. *IEEE/ASME Transactions on Mechatronics*, 6(3):210–220, 2001.
- [86] H. Takahashi, T. Yonemura, N. Sugita, M. Mitsuishi, S. Sora, A. Morita and R. Mochizuki. Master manipulator with higher operability designed for micro neuro surgical system. *IEEE International Conference on Robotics and Automation (ICRA)*, pages 3902–3907, 2008.
- [87] H. Z. Tan, M. A. Srinivasan, B. Eberman and B. Cheng. Human factors for the design of force-reflecting haptic interfaces. *ASME Conference on Dynamics Systems and Control*, 1994.
- [88] W. M. Tang and D. P. Han. A study of surgical approaches to retinal vascular occlusions. *Arch Ophthalmol*, 118:138 – 143, 2000.
- [89] R. Taylor, P. Jensen, L. Whitcomb, A. Barnes, R. Kumar, D. Stoianovici, P. Gupta, Z. Wang, E. Dejuan and L. Kavoussi. A steady-hand robotic system for microsurgical augmentation. *The International Journal of Robotics Research*, 18(12):1201 – 1210, 1999.
- [90] A. R. Tilley. *The measure of man and woman: human factors in design*. John Wiley & Sons, Inc., 2002, ISBN 0471099554.
- [91] TUeDACS, Jan. 2010. <http://www.tuedacs.nl>.
- [92] T. Ueta, Y. Yamaguchi, Y. Shirakawa, T. Nakano, R. Ideta, Y. Noda, A. Morita, R. Mochizuki, N. Sugita, M. Mitsuishi and Y. Tamaki. Robot-assisted vitreoretinal surgery: development of a prototype and feasibility studies in an animal model. *Ophthalmology*, 116(8):1538 – 1543, 2009.
- [93] J. Wang, K. Mitchell, G. W. Jewell and D. Howe. Multi-degree-of-freedom spherical permanent magnet motors. *IEEE International Conference on Robotics and Automation (ICRA)*, 2:1798 – 1805, 2001.
- [94] W. Wei, R. E. Goldman, H. F. Fine, S. Chang and N. Simaan. Performance evaluation for multi-arm manipulation of hollow suspended organs. *IEEE transactions on robotics*, 25(1):147 – 157, 2009.
- [95] W. Wei, R. E. Goldman, N. Simaan, H. F. Fine and S. Chang. Design and theoretical evaluation of micro-surgical manipulators for orbital manipulation and intraocular dexterity. *IEEE International Conference on Robotics and Automation (ICRA)*, pages 3389 – 3395, 2007.

- [96] C. Wheatstone. Contributions to the physiology of vision I - Part the first. On some remarkable, and hitherto unobserved, phenomena of binocular vision. *Philosophical Transactions of the Royal Society*, (128):371 – 394, 1838.
- [97] A. J. Woods and T. Rourke. Ghosting in anaglyphic stereoscopic images. *Stereoscopic Displays and Virtual Reality Systems XI, SPIE*, 5291(1):354 – 365, 2004.
- [98] L. Yan, I.-M. Chen, C. K. Lim, G. Yang, W. Lin and K.-M. Lee. Torque modeling of spherical actuators with double-layer poles. *IEEE/RSJ International Conference on Intelligent Robots and Systems (IROS)*, pages 5447 – 5452, 2006.

# Nomenclature

---

Symbol	Description	Unit
$A$	cross section	$m^2$
$B$	magnetic flux density	T
$c$	stiffness	N/m
$e$	error signal	m or rad
$E$	modulus of elasticity	$N/m^2$
$F$	force	N
$I$	current	A
$i$	transmission ratio	-
	input signal	V
$J$	inertia	$kgm^2$
$K$	actuator constant	N/A
$k$	torsional stiffness	Nm/rad
$l$	length	m
$m$	mass	kg
$p$	pitch	m
$P$	power	W
	controller gain	-
$R$	resistance	$\Omega$
$r$	radius	m
	reference signal	m or rad
$T$	torque	Nm
$u$	measurement signal	V
$U$	input torque	Nm
$V$	voltage	V
$v$	velocity	m/s
$x$	position	m
$y$	position	m
	output signal	m or rad
$z$	position	m

<b>Greek</b>	<b>Description</b>	<b>Unit</b>
$\alpha$	linear expansion coefficient	1/K
$\Delta x$	displacement in x	m
$\theta$	rotation around z axis	rad
$\mu$	friction coefficient	-
$\varphi$	rotation around x axis	rad
$\psi$	rotation around y axis	rad
$\sigma$	standard deviation	m
$\omega$	angular velocity	rad/s

<b>Subscript</b>	<b>Description</b>	<b>Subscript</b>	<b>Description</b>
<i>al</i>	aluminum	<i>max</i>	maximal
<i>b</i>	bending	<i>ms</i>	motor shaft
<i>cont</i>	continuous	<i>nom</i>	nominal
<i>dyn</i>	Dyneema <sup>®</sup>	<i>os</i>	outer segment part
<i>e</i>	encoder	<i>p</i>	preload
<i>ee</i>	end effector	<i>s</i>	stylus
<i>im</i>	inertia match	<i>seg</i>	segment
<i>is</i>	inner segment part	<i>tot</i>	total
<i>m</i>	motor	<i>ts</i>	torque sensor

<b>Abbreviation</b>	<b>Meaning</b>
2D	two dimensional
3D	three dimensional
AC	alternating current
AMC	academisch medisch centrum
AZM	academisch ziekenhuis Maastricht
C	controller
CAD	computer aided design
CCW	counterclockwise
CW	clockwise
CZE	Catharina ziekenhuis Eindhoven
da Vinci <sup>®</sup>	surgical system for robotically assisted MIS, registered trademark of Intuitive Surgical, Inc.
DC	direct current
DCT	dynamics and control technology group, TU/e
DoF	degree of freedom
DSP	digital signal processor
dSPACE <sup>®</sup>	data acquisition and control system, registered trademark of dSPACE GmbH
DVRT	differential variable reluctance transducer
Dyneema <sup>®</sup>	ultra-high molecular weight polyethylene (UHMwPE) fiber, registered trademark of DSM N.V.

<b>Abbreviation</b>	<b>Meaning</b>
EMF	electromotive force
EMI	electromagnetic interference
EyeRhas	eye robot for haptically assisted surgery
FAMM	fast and accurate manipulator modules
FEA	finite element analysis
FFC	flat flexible conductor
FFW	friction feedforward
FPC	flexible printed circuit
FRF	frequency response function
GND	ground (in electrical circuit)
IC	integrated circuit
ILM	internal limiting membrane
IM	instrument manipulator
JPL	Jet Propulsion Laboratory
KAIST	Korea Advanced Institute of Science and Technology
LCD	liquid crystal display
LIS	Leidse instrumentmakers school
LVDT	linear variable differential transformer
Matlab Simulink <sup>®</sup>	modeling and simulation software for dynamic systems, registered trademark of The MathWorks, Inc.
MIS	minimally invasive surgery
NX	computer aided design and manufacturing software, trademark of UGS Corp.
OR	operating room
P	plant
PC	personal computer
PCB	printed circuit board
PERR	position error
PLC	programmable logic controller
RTAI	realtime application interface
RAMS	robot assisted microsurgery
RMS	root mean square
RS232	serial communication standard
S	sensitivity
SISO	single input single output
T	complementary sensitivity
TTL	transistor-transistor logic
TU Delft	Technische Universiteit Delft
TU/e	Technische Universiteit Eindhoven
TUeDACS	TU/e data acquisition and control system
UvA	Universiteit van Amsterdam
ZNA	ziekenhuis netwerk Antwerpen



---

<b>Term</b>	<b>Meaning</b>
anterior	Front part of the eye.
ciliary body	Controls the accommodation of the eye and produces the aqueous humor that fills the space between the lens and the cornea
choroid	Layer of blood vessels between the retina and sclera. It supplies blood to the outer retina.
cornea	Transparent front part of the eye.
fovea	Center of the macula. It has the highest density of photoreceptor cells.
ILM	Internal limiting membrane, boundary between the retina and the vitreous body.
iris	Diaphragm that controls the amount of light that enters the eye.
lens	Focusses the image on the retina. The focal length is set via the ciliary muscle in the ciliary body.
limbus	Border of the cornea and the sclera.
macula	Responsible for central vision. The diameter is approximately 2.5 mm.
ora serrata	Serrated junction between the retina and the ciliary body.
posterior	Back part of the eye.
pupil	Hole in the center of the iris that light passes through.
retina	Light sensitive layer of photoreceptor cells as well as neuronal and support structures.
sclera	Opaque, white outer layer of the eye.
vitreous humor	Clear, gel like liquid that fills the space between the lens and the retina.

## Summary

---

Vitreoretinal surgery encompasses the surgical procedures performed on the vitreous humor and the retina. A procedure typically consists of the removal of the vitreous humor, the peeling of a membrane and/or the repair of a retinal detachment. Operations are performed with needle shaped instruments which enter the eye through surgeon made scleral openings. An instrument is moved by hand in four degrees of freedom (three rotations and one translation) through this opening. Two rotations ( $\varphi$  and  $\psi$ ) are for a lateral instrument tip movement. The other two DoFs ( $z$  and  $\theta$ ) are the translation and rotation along the instrument axis. Actuation of for example a forceps can be considered as a fifth DoF.

Characteristically, the manipulation of delicate, micrometer range thick intraocular tissue is required. Today, eye surgery is performed with a maximum of two instruments simultaneously. The surgeon relies on visual feedback only, since instrument forces are below the human detection limit. A microscope provides the visual feedback. It forces the surgeon to work in a static and non ergonomic body posture. Although the surgeon's proficiency improves throughout his career, hand tremor may become a problem around his mid-fifties.

Robotically assisted surgery with a master-slave system enhances dexterity. The slave with instrument manipulators is placed over the eye. The surgeon controls the instrument manipulators via haptic interfaces at the master. The master and slave are connected by electronic hardware and control software. Implementation of tremor filtering in the control software and downscaling of the hand motion allow prolongation of the surgeon's career. Furthermore, it becomes possible to do tasks like intraocular cannulation which can not be done by manually performed surgery. This thesis focusses on the master console.

Eye surgery procedures are observed in the operating room of different hospitals to gain insight in the requirements for the master. The master console as designed has an adjustable frame, a 3D display and two haptic interfaces with a coarse adjustment arm each. The console is mounted at the head of the operating table and is combined with

the slave. It is compact, easy to place and allows the surgeon to have a direct view on and a physical contact with the patient. Furthermore, it fits in today's manual surgery arrangement.

Each haptic interface has the same five degrees of freedom as the instrument inside the eye. Through these interfaces, the surgeon can feel the augmented instrument forces. Downscaling of the hand motion results in a more accurate instrument movement compared to manually performed surgery. Together with the visual feedback, it is like the surgeon grasps the instrument near the tip inside the eye. The similarity between hand motion and motion of the instrument tip as seen on the display results in an intuitive manipulation. Pre-adjustment of the interface is done via the coarse adjustment arm. Mode switching enables to control three or more instrument manipulators with only two interfaces.

Two one degree of freedom master-slave systems with force feedback are built to derive the requirements for the haptic interface. Hardware in the loop testing provides valuable insights and shows the possibility of force feedback without the use of force sensors.

Two five DoF haptic interfaces are realized for bimanual operation. Each DoF has a position encoder and a force feedback motor. A correct representation of the upscaled instrument forces is only possible if the disturbance forces are low. Actuators are therefore mounted to the fixed world or in the neighborhood of the pivoting point for a low contribution to the inertia. The use of direct drive for  $\varphi$  and  $\psi$  and low geared, backdriveable transmissions for the other three DoFs gives a minimum of friction. Disturbance forces are further minimized by a proper cable layout and actuator-amplifier combinations without torque ripple.

The similarity in DoFs between vitreo-retinal eye surgery and minimally invasive surgery (MIS) enables the system to be used for MIS as well. Experiments in combination with a slave robot for laparoscopic and thoracoscopic surgery show that an instrument can be manipulated in a comfortable and intuitive way.

User experience of surgeons and others is utilized to improve the haptic interface further. A parallel instead of a serial actuation concept for the  $\varphi$  and  $\psi$  DoFs reduces the inertia, eliminates the flexible cable connection between frame and  $\psi$  motor and allows that the heat of the  $\psi$  motor is transferred directly to the frame. A newly designed  $z$ - $\theta$  module combines the actuation and suspension of the hand held part of the interface and has a three times larger  $z$  range than in the first design of the haptic interface.

# Samenvatting

---

Vitreo-retinale oogchirurgie omvat de ingrepen op het glasachtig lichaam en het netvlies in het oog. Een operatie bestaat uit het verwijderen van het glasvocht, het verwijderen van een membraan en/of het herstellen van een netvliesloslating. Ingrepen worden uitgevoerd met naaldvormige instrumenten. De chirurg maakt hiertoe kleine incisies in de sclera. Een instrument wordt handmatig in vier vrijheidsgraden (drie rotaties en een translatie) rond dit toegangspunt gemanipuleerd. Twee rotaties ( $\varphi$  en  $\psi$ ) maken een zijdelingse beweging van de instrumenttip mogelijk. De overige twee vrijheidsgraden ( $z$  en  $\theta$ ) zijn de translatie en rotatie om de lengte as van het instrument. De bediening van bijvoorbeeld een pincet kan gezien worden als een vijfde vrijheidsgraad.

Oogoperaties worden gekenmerkt door de manipulatie van kwetsbaar weefsel van slechts enkele micrometers dik. Momenteel worden er maximaal twee instrumenten gelijktijdig gebruikt. De chirurg heeft alleen visuele terugkoppeling via een microscoop, aangezien de instrumentkrachten te klein zijn om ze te kunnen voelen. Het gebruik van de microscoop dwingt de chirurg om in een statische en niet-ergonomische houding te werken. Ondanks dat de vaardigheid door de jaren heen toeneemt, kunnen handtrillingen op een leeftijd van circa 55 jaar een probleem gaan vormen.

Robotische ondersteuning door middel van een master-slave systeem vergroot de mogelijkheden van de chirurg. De slave robot is boven het oog geplaatst en manipuleert de instrumenten. De chirurg bestuurt de instrumentmanipulators vanuit de master console door middel van haptische pennen. De master en slave zijn via electronica hardware en regelalgoritmen met elkaar verbonden. Het softwarematig filteren van handtrillingen en het schalen van de handbewegingen verlengt de loopbaan van de chirurg. Bovendien wordt het mogelijk om taken uit te voeren die niet handmatig gedaan kunnen worden, bijvoorbeeld het toedienen van een medicijn in een haarvat. Dit proefschrift richt zich op de master console.

Oogoperaties zijn bijgewoond in verschillende ziekenhuizen om inzicht te krijgen in de eisen voor de master console. De master console heeft een instelbaar frame, een 3D scherm en twee haptische pennen met ieder een arm voor de grofinstelling. De console

wordt aan de hoofddeun van de operatietafel bevestigd en is gecombineerd met de slave. Het systeem is compact, snel te plaatsen en biedt de chirurg de mogelijkheid om zichtcontact en fysiek contact met de patiënt te hebben. Verder past het geheel in de operatiekamer indeling, zoals die momenteel gebruikt wordt voor handmatig uitgevoerde operaties.

De haptische pen heeft dezelfde vijf vrijheidsgraden als het instrument in het oog. De chirurg kan via deze pennen de opgeschaalde instrumentkrachten voelen. Het verkleinen van de handbewegingen geeft preciezere instrumentbewegingen dan die welke met de hand mogelijk zijn. In combinatie met de weergegeven beelden is het alsof de chirurg het instrument direct in het oog in de buurt van de tip vasthoudt. De overeenkomst tussen hand- en instrumentbewegingen zorgt voor een intuïtieve aansturing. De grofinstelling wordt gebruikt om de pen van te voren in te stellen. Door om te schakelen kunnen drie of meer instrumentmanipulators aangestuurd worden met de twee pennen.

Twee één vrijheidsgraad master-slave systemen met krachtterugkoppeling zijn gebouwd om de eisen voor de haptische pen af te leiden. Experimenten geven waardevolle inzichten en laten zien dat krachtterugkoppeling zonder het gebruik van krachtsensoren gerealiseerd kan worden.

Twee haptische pennen zijn gerealiseerd om bimanuele chirurgie mogelijk te maken. Iedere vrijheidsgraad is voorzien van een encoder voor de positiemeting en een motor voor de krachtterugkoppeling. De opgeschaalde instrumentkrachten zijn alleen goed voelbaar als de stoorkrachten klein zijn. Actuators zijn zodoende direct aan het frame bevestigd of in de buurt van het draaipunt geplaatst om zo slechts een kleine bijdrage aan de totale traagheid te geven. Voor de  $\varphi$  en  $\psi$  vrijheidsgraad is een aandrijving zonder overbrenging gebruikt, de overige drie vrijheidsgraden zijn voorzien van een niet zelfremmende overbrenging met een lage overbrengverhouding om zo de wrijving te minimaliseren. Stoorkrachten zijn verder geminimaliseerd door een flexibele bekabeling en door het gebruik van motoren en versterkers die geen trillingen geven in het uitgangskoppel.

Vitreo-retinale oogchirurgie en minimaal invasieve chirurgie hebben overeenkomstige vrijheidsgraden, waardoor het systeem ook voor deze laatst genoemde operaties gebruikt kan worden. Experimenten met een slave robot voor buik en borstkaschirurgie laten zien dat een instrument in een gemakkelijke en intuïtieve manier gemanipuleerd kan worden.

Gebruikerservaringen van onder andere chirurgen zijn gebruikt om de haptische pen verder te verbeteren. Een parallelle  $\varphi$ - $\psi$  aandrijving geeft ten opzichte van een seriële aandrijving een lagere traagheid, maakt de flexibele kabel connectie tussen frame en  $\psi$  motor overbodig en zorgt ervoor dat de warmte van de  $\psi$  motor direct naar het frame afgevoerd kan worden. In de nieuw ontworpen  $z$ - $\theta$  module is de lagering van de pen gecombineerd met de aandrijving en heeft deze een drie maal grotere  $z$  slag dan in het eerste ontwerp van de haptische pen.

---

De verwachting is dat robotische ondersteuning door middel van een master-slave systeem voordelen biedt voor zowel chirurg als patiënt. Een ontwerp is gemaakt voor de master console en twee haptische penen zijn gerealiseerd om hiermee de bij de patiënt geplaatste slave robot aan te kunnen sturen. Een compacte layout maakt het systeem makkelijk integreerbaar in de huidige operatiekamer indeling.



# Dankwoord

---

Robotische ondersteuning bij het uitvoeren van oogoperaties door middel van een master-slave systeem. Een project waarbinnen niet alleen ik werkzaam ben geweest, maar ook tal van andere mensen meegeholpen hebben aan de ontwikkeling van de master console. Zodoende wil ik dan ook de volgende personen bedanken:

Nick Rosielle. Bedankt voor de directe begeleiding tijdens de afgelopen jaren. Het was een erg leerzame tijd. Vol verwondering heb ik me altijd afgevraagd hoe je het toch klaarspeelt om met ogenschijnlijk gemak nieuwe oplossingen en ideeën aan te dragen.

Henk Nijmeijer. Ook jou wil ik graag bedanken voor de begeleiding en uiteraard het vertrouwen en de geboden kans om met dit project aan de slag te kunnen gaan. Ik waardeer de geboden vrijheid in combinatie met de kritische blik en waar nodig het commentaar om het geheel in goede banen te leiden.

Maarten Steinbuch. Ik heb het altijd bewonderenswaardig gevonden hoe snel je tot de kern van de zaak wist door te dringen en de benodigde hulp kon aanbieden in de soms toch wel korte besprekingen. Bedankt voor de betrokkenheid en enthousiasme bij dit gedeelte van het EyeRhas project.

Marc de Smet, Eric van Oosterhout en Igor Lundqvist wil ik bedanken voor het kunnen bijwonen van de oogoperaties, voor jullie advies en voor de tijd die jullie wisten vrij te maken voor de verschillende besprekingen.

Lucas van Leeuwen, Jurgen Bulsink, René Henselmans, Fabian Manders en de andere mensen van de GTD instrumentmakerij die hebben geholpen met de realisatie van de 1 DoF opstellingen en de haptische pennen. Zonder jullie had de hardware er niet gestaan. Het was erg leerzaam en leuk om jullie aan het werk te zien. Hetzelfde geldt voor Jovita Moerel, Paul Aendenrooier, Paul Beijer, Jos van Kruijsdijk en Rinus Janssen voor de realisatie van de electronica.

Jasper Grasman en Pieter Poels wil ik bedanken voor hun afstudeer- en stagebijdragen aan het ontwerp van de master console. Betreffende de control van de 1 DoF opstellingen geldt hetzelfde voor Jesse Scholtes. Het was erg plezierig en leerzaam om met jullie



samen te werken.

Voor de ondersteuning bij de electronica en regeltechniek wil ik een woord van dank uiten aan: Harrie van de Loo, Peter Hamels, Dennis van Raaij, Ramon Solberg, Ruud van den Bogaert, George Leenknecht, Kees-Jan Zandsteeg en Ruud van der Aalst.

Dit project zou zonder financiering niet mogelijk zijn geweest. Zodoende wil ik dan ook Lou Hulst, Casper Langerak, Eddy Schipper en Annette Steggerda van SenterNovem/ Agentschap NL bedanken. Ook de nog niet genoemde leden van de begeleidingscommissie wil ik via deze weg bedanken voor hun input tijdens de halfjaarlijkse besprekingen.

Ook TNO heeft een belangrijke rol gespeeld. Een woord van dank gaat dan ook uit aan Pieter Kappelhof, Ian Saunders, Jeroen Heijmans, Michiel Oderwald, Bart Dirx en Bas de Kruif voor het opzetten en het leiden van dit project. Zonder de themamiddag over medische technologie was dit project waarschijnlijk niet tot stand gekomen.

Prof. Frans van der Helm (TU Delft) en Prof. Elena Lomonova (TU/e) wil ik bedanken voor het lezen van de conceptversie van dit proefschrift.

Directe (oud)collega's uit het Constructies en Mechanismen lab en natuurlijk ook uit de DCT groep, voor zover nog niet genoemd. In het bijzonder wil ik Chris Werner bedanken voor de vakinhoudelijke discussies, Thijs Meenink voor de prettige samenwerking binnen het EyeRhas project en Lia Neervoort samen met Petra Aspers voor hun ondersteuning tijdens de afgelopen jaren.

Buiten het werk verdienen ook de leden en de trainers van de Eindhovense Studenten Schaats Vereniging Isis een woord van dank. Dankzij jullie heb ik tal van mooie momenten op en naast het ijs mogen beleven. Al met al heeft dit een belangrijke bijdrage gevormd aan de nodige ontspanning.

Tenslotte mogen natuurlijk ook mam, Yvonne en Walter niet vergeten worden. Dank jullie wel voor de steun tijdens de afgelopen jaren. Zonder deze steun was dit alles niet gelukt. Pap, helaas mocht je de afsluiting van dit alles niet meer meemaken.

Ron Hendrix,  
Februari 2011

# Curriculum Vitae

---

Ron Hendrix was born on December 19, 1980 in Arcen en Velden, the Netherlands.

- 1993-1999 Secondary school, Scholengemeenschap Venlo & Omstreken, Venlo.
- 1999-2005 Mechanical Engineering at Technische Universiteit Eindhoven. Graduated (cum laude) within the Constructions & Mechanisms group.
- 2004-2005 Master thesis project at TNO TPD, Delft and ASML SA, Veldhoven.
- 2005-2006 Visiting scientist in the Dynamics and Control group within the Department of Mechanical Engineering at Technische Universiteit Eindhoven.
- 2006-2011 Ph.D. candidate at Technische Universiteit Eindhoven, Department of Mechanical Engineering, Dynamics and Control group.

